University of Trento
Department of Physics
Doctoral thesis

~ · ~

Academic Year 2023–2024

Enhancing the detection and the reconstruction of gravitational-wave transients in the LIGO-Virgo-KAGRA data using weak assumptions on the astrophysical sources

Supervisor
Prof. Giovanni Andrea Prodi

Author
Sophie Bini

Final examination date: 3 July 2024

Acknowledgments

I would like to thank my supervisor Giovanni Prodi for his guidance and support during the course of my PhD. Thank you for teaching me gravitational-wave physics, and for giving me the freedom to explore different topics. It is always a pleasure to discuss with you about physics, and our university.

This thesis would not be possible without all the discussions, advices and support of the research group I had the chance to work with. I would like to thank Francesco Salemi and Gabriele Vedovato for introducing me to CoherentWaveBurst and patiently help me whenever I needed, Marco Drago and Claudia Lazzaro for sharing their knowledge and expertise. I would like to acknowledge our colleagues in Trieste, especially Edoardo Milotti, Agata Trovato, Andrea Virtuoso and Giacomo Principe: it's always a pleasure to work with you. I would like also to thank my colleagues Andrea Miani, Alessandro Martini for making the office such a friendly environment.

A special thanks to Shubhanshu Tiwari, for inviting me to the amazing city of Zurich, and to Yumeng Xu, Dixeena Lopez, Eleanor Hamilton for warmly welcoming me. It has been a wonderful experience.

Vorrei ringraziare i miei genitori, che sono sempre contenti quando arrivano delle onde gravitazionali, mia sorella, grazie alla quale posso continuare a fare questo lavoro comodamente, e tutta la mia famiglia che appoggia sempre le mie scelte, anche quando queste ci allontanano per un pò. Grazie a tuttə lə dottorandə di Trento per aver creato una piccola comunità in cui mi sento sempre a casa, ai miei coinquilini circensi, a Gabriella e Marta per aver affrontato con me draghi e zanzare e a Martina per essermi sempre vicina, nonostante il fuso orario!

Infine, vorrei ringraziare Alberto: in tutti questi anni hai sempre saputo ascoltarmi e trovare le parole giuste per incoraggiarmi. Ci sono poche cose certe nella vita di una ricercatrice, ma sapere di averti accanto mi basta per essere felice.

This material is based upon work supported by NSF's LIGO Laboratory which is a major facility fully funded by the National Science Foundation. I also gratefully acknowledge the support of the Science and Technology Facilities Council (STFC) of the United Kingdom, the Max Planck Society (MPS), and the State of Niedersachsen/Germany for support of the construction of Advanced LIGO and the construction and operation of the GEO600 detector. Additional support for Advanced LIGO was provided by the Australian Research Council. I gratefully acknowledge the Italian Istituto Nazionale di Fisica Nucleare (INFN), the French Centre National de la Recherche Scientifique (CNRS) and the Netherlands Organization for Scientific Research (NWO), for the construction and operation of the Virgo detector and the creation and support of the EGO consortium Moreover, I also acknowledge the support of the NSF, STFC, INFN, and CNRS for the provision of computational resources. This research was also partially supported by the PRIN project 202275HT58.

Abstract

Since the first observation of a gravitational-wave (GW) in 2015, the LIGO and Virgo detectors reported tens of astrophysical signals interpreted as mergers of compact objects. These observations provide invaluable tests of the General Relativity and open a new era of astronomy, unveiling compact objects' nature. The first chapter of the thesis recalls briefly the theoretical fundaments of GWs and summarizes the path to their discovery.

GWs are observed with ground-based large scale interferometers. The second chapter describes these facilities, and overviews the main data analysis techniques that lead from the interferometers outputs to the detection and the interpretation of GW events.

The focus of the thesis is the detection and the characterization of GW transients with minimal assumptions on the GW sources. To identify astrophysical signals embedded in detector noise, there are two main approaches: template-based and unmodelled searches. The firsts look for GW signals with a time-frequency evolution consistent to the waveform models contained in extensive template banks. Instead, unmodelled or burst searches do not assume a waveform model, but look for excess of power that is coherent on multiple GW detectors.

Burst searches are fundamental to observe GWs from various astrophysical sources, outlined in the third chapter. Unmodelled searches observe GWs originated from the coalescence of compact binaries, and might observe GWs that are expected by other sources such as supernovae, isolated neutron stars, and cosmic strings. Burst searches also provide the reconstruction of the GW waveform with minimal assumptions, and are able to identify discrepancies between theoretical models and measured data, which may reveal new physics.

A well-known software for burst searches is Coherent WaveBurst (cWB), presented in the fourth chapter. cWB identifies excess of power with respect to the detector noise that are coherent in the GW detectors network. The data stream from each detector is transformed into the time-frequency domain using wavelets, and the most energetic time-frequency regions are selected. Then, a likelihood ratio statistic is maximized over all sky directions. cWB associates to each candidate event a false alarm probability to distinguish between significant outliers and detector noise. The significance is estimated using a background distribution build from time-shifted data: the data of one detector are time-shifted with respect to the other detector(s), so that the signals that are coherent cannot have an astrophysical origin by construction, but they are due only to transient noise. A further step to increase the cWB search sensitivity is implemented using a decision-tree learning classification algorithm.

Within this framework, the fifth, sixth and seventh chapters summarize the author's original contributions to this field:

- **Search sensitivity of three-detectors network in burst searches**
  Having more detectors participating in the GW observations generally improves the source localization and the characterization of the GW signals. The capability of burst searches to distinguish between potential signals and transient noise depends on the orientation of the detectors and on their relative sensitivities. In literature, the cWB search sensitivity of the three-detectors network composed of the LIGO and Virgo detectors (HLV) is lower than the one achieved using only LIGO detectors (HL). cWB uses likelihood regulators to force the reconstruction of the GW component observed by the LIGO aligned detectors. These regulators successfully reduce the false alarm rate of the HL coherent analysis, but to make full use of a third, not-aligned detector, they should be relaxed.

  The fifth chapter investigates the impact of the likelihood regulators in cWB for HLV network, first in a simplified case assuming Gaussian noise only, and then in the data from the third LIGO-Virgo-KAGRA observing run. Thanks to latest cWB enhancements and relaxed likelihood regulators, we show that the HLV network reduces significantly the gap w.r.t. HL, having a higher sensitivity for several waveforms tested on average over the sky directions. Moreover, we investigate the use of the HLV network to test the consistency between cWB unmodelled signal reconstruction and the GW waveform models.

- **An autoencoder neural network integrated into GW burst searches to improve the rejection of noise transients**
  GW data contains short-duration disturbances, called glitches, which can mimic astrophysical signals. Mitigation of glitches is particularly difficult for unmodelled algorithm, such as cWB, that do not use GW waveform models to filter the data, but are sensitive to the widest possible range of morphologies.

  Noise mitigation is a long-term effort in cWB, which led to the introduction of specific estimators and a machine-learning based signal-noise classification algorithm. The sixth chapter presents an autoencoder neural network, integrated into cWB, that learns transient noise morphologies from GW time-series and it improves their rejection. An autoencoder is an unsupervised learning neural network that compresses the input data into a lower dimensional space, called *latent* space, and then re-constructs an output with the original dimensions. Here, the autoencoder is trained on time-series belonging to a single glitch family, known as blip, and the network learns that specific morphology.

  The autoencoder improves cWB discrimination between blip-like glitches and potential GW signals, reducing the background trigger at low frequencies. We inject in the LIGO detectors' data from the third Advanced LIGO-Virgo observing run a wide range of simulated signals, and we evaluate the cWB search sensitivity including the autoencoder output in the cWB ranking statistics. At a false alarm rate of one event per 50 years, the sensitivity volume increases up to 30% for signal morphologies similar to blip glitches.

- **Search for hyperbolic encounters between compact objects in the data from the third LIGO-Virgo-KAGRA observing run**
  As GW detectors sensitivity increases, new astrophysical sources could emerge. Close hyperbolic encounters (HE) are one such source class: scattering of stellar mass compact objects is expected to manifest as GW burst signals in the frequency band of current detectors. The seventh chapter presents the search for GWs from HE in the data from the second-half of the third observing run using cWB. No significant event has been identified in addition to known detections of GW events.

We inject third Post-Newtonian order accurate HE waveforms with component masses between [2,100]$M_{\odot}$. For the first time, we report the sensitivity volume achieved for such sources, i.e. the portion of the Universe in which the proposed analysis would have detected a HE signal with a certain significance, if any. The sensitivity volume peaks at $3.9\pm1.4\times10^{5}$ $\mathrm{Mpc}^{3}\mathrm{year}$ for compact objects with masses between [20, 40] $M_{\odot}$, corresponding to a rate density upper limit of 0.589 ± 0.094 $\times10^{-5}\mathrm{Mpc}^{-3}\mathrm{year}^{-1}$. Moreover, the sensitive volume prospects for the next observing runs of current detectors are discussed.

All the result shown are based on the latest publicly available data from the third observing run of the LIGO-Virgo-KAGRA collaboration.

Contents

Acronyms

ASD amplitude spectral density.

BBH binary black hole.

BH black hole.

BNS binary neutron star.

CBC compact binary coalescence.

CCSNe core collapse supernovae.

cWB Coherent WaveBurst.

DPF Dominant Polarization Frame.

FAR false alarm rate.

GA Gaussian pulse (signal).

GR general relativity.

GW gravitational waves.

HE hyperbolic encounter.

HL LIGO Hanford and LIGO Livingston detectors network.

HLV LIGO Hanford, LIGO Livingston,and Virgo detectors network.

HLVK LIGO Hanford, LIGO Livingston, Virgo, KAGRA detectors network.

IFAR inverse false alarm rate.

LVK LIGO-Virgo-KAGRA (collaboration).

ML machine learning.

MSE mean square error.

NS neutron star.

NSBH neutron star-black hole.

PE parameter estimation.

PN post Newtonian (approximation).

PSD power spectral density.

SG sine-Gaussian (signal).

SNR signal to noise ratio.

TF time-frequency.

TT traverse-traceless (gauge).

WNB white noise burst.

Chapter 1

Brief introduction to gravitational-waves theory

Gravitational-waves (GW) are ripples of the gravitational field that can be generated by various astrophysical sources. GWs propagates at the speed of light outward from their source. Their existence was derived from Einstein's General Relativity theory in the first decades of 1900. In the 50s, experiments to observe GW emission began to be designed, and in 2015 the first observation of GWs from the merger of two black holes was announced by the LIGO-Virgo collaboration. Section 1.1 recalls the main historical events that have marked this field of research.

The groundbreaking discovery opened the era of GW astronomy. To date, 90 GW events have been published by the LIGO-Virgo-KAGRA (LVK) collaboration in GW catalog [1], and ten of GW candidate events from the ongoing observing run have been publicly reported [2]. GW observations provide an extraordinary amount of information on the compact objects' nature, on the formation of the early Universe, and enable to test General Relativity in strong regimes.

This chapter introduces GW theory. It aims to provide the basic notation of GW science to a reader with knowledge in physics, but not in this specific field. Section 1.2 derives the wave equations from the linearization of Einstein's equations, and Section 1.3 outlines the main astrophysical source of GWs, and shows examples of GW waveforms in simple cases.

1.1 The road to the discovery

This section presents the main historical events that lead to the groundbreaking discovery of GWs, following mostly Ref. [3]. The history of gravitational-waves started with the formulation of Einstein's General Theory of Relativity (GR), published in 1915. GR unravels gravitation, establishing a relationship between the geometry of the spacetime with the mass and the energy within that spacetime. The core of the theory is expressed by Einstein's equations (Eq. 1.1 in the next section). These equations cannot be solved in full generality, and only specific solutions assuming particular simplistic conditions are known. In the years following the publication of GR, the idea to derive wave equations for the gravitational case similar to the electromagnetic waves started to emerge. In 1922, Eddington published an article on the propagation of GWs, deriving the existence of a type of wave travelling at the speed of light from Einstein's equations. For several years, Einstein itself was not convinced of the existence of GWs, suspecting that the wave equations were only a mathematical artifact produced by a peculiar coordinate system. With the help of Infeld, his student, and Robertson, who was asked to review an Einstein's

article, Einstein admitted an error in the calculations and became convinced of the existence of GWs.

Next, the debate focused on whether GWs carry energy or not. It is not obvious to study energy conservation in GR: the conservation of the energy means that the energy of a system is a constant over time. In GR time is part of the coordinate system, and it depends on the position. Locally the spacetime can always be considered flat, and there the energy is conserved. Globally, the question is more complex. Within this debate, the work of Pirani was particularly innovative: instead of investigating the source of GWs, he tackled the practical question of which would be the effect of GWs on the medium. Pirani showed that a GW would move particles back and forth as it passes though the matter. Pirani's work was published in 1956 on a polish journal [4], and unfortunately remained unknown for a long time.

The debate on GWs energy continued up to the Chapel Hill conference, in 1957, a turning point event in the history of GWs. There, Feynman convinced most of the community that GWs carry energy using the 'sticky bead' thought experiment: a GW would shake back and forth a bead on a stick, oriented transversely w.r.t. the direction of propagation of the wave, heating both the bead and the stick. Among the audience, there was also Weber, who committed to design an experiment to observe GWs on Earth.

Weber considered different experimental set-ups. In the 60s, he started the design and construction of cylindrical bars that would act as antenna of GWs [5]. The bars had dimensions of about 70cm in diameter and 150cm in length, were made in aluminium, and suspended to mitigate terrestrial vibrations. The passage of a GW would stimulate the resonant modes of the bars. Several piezoelectric sensors were placed on the surface of the bar to measure its vibrations: these sensors would enable to detect a GW as an electrical signal. Weber built two bars and placed them 950km away. An astrophysical event would produce signals with similar characteristics in both bars, while signals observed only in a single antenna would suggest a local terrestrial origin. The idea of using the coherence among multiple detectors to distinguish astrophysical signals from instrumental and environmental noise is adopted still nowadays.

In 1969, Weber announced the discovery of GWs [6]: he claimed the detection of several signals originated from the centre of our galaxy. The results were not convincing from a theoretical perspective: the amount of energy released in form of GWs, according to Weber's findings, implied that a huge amount of stellar mass was converted in GWs. Such a rapid decrease of the mass of the galaxy would have dispersed the galaxy long ago. Moreover, in the following years several groups realized independently resonant bars, similar to Weber's one, to validate its results and no groups observed GWs. A certain pessimism around the field started growing.

The scepticism blow away in 1974 thanks to the discovery of the Hulse - Taylor binary pulsar [7]. A pulsar is a rapidly rotating neutron star emitting periodic electromagnetic flashes. Hulse and Taylor recorded the radio emissions from a pulsar, and realized that there was a systematic variation in its pulses: the pulsar's period was about 60 milliseconds, but sometimes it occurred before than expected and sometimes after, with a period of variations of about 7.7 hours. This behaviour is explained if the pulsar is part of a binary system with another astrophysical object. The binary system observed by Hulse and Taylor is composed of a neutron star and a pulsar, orbiting around their center of mass. The timescale of the variability of the pulses indicates the period of the binary. Most importantly, Hulse and Taylor realized that the orbital period was decreasing over the years, and the decaying rate was consistent with the emission of GWs according to GR. This observation constituted the first indirect observation of GWs, and was awarded with the Nobel Prize in 1993.

The discovery of the binary pulsar confirmed the correctness of GR, and boosted the search for a direct observation. A different experiment to observe GWs emerged: large-scale Michelson interferometers. Such systems enable high precision measurements of variations of the optical

path of a laser. As shown in Section 2.1, the effect of a GW is to shake the interferometer's suspended optics, modifying the optical path between them. The idea of using interferometry to detect GWs had several precursors. In the 70s, several scientists among which Forward, Weiss, and Drever started the construction of the first prototypes. These instruments were of the order of meters long. In particular, the German group at Garching, together with the Glasgow group, realized a 30m long prototype and asked funding for building a 3km facility. As explained in the Section 2.1, the longer the interferometer's, the more sensitive to GWs. Unfortunately, the proposal was not funded completely, and they decided to build a shorter detector 600m long, known today as GEO 600 [8]. Its construction begun in 1995, and it was operational in 2001. Over the years, GEO 600 has allowed to acquire experience with the operations of such instruments, and has tested several technologies.

GW interferometers are complex instruments, and the size and the accuracy needed to observe GWs, required the building up of large collaborations. In 1975 Weiss, who was building an interferometer prototype at MIT, met the theoretical physics Thorne which envisioned to build a GW interferometer at Caltech. After some years, the two institutions joined the efforts, and proposed the 'Laser Interferometer Gravitational-wave Observatory', known as LIGO [9]. The project consisted of two 4km long interferometers located in Hanford (Washington) and in Livingston (Louisiana), it was funded in 1988, and the construction was completed in 1997. In 2002 LIGO started taking data.

In the 80s, also the Italian and French GW communities started the design of a 3km interferometer, Virgo [10], named from the stellar cluster that would have been observable with the detector. Virgo is located in the countryside near Pisa, in Italy. The construction started in 1996, and in 2007 Virgo joined LIGO in a collaboration to search for GWs. The frequency bandwidth of ground-based detectors $\sim$km long is between 20Hz to 4000Hz.

In the following years, the expectations and the pressure for the discovery of GWs were growing. In 2010 the LIGO and the Virgo collaboration did a stress-test to verify their detection capabilities: a strong signal was injected in the data of both LIGO detectors. The signal was found consistent with a GW originated from the coalescence of a black hole and a neutron star. The signal seems to come from the constellation Canis Major, so that in the community it is referred to as the 'Big Dog' event. Few people knew that the signal had not an astrophysical origin, but was just a test: the collaboration proceeded as if it was real and prepared a scientific publication to report the discovery. At the end, it was revealed that the signal was just an injection. For sure, it was disappointing for several scientists, but the collaboration proven to be ready to detect GWs!

The long sought discovery occurred in 2015: on September 14, a signal was recorded in the LIGO detectors [11]. The signal, referred to as GW150914, was consistent with the emission of a GW from the coalescence of two black holes of masses $36^{+5}_{-4}M_{\odot}$ and $29^{+4}_{-4}M_{\odot}$ at a luminosity distance of 410^{+160}_{-180} Mpc. About an energy of $3^{+0.5}_{-0.5}M_{\odot}c^2$ were released in form of GWs. Fig. 1.1 shows the signals observed in the two LIGO sites and the comparison with the GW waveforms model. The first algorithm that detected the signal embedded in the detector noise was Coherent WaveBurst [12], discussed in great detail in Chapter 4 and used to produce most of the results presented in this thesis. The discovery of GWs was announced on 11 February 2016, and it was awarded with the Nobel Prize to Barish, Weiss and Thorne in 2017.

Since 2015, there have been three periods of data taking, called observing runs, spaced out with periods in which the detectors' sensitivities are improved. The fourth observing run is ongoing at the time of writing this thesis. In addition, a new detector, KAGRA [13], has joined the network of detectors. KAGRA is located in Toyama, Japan, in a cave under a mountain. It is the first GW interferometer working at cryogenic temperatures to reduce the noise due to thermal fluctuations.

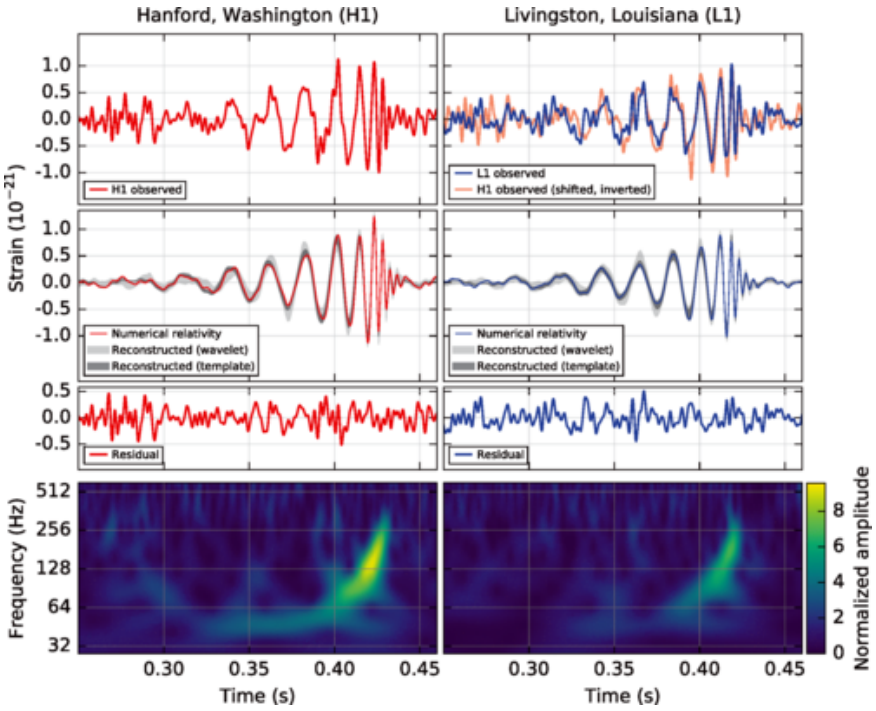

Figure 1.1: The first GW event observed by LIGO Hanford (left column) and LIGO Livingston (right column) detectors. The first row shows the measured data, the central row compares the signals reconstructed with the GW waveforms computed modelling the coalescence of two black holes with a numerical relativity method (red). The residual after subtracting the numerical relativity method from the measured data are presented. The last row shows the measured data in the time-frequency domain: in this representation, it is evident the 'chirp' structure expected by the coalescence of compact binaries [11].

To date, tens of GW events have been reported by the LVK collaboration [1]. The observed events are consistent with the emission of GWs from the coalescence of binary systems composed of two black holes (BBH), two neutron stars (BNS), or a black hole and a neutron star (NSBH). A GW event that is worth mentioning in this introduction is GW170817 [14]: it is consistent with the coalescence of two neutron stars, and an electromagnetic counterpart was observed in several bands, from gamma-ray to radio, opening the era of multi-messenger astronomy with GWs. GW observations provide an important amount of information on compact objects' nature and allow testing GR in strong regime with unrivalled accuracy [15]. In addition, the increasing number of detections is opening the road to the investigation of the population of compact objects, and to the identification of the astrophysical formation channels of such systems [16].

GW astronomy has just begun: in the next decades, new generation of detectors will lead to many more observations and would allow the exploration of bigger portion of the Universe. The interferometer LIGO India [17] will join the detector network. The design of third-generation ground-based interferometers is planned in Europe, Einstein Telescope [18], and in the US, Cosmic Explorer [19], which should start to take data around 2035. In addition, the LISA mission [20], made of a constellation of three satellites millions of kilometres away from each other, will allow the detection of low frequency GWs from space.

1.2 Linearization of the Einstein's equations

The Einstein's equations are the fundamentals of GR, describing the relationship between the geometry of the spacetime, represented by the generic metric $g_{\mu\nu}$, and the mass and the energy of the system, contained in the stress-energy tensor $T_{\mu\nu}$. The Einstein's equations are ten non-linear partial differential equations:

$$R_{\mu\nu} - \frac{1}{2}\, g_{\mu\nu} R = \frac{8\pi G}{c^4} T_{\mu\nu} \tag{1.1}$$

where $R_{\mu\nu}$ and R are the Ricci tensor and the scalar curvature, that depends on the first and the second derivative of the metric $g_{\mu\nu}$. For weak gravitational fields, the metric can be expanded around the flat-space metric $\eta_{\mu\nu}$ and small fluctuations $h_{\mu\nu}$ as:

$$g_{\mu\nu} = \eta_{\mu\nu} + h_{\mu\nu}, \qquad \text{where} \quad |h_{\mu\nu}| \ll 1 \tag{1.2}$$

The presence of GWs emerges linearizing the Einstein's equations to the first order w.r.t. $h_{\mu\nu}$. When substituting Eq. 1.2 in the Einstein's's equations, it is useful to define $\bar{h}_{\mu\nu} = h_{\mu\nu} - 1/2 \eta_{\mu\nu} h$, where $h = \eta^{\mu\nu} h_{\mu\nu}$. In addition, similarly to the electromagnetic case, the gauge invariance can be used to set $\partial^\mu \bar{h}_{\mu\nu} = 0$. From the linearization, the wave equation is obtained as:

$$\boxed{\Box \bar{h}_{\mu\nu} = -\frac{16\pi G}{c^4} T_{\mu\nu}} \tag{1.3}$$

where $\Box = -(1/c^2)\partial_0^2 + \nabla^2$. A complete explanation can be found in the first chapter of Ref. [21]. The tensor $T_{\mu\nu}$ generates the waves in $h_{\mu\nu}$, i.e. the GWs. The matrix $h_{\mu\nu}$ is symmetric, so it has 10 independent components. The gauge invariance $\partial^\mu \bar{h}_{\mu\nu} = 0$ reduces the number of independent components to 6.

Eq. 1.3 is the starting point to compute the generation of GWs in the linearized approximation. Outside the source of GWs, $T_{\mu\nu} = 0$. There, the residual gauge freedom reduces further the independent components of $h_{\mu\nu}$ to 2. This is known as the traverse-traceless (TT) gauge for which:

$$h^{00} = 0\,, \qquad h^{0i} = 0\,, \qquad \partial_i h^{ij} = 0\,, \qquad h^i_i = 0 \tag{1.4}$$

From the equations above, the only non-zero components of h^{TT}_{ij} are in the plane transverse to the direction of the propagation $\hat{\mathbf{n}}$. Choosing $\hat{\mathbf{n}}$ along the z axis for simplicity, a solution of Eq. 1.3 outside the source in the TT gauge is:

$$h^{TT}_{ij}(t,z) = \begin{pmatrix} h_+ & h_\times & 0 \\ h_\times & -h_+ & 0 \\ 0 & 0 & 0 \end{pmatrix}_{ij} \cos(w(t - z/c)) \tag{1.5}$$

where h_+ and $h_\times$ are the 'plus' and 'cross' polarizations of the wave: a rotation of $\pi/4$ around the propagation axis transforms one polarization into the other. The TT gauge is particularly useful because GWs have a simple form, as in Eq. 1.5. Physically, in the TT gauge an object at rest before the passage of a GW, remains at rest, while its coordinates stretch. Hence, an object at rest does not change coordinates (see Section 1.3.3 in Ref. [21] for a complete proof).

Given a plane wave h_{kl} propagating outside the source in a generic direction $\hat{\mathbf{n}}$, the solution is transformed into the TT gauge as:

$$h^{TT}_{ij} = \Lambda_{ij,kl} h_{kl} \tag{1.6}$$

where $\Lambda_{ij,kl}$ is a projector defined as:

$$\Lambda_{ij,kl} = P_{ik} P_{jl} - \frac{1}{2} P_{ij} P_{kl}, \qquad \text{where} \quad P_{ij}(\hat{\mathbf{n}}) = \delta_{ij} - n_i n_j \tag{1.7}$$

It is useful to show an example of a GW generated by a generic source in a simple case, including the tensor $T_{\mu\nu}$ (from Section 3.3 in Ref. [21]). The solution of Eq. 1.3, using Green's function, is

$$\bar{h}_{\mu\nu}(t, \mathbf{x}) = -\frac{4G}{rc^4} \int d^3x' T_{\mu\nu}(t - \frac{r}{c} + \frac{\mathbf{x}' \cdot \hat{\mathbf{n}}}{c}, \mathbf{x}') \tag{1.8}$$

where the energy-momentum tensor is evaluated at the retarded time $t - r/c$. In the TT gauge, using the transformation in Eq. 1.7, the equation above becomes:

$$\bar{h}^{TT}_{ij}(t, \mathbf{x}) = -\frac{1}{r}\frac{4G}{c^4}\Lambda_{ij,kl}(\hat{\mathbf{n}}) \int d^3x' T_{kl}(t - \frac{r}{c} + \frac{\mathbf{x}' \cdot \hat{\mathbf{n}}}{c}, \mathbf{x}') \tag{1.9}$$

The wave amplitude decrease linearly with the distance from the source r. For a non-relativistic source, the solution of the wave equation (Eq. 1.9) can be expanded in series of v/c. The leading term of the expansion is:

$$h^{TT}_{ij}(t, \mathbf{x}) = \frac{1}{r}\frac{2G}{c^4}\Lambda_{ij,kl}(\hat{\mathbf{n}})\frac{d^2}{dt^2}Q_{kl}(t - r/c), \tag{1.10}$$

where Q_{kl} is the quadrupole moment:

$$Q_{kl} = \int d^3x (x_k x_l - 1/3 r^2 \delta_{kl}) \frac{T^{00}}{c^2} \tag{1.11}$$

at lowest order in v/c, T^{00}/c^2 corresponds to the source mass density. Eq. 1.10 is referred to as the quadrupole radiation, and shows that GWs are primarily originated by the variations in time of the quadrupole moment.

To conclude this section, the energy carried by GW is briefly mentioned. Within the linear approximation, the energy carried by a GW is null because the TT gauge fixes $\partial^\mu \bar{h}_{\mu\nu} = 0$, so from Eq. 1.3 $\partial^\mu T_{\mu\nu} = 0$. To study the energy carried out by GWs, it is necessary to go beyond the first linear approximation, considering the quadratic order of the metric fluctuations $h_{\mu\nu}$. The energy flux carried by a GW through a surface element dA is (see Section 1.4 in Ref. [21]) is:

$$\frac{dE}{dAdt} = \frac{c^3}{32\pi G}\langle \dot{h}^{TT}_{ij}\dot{h}^{TT}_{ij}\rangle = \frac{c^3}{16\pi G}\langle \dot{h}^2_+ + \dot{h}^2_\times\rangle \tag{1.12}$$

The GW luminosity is computed substituting the waveform expression (as Eq. 1.9) in the above equation.

1.3 Overview of gravitational-waves sources

This section overviews the main astrophysical sources that emit, or are expected to emit, GWs. The GW emissions can be divided in three main categories: transients GWs, continuous GWs, and the stochastic background of GWs.

1.3.1 Transient gravitational-waves

Transient GWs refer to signals with a typical duration of the order of seconds or less, extending up to the order of hours in certain cases, in which a large amount of GW energy is released. Short-duration GWs are produced from the coalescence of compact binaries (CBC), as in the case of the first GW observation showed in Fig. 1.1, and the other GW events reported by the LVK collaboration. Transient GWs are also expected from supernovae, isolated neutron stars undergoing a rearrangement of their structure, and cosmic strings.

Next, the GW emission from CBC is introduced briefly, while the other sources of GW transients will be discussed in more detail in Chapter 3.

Compact binary systems involve two compact objects, black holes (BH) and/or neutron stars (NS), that orbit around each other. During the inspiral phase, the orbital period decreases due to emission of GWs (as observed by Hulse and Taylor). To compensate the loss of energy caused by GW emission, the radius r of the orbit decreases. According to Kepler's law, the frequency of the orbit is proportional to M/r, where M is the mass of the system. The frequency of the GWs is twice the frequency of the orbit, and it increases as r decreases. The radiated power in form of GWs is correlated with the frequency of the signal, and it increases over time as well. This runaway process proceeds until the objects are too close and merge, releasing a huge amount of energy in the form of GWs with a characteristic chirp signature in the time-frequency domain, as shown in Fig. 1.1. In the case of the first direct GW observation, GW150914 [11], the total amount of energy released in form of GWs is $3 \pm 0.05 M_{\odot} c^2$, and considering the inferred distance ($\sim$ 400Mpc) the estimated peak luminosity is of the order of $\sim 10^{56}$erg s^{-1}. For comparison, the ultra luminous GRB110918A reached a peak isotropic-equivalent luminosity of 10^{54} erg s^{-1} [22]. The remnant of the coalescence is a compact object.

The totality of the GW events observed so far originated from such systems [1, 23, 24]. GWs are released during the whole inspiral phase, but at large orbit the GW amplitude is low and the GW frequency is below the frequency band of current ground-based detectors. LIGO and Virgo, which operate in the frequency range between $\sim$20Hz up to $\sim$4000 Hz, catch only the latest cycles of the inspiral of BBH with component masses of about $\sim 50 M_{\odot}$. The coalescence of BNS, instead, occurs at higher frequencies and several cycles of the inspiral can be observed [14].

In a simple case, the two compact objects with masses m_1 and m_2 form a binary system with reduced mass μ, and the coordinate in the center of mass frame follows a circular orbit. Fixing the coordinate frame in the (x, y) plane, the coordinate of the center of mass are $x_0(t) = R\cos(\omega_s t)$ and $y_0(t) = R\sin(\omega_s t)$, with R the radius of the orbit and ω_s the radial frequency. Within the linear approximation [21], the quadrupole moment (Eq. 1.11) is:

$$Q^{ij}(t) = \mu(x_0^i(t)x_0^j(t) - 1/3R^2(t)\delta^{ij}) \tag{1.13}$$

In this simple case, in the source frame:

$$\begin{aligned} Q^{11} &= \mu(R^2\cos^2(\omega_s t) - 1/3r^2) \\ Q^{22} &= \mu(R^2\cos^2(\omega_s t) - 1/3r^2) \\ Q^{12} &= Q^{21} = \mu(R^2\cos(\omega_s t)\sin(\omega_s t) - 1/3r^2) \\ Q^{i3} &= 0 \end{aligned} \tag{1.14}$$

The GW waveforms h_+ and $h_\times$ are computed from the time derivatives of the equations above, and moving to the observer frame:

$$h_+(t) = \frac{1}{r}\frac{4G\mu\omega_s^2 R^2}{c^4}\left(\frac{1+\cos^2(i)}{2}\right)\cos(2\omega_s t) \tag{1.15}$$

$$h_\times(t) = \frac{1}{r}\frac{4G\mu\omega_s^2 R^2}{c^4}\cos(i)\sin(2\omega_s t) \tag{1.16}$$

where i is the orbit inclination w.r.t. the line of sight (see a complete description in problem 3.2 in Ref. [21]). When the orbit is face-on ($i = 0$), h_+ and $h_\times$ differ by a 90° phase shift in phase and the radiation is circularly polarized. When the orbit is edge-on ($i = \pi/2$) $h_\times = 0$,

and the GWs are linearly polarized. Intermediate values of i lead to an elliptical polarization. An important field of research is the modelling of CBC and the corresponding GW emission. Accurate waveform models are crucial to detect these signals and infer the physical parameter of the sources, as described in Sec. 2.2.

1.3.2 Continuous waves

Continuous GWs are persistent emissions expected from asymmetric rotating bodies, that have a time-varying quadrupole moment. The inertia tensor I^{ij} of the body is:

$$I^{ij} = -\int \mathrm{d}^3 x \rho(\mathbf{x})(R^2\delta^{ij} - x^i x^j) \tag{1.17}$$

with ρ the mass density and R the radius of the object. The h_+ and $h_\times$ polarizations are computed from the quadrupole moment (Eq. 1.10) that at lowest order in v/c is equal to I^{ij}:

$$Q^{ij} = -I^{ij} + \text{constants} \tag{1.18}$$

In the body frame, I^{ij} is diagonal. The GW waveform depends on the second time derivative of Q^{ij}, so the constants in the equation above can be neglected. In the simple case of a rigid body with coordinates of the body frame denoted by (x_1, x_2, x_3), rotating about one of its principal axis (x_3), the GW polarizations are (from Section 4.2. in Ref. [21]):

$$h_+ = \frac{1}{r}\frac{4G\omega_s^2}{c^4}\Big(I_{11} - I_{22}\Big)\frac{(1+\cos i)}{2}\cos(2\omega_s t) \tag{1.19}$$

$$h_\times = \frac{1}{r}\frac{4G\omega_s^2}{c^4}\Big(I_{11} - I_{22}\Big)\cos i \sin(2\omega_s t) \tag{1.20}$$

where i is the angle between the line-of-sight of the observer and the direction of the spin of the body. The equations above show that the frequency of the GW signal is twice the rotating frequency of the body ω_s. The GWs are emitted only if the quadrupole moment varies over time: in this simple case, this condition is equivalent to having the moment of inertia I_{11} and I_{22} different. Searches for continuous waves with current ground-based detectors target specific pulsars whose ω_s and sky position are known from the electromagnetic observations, and also look for generic all-sky all-frequency GW emissions. So far, no continuous GWs have been reported, yielding tight constraint on the equatorial ellipticity ($\propto I_{11} - I_{22}$). Recent results on the searches for continuous GWs can be found in Ref. [25–33].

1.3.3 Gravitational-waves stochastic background

The GW stochastic background refers to a stationary GW emission that permeates the Universe. The stochastic GW background consists of two different contributions: an astrophysical background and a cosmological one. The first originates from the superposition of several GW sources, such as transients and continuous GWs, that are not resolved individually.

The cosmological GW background is expected to originate for the early Universe. Similarly to the neutrino or the cosmic microwave background that are originated from neutrinos and photons decoupling, GW cosmological background is expected from the gravitons decoupling. Such emission should retain crucial information on gravitons' nature. The cosmological background is expected to be isotropic, stationary and unpolarized. Recent results on the search for stochastic GW background can be found in Ref. [34, 35].

Chapter 2

Gravitational-waves observations

This chapter overviews the current status of GW science, introducing the experimental set-up used to detect GWs, and presenting the main data analysis strategies employed in this domain.

GWs are detected by a network of ground-based interferometers. The sensitivity necessary to observe GWs required the construction of kilometres scale detectors, whose design and operations are complex. The key concepts of GW interferometers are presented in Section 2.1.

The detectors outputs are analysed to identify GWs among instrumental and environmental noise. Once a candidate event has been identified, the physical features of the astrophysical sources are inferred exploiting some generic or specific model of the emission, examples include the source's position and intrinsic source properties such as the masses and the spins. The data analysis workflow, that starts from the detector output up to the publication of GW transients catalogs, is presented in Section 2.2.

The treatment of these topics is clearly not exhaustive, but aims to explain the main figure of merits that are encountered in GW astronomy.

2.1 Gravitational-wave experiment

Since their discovery in 2015, GWs are observed with ground-based interferometers. This section introduces the design of Michelson interferometers (Sec. 2.1.1), and explains how this technique is used to detect GWs (Sec. 2.1.2). The response of ground-based interferometers to GWs depends on the sky localization of the astrophysical sources (Sec. 2.1.3). The principal noise sources that limit the sensitivity to GWs are overviewed in Section 2.1.4 and Section 2.1.5. More details can be found in Ref. [21].

2.1.1 Michelson interferometers

GWs are observed with interferometers. The design is essentially that of a Michelson interferometer, whose primary elements are the following: I) a coherent light beam, II) a beam splitter that splits the input light in two perpendicular components with equal amplitudes, III) mirrors that act as inertial test masses and define two orthogonal arms of about the same optical length L, and IV) a photodetector that senses the interference between recombined beams at the output of the beam splitter. A scheme of the Virgo detector is reported in Fig. 2.1. The electric field of the input laser is typically written using a complex notation as:

$$E(t, \mathbf{x}) = E_0 e^{-i\omega_L t + i\mathbf{k}_L \cdot \mathbf{x}} \tag{2.1}$$

where ω_L is the laser frequency, and k_L the wave number. We can assume the interferometer's arms are oriented along the x and y axis, with optical length L_x and L_y, respectively. The electric field at the detector output E_{out} is the sum of the field travelling in the two arms, so that the power measured at the interferometer output is:

$$P = |E_{\text{out}}|^2 = E_0^2 \sin^2[k_L(L_x - L_y)] \tag{2.2}$$

A differential variation of the arms length results in a variation of the power at the detector output. Thus, a Michelson interferometer enables to measure accurately small variations of the optical path of the light beam.

2.1.2 Effects of gravitational-waves

The effect of GWs on matter can be described in two frames: the proper detector frame and the TT gauge, introduced in the Section 1.2.

In the proper detector frame, the coordinates of the test masses are measured with a rigid ruler from an origin, typically located at the beam splitter. The effect of GWs is to shake the test masses with a different phase. Hence, the effect of GWs is a variation of the interferometer's arms that results in a variation of light intensity at the detector output (Eq. 2.2). The description within the proper detector frame is intuitive, but it is valid only under certain simple conditions.

Instead, in the TT gauge the coordinates are defined by the positions of the free-falling objects. The mirrors at the end of each arm are suspended, so that they can be considered free-falling in the horizontal plane. When a GW passes, the coordinates of the test masses do not change, but instead it is the coordinate system that is waving. The GW changes the propagation of light between the test masses, inducing a phase difference $\Delta\phi(t)$ in the beams of the interferometer that is proportional to the GW amplitude h. Considering a GW plane wave propagating orthogonally w.r.t. the plane defined by the arms of the detectors, the phase difference can be written as:

$$\Delta\phi(t) \simeq h(t - L/c)k_L \tag{2.3}$$

The phase shift can be seen also as a differential variation of the optical lengths:

$$\frac{L_x - L_y}{L} \simeq h(t - L/c) \tag{2.4}$$

Hence, GWs induce a variation of $L_x - L_y$ that results as a variation of light power at the output of the interferometer.

Eq. 2.4 indicates that, given a GW of amplitude h, the longer the optical length, the larger the displacement of the mirrors. This motivates the need of kilometre-long interferometers. In addition, Fabry-Perot cavities, mentioned in Fig. 2.1, significantly increase the interferometers' optical lengths. L sets also the wavelength of the GW λ_{GW} that can be observed: if $h(t)$ changes sign too many times during the beam travel time in the arms, the overall effect is cancelled out. Thus, the interferometers can detect GWs as long as $\lambda_{GW} \gtrsim L$. The typical light travel time inside the interferometers' arms is of the order of a few ms, which upper limits the spectral sensitivity of current detectors in the kHz range. Instead, the lower frequency corner is about 20Hz, as discussed in Section 2.1.4.

Another aspect that is important to mention is that GW interferometers are locked in the dark fringe: L_x and L_y are set so that when the beams recombine after the beam splitter, they are in destructive interference, and the light intensity measured at the output is very weak. The passage of a GW modifies the light path of the beams, and modulates the output light intensity. The almost equal optical arm lengths reduce common mode noise, such as the input power

fluctuations. Moreover, the dark fringe condition makes possible an interference measurement with almost unitary detection efficiency of photons, which allows reaching quantum noise limited sensitivities. GW interferometers are complex instruments. This section presented only the basic concepts, additional key elements that improve significantly the sensitivity to GWs are shown and briefly described in the caption of Fig. 2.1.

2.1.3 Directional sensitivity

This section discusses how the response of a GW interferometer depends on the sky localization of the astrophysical sources. The detector output is a time-series containing information on the GW polarizations $h_{+,\times}$, and on the source position thought the polar angle θ and azimuthal angle ϕ. Fig. 2.2 shows a scheme of the coordinates. The amplitude of the GWs projected in the detector basis is:

$$h(t) = h_+(t)F_+(\theta,\phi) + h_\times(t)F_\times(\theta,\phi) \tag{2.5}$$

where F_+ and $F_\times$ are the antenna responses, or antenna patterns, to the plus and cross polarizations. From geometrical considerations [21]:

$$\begin{aligned} F_+(\theta,\phi) &= \frac{1}{2}(1+\cos^2\theta)\cos 2\phi \\ F_\times(\theta,\phi) &= \cos\theta \sin 2\phi \end{aligned} \tag{2.6}$$

F_+ and $F_\times$ are between [0,1]. GW interferometers have a broad directional sensitivity, but also have blind spots, i.e. sky positions from which a potential GW signal would not be observed. For example, a GW with only plus polarization ($h_\times = 0$) coming from $\phi = \pi/4$, has $h(t) = 0$. In this case, the GW produces the same shift simultaneously in L_x and L_y, so there is no differential variation. The sky coverage can be increased observing with multiple GW interferometers with different orientations, i.e. different antenna patterns [37].

Currently, the network of ground-based GW detectors includes LIGO Livingston in Louisiana (USA), LIGO Hanford in Washington (USA), Virgo in Pisa (Italy), and KAGRA in Toyama (Japan). A large network of detectors generally improves the capability to detect and characterize GW signals [37]. More detectors increase the sky coverage, and allow observing more than one GW polarization. In addition, multiple detectors are crucial to reject instrumental and environmental noise that occur in a single detector, and that can be confused with GWs. The performance of large GW networks will be discussed extensively in Chapter 3.

2.1.4 Main noise sources

As described above, the interferometer output consists of variations of the light intensity, sensed by a photodiode. The light intensity is converted into a digital signal $s(t)$,referred to as GW *strain*, that is a combination of instrumental and environmental noise $n(t)$ and a potential GW signal $h(t)$:

$$s(t) = n(t) + h(t) \tag{2.7}$$

Section 2.2.2 will present the techniques used to distinguish $h(t)$ from $n(t)$. Here, the main noise sources that contribute to $n(t)$ are presented.

The sensitivity of GW interferometers is typically expressed in terms of noise amplitude spectral density (ASD). To define the ASD, the detector noise is assumed to be a zero-mean stationary stochastic process. The noise $n(t)$ is described by a probability distribution $p(n(t))$

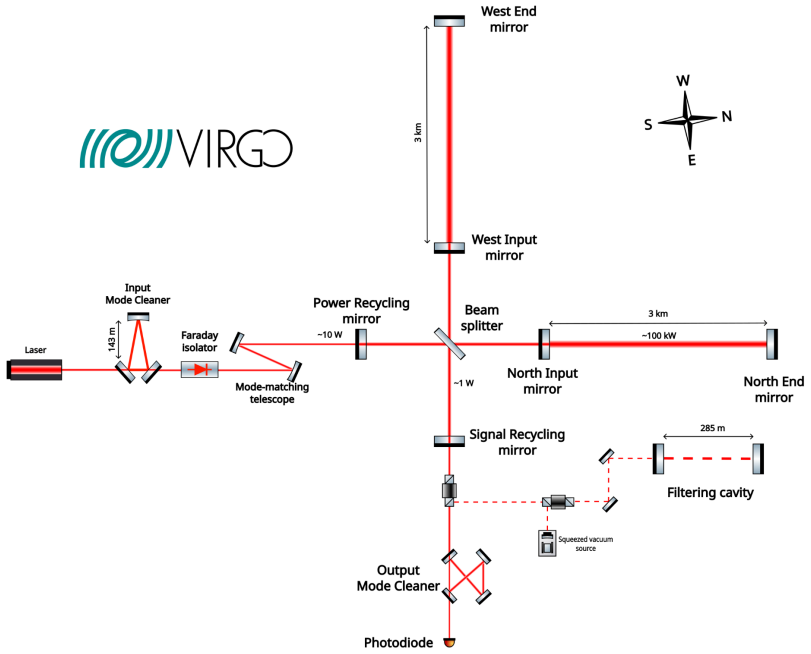

Figure 2.1: Simplified schematic of the Virgo interferometer (Courtesy of the Virgo collaboration). The test masses are indicated as "West End mirror" and "North End mirror". Next, the main optical subsystems are represented.
More details can be found in Ref. [10, 21].

Fabry-Perot cavities are present in the two arms. Each cavity consists of two mirrors, the test mass and an additional input mirror, located 3km away. The light in the cavity bounces back and forth several times. When the cavity is in resonance, i.e. the beams inside interfere constructively, the electric field is intense and the cavity is extremely sensitive to variation of its length. Given a GW amplitude h, Fabry-Perot cavities increase the phase variation (Eq. 2.3) by a factor of ~ 500.

Power recycling mirror is placed between the laser and the beam splitter. As the interferometer is locked in the dark fringe, the power that circulates in the arms goes back into the laser. The power recycling mirror reflects the light into the interferometer, increasing the circulating power by a factor ~ 100, improving in turn the sensitivity to GWs (Section 2.1.4).

Signal recycling mirror is placed between the beam splitter and the photodetector. Depending on its configuration, it improves the sensitivity to GWs at specific frequencies, or it enlarges the interferometer bandwidth.

Input mode cleaner is a triangular cavity located after the laser, that removes the high order modes of the input light. A beam with finite transverse extension can be treated as a Gaussian beam plus higher order modes. These last are not in resonance in the Fabry-Perot cavities, and decrease the sensitivity to GWs.

Output mode cleaner similarly to the input model cleaner, it filters out the higher order modes of the output beam. Even if the beam after the input mode cleaner contains only the Gaussian modes, optics misalignment and imperfections generate additional high order modes.

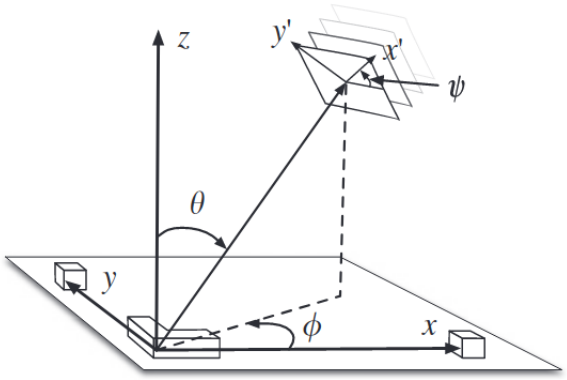

Figure 2.2: Scheme of the coordinates used to derive the antenna responses in Eq. 2.6. The interferometer arms are along the x and y axis, the beam splitter is at the origin and the test masses are indicated by white cubes. The position of the GW source is specified by the polar angle θ and the azimuthal angle ϕ [36].

[38]:

$$p(n) = \mathcal{N} \exp\left\{ -\frac{1}{2} \sum_{i,j} (n_i - \mu)(n_j - \mu) C_{ij}^{-1} \right\} \tag{2.8}$$

where μ is the mean and C_{ij} is the covariance computed at samples i, j. For stationary noise, C_{ij} depends only on the lag $|i - j|$. Transforming to the Fourier domain where i, j indicate to frequencies f_i, f_j, the stationary noise has a diagonal covariance matrix $C_{ij} = \delta_{ij} S_n(f_i)$ that defines the power spectral density (PSD). The noise ASD is simply $\sqrt{S_n(f_i)}$, and has dimension $\mathrm{Hz}^{-1/2}$. $S_n(f)$ is measured from the data using Welch's method [38]: the time-series $s(t)$ is divided into overlapping segments and windowed. Then for each segment, the Fourier transform is performed, and the square magnitudes are averaged.

Fig. 2.3 presents the ASD for Advanced Virgo at the beginning of the third observing run (O3), and the various contributions to the noise budget. The frequency bandwidth of current GW detectors is between 20Hz and 4000Hz. The best sensitivity is achieved for frequencies around $\sim$ 100 Hz, which is where the observed BBH mergers signals stand. The main noise sources are:

- **Quantum noise** consists of two contributions: shot noise and radiation pressure. The first is due to the fluctuations of the number of photons that arrive at the photodetector. Shot noise limits the interferometers' sensitivity at high frequencies. The more photons arrive, the lower the relative error on their number. Hence, shot noise is mitigated increasing the light power circulating in the interferometers arms.

  The second contribution arises from radiation pressure, i.e. the pressure exerted by the photons on the mirrors. The fluctuations of the number of photons on the mirrors result into a white stochastic force that shakes the mirrors. The resulting displacement of the mirrors has a red spectrum. The more the laser power, the stronger this spurious force.

  Radiation pressure and shot noise depend on the laser power proportionally and inversely proportionally. This effect, referred to as quantum noise, is a manifestation of the uncertainty principle: GW detectors use photons to measure the position of an object. At the

same time, the photons give a non-determinist recoil to the object, and the recoils affect the measure itself.

Quantum noise seems to constitute a fundamental limit to GW detector sensitivity. However, current detectors go beyond the quantum noise injecting squeezed states at the detector output [39–41]. Squeezed states are states of the light in which the uncertainty in one of the two quadratures (in-phase and quadrature phase) is decreased, while the other is increased, always satisfying the Heisenberg uncertainty principle. More details can be found in Ref. [42].

- **Seismic noise** Earth's ground vibrates continuously, shaking the test masses. These fluctuations mimic the effect of GWs. To mitigate this noise, in Virgo, the test masses have a specific passive-active attenuator system, composed of a 6m long inverted pendulum, and several stages of suspensions [42]. The attenuation factor is proportional to $(f_0/f)^2$ for frequencies $f \gg f_0$. The resonant frequency f_0 is ~ 0.6Hz. The other optics are suspended as well.

- **Thermal noise** LIGO and Virgo detectors operate at ambient temperature, so their mirrors and suspensions experience Brownian motion [43]. The thermal noise affects the properties of the mirrors coatings, induces fluctuations on the suspensions, and on the test masses, contributing significantly to the total detector noise. In addition, the fluctuations of the normal modes of the suspensions wires cause a set of spikes at specific frequencies, as shown in Fig. 2.3. To reduce the impact of this noise source, KAGRA detector is operating at cryogenic temperature.

- **Newtonian noise** Variations in the density of the atmosphere and of the ground lead to fluctuations in the Newtonian gravitational force that acts on the test masses. This noise contribution can be measured with arrays of seismometers, and eventually subtracted from the detector output [44]. Future generation detectors will operate underground to reduce the impact of this noise.

2.1.5 Short-duration transient noise

One of the major challenges for both detector and data-analysis experts is represented by short-duration disturbances, called *glitches*, which occur with both high amplitude and high rate. During the third observing run, the median rate of glitches with signal-to-noise ratio (SNR) >6.5 was $\sim 0.3\text{min}^{-1}$ in LIGO Hanford, $\sim 1\text{min}^{-1}$ in LIGO Livingston and 0.8min^{-1} in Virgo [1, 23]. Such noise can mimic GW transients, increasing the false alarm rate of GW searches. Moreover, if the transient noise overlaps with astrophysical signals, it might reduce the search sensitivity [45], affect the estimation of the properties of the source [46], their sky localization [47], and the studies performed to test the validity of General Relativity [48].
Glitches are due to the instrument itself and by its interaction with the environment [49, 50]. The ideal strategy to reduce their occurrence is to identify their origin and solve the causes [51]. Thousands of *auxiliary channels*, i.e. sensors used to monitor the state of the instruments and the environment such as microphones, seismometers [52], are acquired to understand the correlations between the detector state and the detector output. A funny example is the case of Raven glitches: in 2016 some glitches turned out to be associated with signals recorded by a microphone located in the surroundings of the LIGO Hanford detector. The strokes were due to a couple of ravens picking on the ice that covered the cooling system. An adjustment in the set-up prevented the ice build up, and simply solved the cause of some glitches!

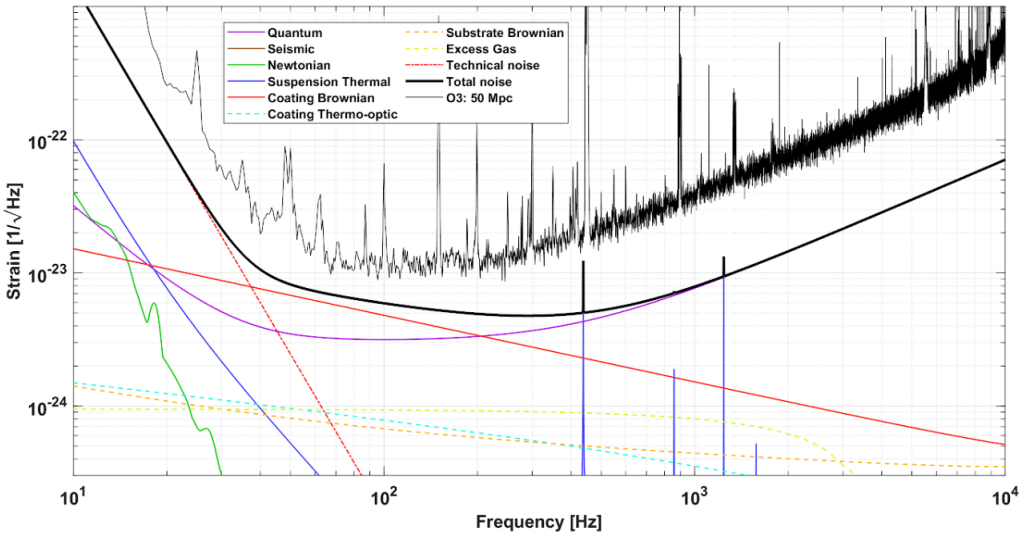

Figure 2.3: Sensitivity of Advanced Virgo, in terms of noise ASD, at the beginning of the third observing run in black thin line. Anticipated best sensitivity for Advanced Virgo (Phase I) in black bold line. The contributions of the main sources of noise are highlighted in colours [42].

If it is not possible to identify the root cause, but the coupling between the source of the transient noise and the detector output $h(t)$ is known, periods of data between seconds to hours can be excluded. Instead, if the coupling is not completely understood, the glitches cannot be vetoed safely as this may remove accidentally true GW signals. The identification and characterization of glitches is therefore crucial for GW data analysis. Several methods have been proposed in the latest year to address this problem. As glitches appears in huge quantities and they exhibit a large variety of morphologies, machine learning approaches emerge as essential [53]. Many studies focus on glitch classification into classes (or families) according to their signature in time-series [54, 55] or in time-frequency evolution [56, 57]. Glitch mitigation for GW transients searches will be addressed in Chapter 6.

2.2 Data analysis techniques

This section introduces the main analyses that lead to the production of GW catalogs [1] that contain the collection of GW detections, and the properties of each source.

First, the detector output needs to be calibrated (Sec. 2.2.1). The resulting signal contains both potential GW events and instrumental and environmental noise. Detection algorithms identify GW signals, and assign a significance, i.e. a probability that the signal under investigation is a genuine astrophysical signal (Sec. 2.2.2). If the significance is above a certain threshold, and the data around the time of the potential event is clean, the signal is considered a GW candidate (Sec. 2.2.3). The sources parameters, such as the objects' masses and spins in case of CBC signals, are estimated (Sec. 2.2.4). Lately, since the number of GW observations is continuously increasing, it is possible also to perform statistical studies on the population of the observed GW sources (Sec. 2.2.5).

2.2.1 Calibration

The effect of GWs on the interferometers is to generate a phase shift between the beams that travel in the two orthogonal arms, which is read by a photodetector at the detector output (Section 2.1.2). In order to extrapolate robust astrophysical results, it is fundamental to characterize the uncertainties and the biases associated with the detector measurement. The uncertainties in the amplitude and in the phase of the output signal impact the detection of GW events, the estimates of the physical parameters of the GW sources, and limit the capability to test GR [58].

The quantification of the detectors' response to GWs is referred to as calibration [59, 60]. The calibration errors include statistical errors, due to the intrinsic uncertainty associated with the measurements, and systematic errors, i.e. potential biases between the model of the transfer function of the detector's systems and the measurements.

GW interferometers are complex instruments, and have various feedback control loops to maintain the detectors at the working point. Various optical cavities have to be hold in resonance (see Fig. 2.1), and the suspensions of the test masses, needed to reduce the seismic noise, have active independent actuators. To control the length of the arms, in Virgo an electric current in wire coil magnets is used to control the position of the test masses. The response of these actuators is evaluated using an additional laser, called photon radiation pressure actuator, directed into the test masses. The recoil of the photons from this laser, induces a force in the mirrors. A know excitations is applied to the test masses, and the response of the detector output enables to measure the interferometer transfer function. Calibration injections are repeated at various frequencies during the whole observational run to characterize the time dependence of the calibration.

The calibration uncertainties for LIGO detectors in the frequency range between 20Hz and 2000Hz during the third observing run were$<$ 7% in amplitude and $< 4°$ in phase (O3a) [59], and $< 12\%$ in amplitude and $< 10°$ in phase (O3b)[61]. In Virgo, the calibration uncertainties were $< 5\%$ in amplitude and $< 2°$ in phase [62, 63].

2.2.2 Detection

The detector output $s(t)$ is a combination of potential GW signals $h(t)$ and detector noise $n(t)$ (Eq. 2.7). This section overviews the main techniques used to search for GW signal $h(t)$ embedded in the noise, and to evaluate the probability that it is a true astrophysical signal. There exist two approaches to detect a GW signal: template-based methods, which assume some knowledge on the form of $h(t)$, and unmodelled methods, which are agnostic on the waveform model. In the following, we introduce briefly template-based searches, while unmodelled searches of GW transients are the focus of this thesis, and they will be discussed in great detail in the next chapters.

Typically, template-based searches are based on matched filter technique. The idea is to apply to the detector output $s(t)$ a filter function $K(t)$:

$$\hat{s} = \int_{-\infty}^{\infty} dt\ s(t)K(t) \tag{2.9}$$

The filter is chosen to maximize the SNR, defined here as S/N. S is the expected value of $\hat{s}$ when a GW is present:

$$S = \int_{-\infty}^{\infty} dt\ \langle s(t)\rangle K(t) = \int_{-\infty}^{\infty} dt\ h(t)K(t) = \int_{-\infty}^{\infty} df\ \tilde{h}(f)\tilde{K}^*(f) \tag{2.10}$$

in the equation above the noise is assumed to be stationary, so $\langle n(t)\rangle = 0$. N is the root-mean-square of $\hat{s}(t)$ when there is no GW signal:

$$N^2 = (\langle \hat{s}^2(t)\rangle - \langle \hat{s}(t)\rangle^2)_{h(t)=0} = \langle \hat{s}^2(t)\rangle_{h(t)=0} = \int_{-\infty}^{\infty} dt dt'\ K(t)K'(t)\langle n(t)n(t')\rangle = \int_{-\infty}^{\infty} df \frac{1}{2} S_n(f)|\tilde{K}(f)|^2 \tag{2.11}$$

where the last equality uses $\int_{-\infty}^{\infty} df df' \langle \tilde{n}^*(f)\tilde{n}(f')\rangle = \int_0^{\infty} df S_n(f)$ [21]. The filter that maximizes the SNR is [21]:

$$\tilde{K}(f) = \text{const}\ \frac{\tilde{h}(f)}{S_n(f)} \tag{2.12}$$

The meaning of the above equation is simply the following: if the noise is white the signal itself is the best filter, if the noise depends on the frequency, as in the case of GW detectors (see Fig. 2.3), noisy frequency regions have to be weighted less. So, when searching for a GW signal with matched filter technique, the filter $\tilde{K}(f)$ is applied to the data $s(t)$, and the corresponding SNR is computed.

However, there is not a single form of the GW signal to filter the data with, because $h(t)$ depends on several physical parameters $\boldsymbol{\theta}$. In the case of GWs from CBC, the GW waveform depends on at least 15 parameters: the masses of the two objects, their spins (3 degrees of freedom for each object), the location (luminosity distance and two angles), the orientation (inclination angle and polarization), the time and the orbital phase at which the signals enter the detectors' bandwidth. The search algorithms based on matched filtering build extensive template banks, containing up to several millions of possible $h(t, \theta_i)$ waveforms, covering a broad astrophysical parameter space. All the templates are applied to the data, and the corresponding SNR is computed. The segments of data for which the SNR is higher than a certain threshold are selected.

The next step is to estimate the significance of each trigger, i.e. the probability that it is a genuine astrophysical signal, and not a terrestrial disturbance. The SNR distribution of Gaussian noise drops rapidly for high values of SNR. Hence, setting a sufficiently high threshold on the SNR corresponds to setting a threshold on the false alarm rate (FAR) [21]. However, GW detectors contain short-duration disturbances, called glitches (see Section 6.1). Thus, selecting a large threshold on the SNR does not assure that the glitches are removed from the list of potential GW candidates.

To distinguish glitches from astrophysical signals, data from different GW detectors are combined: a trigger that is observed only in one detector more likely originates from a local disturbance, while an astrophysical event is expected to be observed in more than one detector with similar characteristics. To account for glitches, the significance is estimated building a background distribution using time-shifted data: the data of one detector are time-shifted by an amount larger than light travel time between the detectors w.r.t to the other detector(s) data. The detection algorithm is applied to the time-shifted data, and the triggers that are found by construction cannot have an astrophysical origin. Next, each trigger identified in the on-source data is compared with the background distribution and its significance is estimated. This procedure is explained in more details in Section 4.1.5.

Recently, several works have proposed machine learning (ML) techniques to perform template-based searches. An overview is presented in Ref. [53]. The basic idea is to perform a binary classification between a signal and a noise class. The training dataset is typically built using GW simulations, while the noise population is learned from simulated Gaussian noise or from

background distribution. The signal-noise classification can be performed with several ML techniques such as decision-tree learning, and deep-learning algorithms such as convolutional neural networks. The input data can be either in the form of time-series or image, using the time-frequency representation of $s(t)$ as show in Fig. 1.1.

Section 1.3 overviewed the sources of GWs, and identified three main types of signals: transients GWs, continuos GWs, and the stochastic GW background. For each type, different detection and noise mitigation strategies have been developed. More details on the template-based algorithms employed for CBC detection within the LVK collaboration can be found in Ref. [64–67].

2.2.3 Event validation

Once a detection algorithm has identified a trigger with a FAR below a certain threshold, several checks are performed to assess the quality of the data around the time of the event [68]. These investigations are fundamental to increase the confidence that the trigger has an astrophysical origin, and to infer accurately the physical parameters of its source. The presence of instrumental or environmental artefacts is monitored performing tests of stationarity and Gaussianity on the data, and looking for correlations between $s(t)$ and the auxiliary sensors that monitor the status of the instruments and of the environment [49, 50]. During an observational run, such tests are done automatically in a couple of minutes. A rapid-response-team controls the results and, if positive, the trigger is considered a candidate GW event. Further tests are performed in higher latency, if necessary.

2.2.4 Estimation of the sources parameters

The estimation of the physical parameters of the GW sources is a fundamental analysis that enables testing GR, and has important implications for astrophysics and cosmology. For example, in the case of GWs originated by CBC, from the luminosity distance and some knowledge of the cosmological redshift it is possible to measure the Hubble constant [69], and from the masses and the spins, it is investigated the formation channels of binary systems [16].

The parameter estimation (PE) routines generate posterior distribution for the physical parameters of the sources. The most common approach to perform PE is Bayesian inference, see Ref. [70] for a review. As defined before, $s(t)$ is the measured data, and $\boldsymbol{\theta}$ the unknown parameters that describe the GW signal $h(t, \boldsymbol{\theta})$. The uncertainty on $\boldsymbol{\theta}$ before making an experiment is the prior probability density function $\pi(\boldsymbol{\theta})$. Typically, prior distribution are chosen uniform in a range in which the waveform approximants is accurate. The Bayes theorem states that the posterior distribution, i.e. the probability of a set of parameters given the observation, is:

$$p(\boldsymbol{\theta}|s) = \frac{\text{likelihood} \cdot \text{prior}}{\text{normalization const.}} \propto p(s|\boldsymbol{\theta})\pi(\boldsymbol{\theta}) \tag{2.13}$$

The likelihood $p(s|\boldsymbol{\theta})$ is defined from the probability distribution of the noise $p(n)$, assuming the noise is stationary and Gaussian:

$$p(n) = \mathcal{N} \exp\left(-\frac{1}{2} \int_{-\infty}^{\infty} df \ \frac{|\tilde{n}(f)|^2}{1/2S_n(f)} \right) = \mathcal{N} \exp\left(-\frac{1}{2}(n|n) \right) \tag{2.14}$$

where the equation above introduces, to simplify the notation, the scalar product $(A|B) = 4\text{Re} \int_0^{\infty} df \tilde{A}^*(f)\tilde{B}(f)/S_n(f)$ [21]. If a GW signal with parameters $\boldsymbol{\theta}_t$ is present, the detector output is $s(t) = h(t, \boldsymbol{\theta}_t) + n(t)$, and Eq. 2.14 becomes:

$$p(s|\boldsymbol{\theta}_t) = \mathcal{N} \exp\left(-\frac{1}{2}(s - h(\boldsymbol{\theta}_t)|s - h(\boldsymbol{\theta}_t)) \right) \tag{2.15}$$

Once the posterior distribution is obtained, the most probable, or maximum a posteriori, value $\hat{\theta}_i$ of each parameter is computed integrating the posterior distribution:

$$\hat{\theta}_i = \int d\theta \; \theta_i p(\theta|s) \tag{2.16}$$

Typically, the uncertainties on the PE estimates are reported in terms of the 90% credible intervals.

Fig. 2.4 shows the posterior distributions for the masses, and the luminosity distance and orbit inclination for the first GW observation, GW150914 [22]. The figure shows the results derived using two waveform approximants, based on different analytical and numerical methods.

The PE of each GW event detected are reported in the GW catalogs [1, 23, 24]. As the detectors sensitivity is increasing and so the number of GW observations, alternative methods w.r.t. Bayesian inference are under investigation. Indeed, the latter has a large computational cost: the evaluation of the most probable values requires the multidimensional integration of the likelihood over the space of the parameters $\boldsymbol{\theta}$. As mentioned before, the parameters that characterize a CBC are at least 15.

Novel ML-based methodologies show to be much faster: algorithms such as normalizing flows [71, 72] or variational autoencoders [73] can be trained to learn posterior distributions. The training dataset typically contains a set of parameters $\boldsymbol{\theta}$ and their corresponding GW waveforms $h(t, \boldsymbol{\theta})$.

Once PE is done, the GW waveform generated with the parameters inferred is compared with the measured data to check that they are consistent. Potential discrepancies may arise from detector noise, missing physics in the models, or deviations from GR. Such analysis will be discussed in Section 7.1.2.

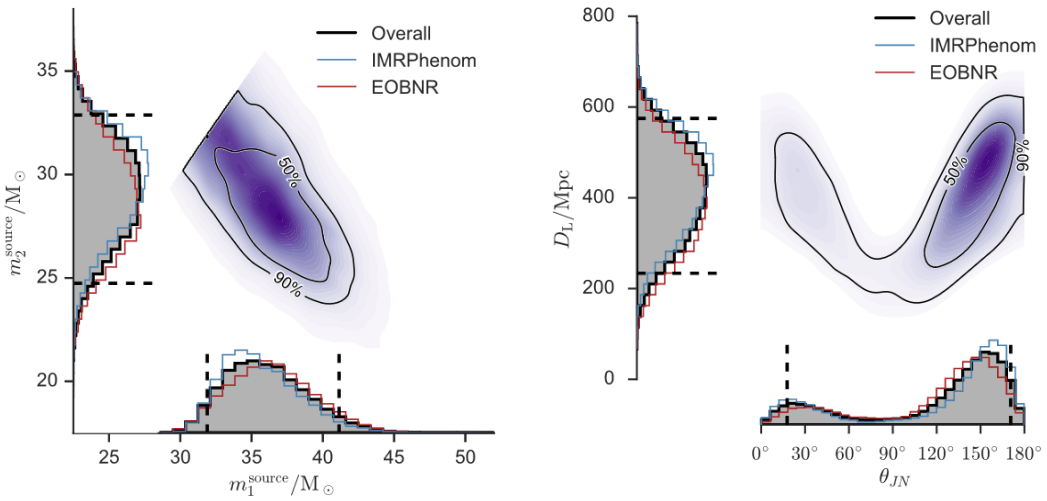

Figure 2.4: (*left*) Posterior distribution for the source-frame component masses m_1^{source} and m_2^{source}. The frequency of the signal $s(t)$ is redshifted by a factor $(1+z)$, where z is the cosmological redshift. Thus, the measured redshifted masses m are related to the source-frame masses as $m = (1+z)m^{\rm source}$. (*right*) Posterior distribution for the source luminosity distance D_L and the inclination of the orbital plane θ_{JN}. D_L is correlated to the source inclination. Both figures report the results obtained with two waveform approximants (IMRPhenom in blue, and EOBNR in red). The dashed vertical lines mark the 90% credible interval [22].

2.2.5 Population of merging compact binaries

As the number of GW observations increases, it is possible to use statistical methods to infer the characteristics of BHs and NSs in binary systems, and estimate how often they merge. These findings have significant astrophysical implications, for example, probing the formation channels and the evolution of binary systems. The two main formation channels of compact binary systems are the isolated evolution of massive binary stars, and the dynamical formation in dense stellar environments. Another formation channel involves primordial black holes. Each scenario predicts different parameters' distributions: the isolated evolution scenario, for example, is expected to produce nearly aligned spins and an upper limit on the component masses from the pulsational pair-instability supernova process.

To estimate the parameters of BBH and BNS populations from GW observations, a hierarchical Bayesian approach is used. The framework is briefly presented next, a complete description can be found in Ref. [16]. The data from N_{det} CBC detections is indicated as $\mathbf{d}$. N_{det} follows a Poisson process with expected events $N\epsilon(\Lambda)$, where N is the total number of events expected during the observational period and $\epsilon(\Lambda)$ is the fraction of CBC systems detectable with current interferometers from a population with parameters Λ. The selection effect $\epsilon(\Lambda)$ is estimated injecting GW waveforms in data and counting the simulation recovered. The posterior distribution of the population parameters is given by [70]:

$$p(\Lambda, \boldsymbol{\theta}, N|\boldsymbol{d}) \propto (N\epsilon(\Lambda))^{N_{det}} \exp^{-N\epsilon(\Lambda)} \prod_{i=1}^{N_{det}} p(\boldsymbol{d}_i|\boldsymbol{\theta}_i)\pi(\boldsymbol{\theta}_i|\Lambda)\pi(\Lambda)\pi(N) \tag{2.17}$$

where $p(\boldsymbol{d}_i|\boldsymbol{\theta}_i)$ is the likelihood of the i event given the PE $\boldsymbol{\theta}_i$. $\pi(\boldsymbol{\theta}_i|\Lambda)$, $\pi(\Lambda)$, and $\pi(N)$ are the priors on the individual event parameters, and on the population parameters. There are several models with different degree of complexity to describe $\pi(\boldsymbol{\theta}_i|\Lambda)$, focusing especially on the distributions of the masses and the spins. A common model for the masses distribution is the power law + peak distribution, where the mass distribution is modelled with eight parameters that fix two hard cut-offs on the minimum and maximum mass allowed, and a Gaussian peak to address the excess of events due to the upper limit mass from the pair-instability supernovae.

Marginalizing over $\boldsymbol{\theta}$ and N returns the posterior $p(\Lambda|\boldsymbol{d})$. Eq. 2.17 can also be marginalized over Λ, and all the parameters $\boldsymbol{\theta}$ except one. The resulting distribution $p(\theta_j|\boldsymbol{d})$ represents our best guess for the astrophysical populations of the parameter θ_j, given a certain model. Fig. 2.5 shows the differential merger rate for the primary mass of the binary black holes, predicted using different models for the prior $\pi(\boldsymbol{\theta}_i|\Lambda)$.

These models enable the estimation of the merger rate from the GW catalogs [16]. From the third observing run, the BBH merger rate is between 17.9 $\mathrm{Gpc}^{-3}\mathrm{yr}^{-1}$ and 44 $\mathrm{Gpc}^{-3}\mathrm{yr}^{-1}$, and for BNS is between 10 $\mathrm{Gpc}^{-3}\mathrm{yr}^{-1}$ and 1700 $\mathrm{Gpc}^{-3}\mathrm{yr}^{-1}$.

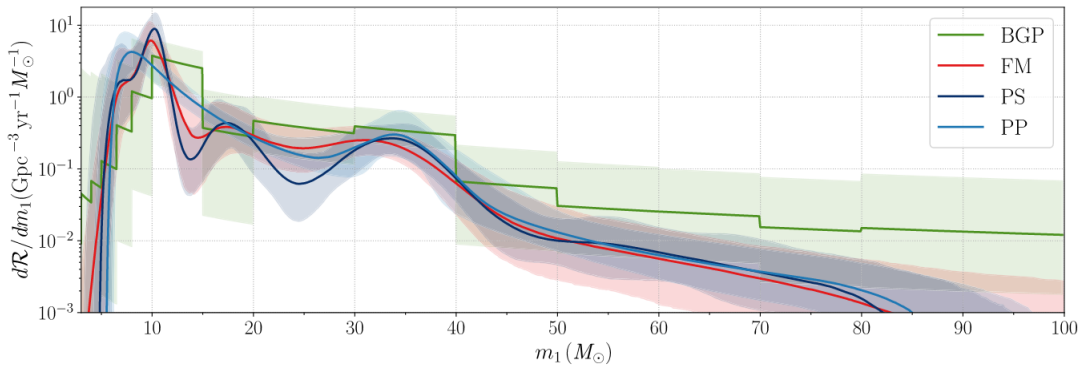

Figure 2.5: Differential merger rate for the primary mass of BBH predicted using different models (parametric power law + peak model (PP); non-parametric prior models power law + spline (PS), flexible mixture (FM), binned gaussian process (BGP)). The comparison of different models is beyond the scope of this section. It is interesting to note that the mass distribution has localized peaks at $\sim 10M_\odot$ and $\sim 35M_\odot$, and there is inconclusive evidence for an upper mass gap at $50M_\odot$ [16]

Chapter 3

Sources of gravitational-wave transients

The core of this thesis is the detection and the reconstruction of GW transients (or GW bursts) by using methods which make only generic assumptions on the source. In particular, such methods are either fully agnostic to the signal waveform or at most weakly informed of its time-frequency characteristics. We will refer to these methods in the following as "unmodelled". Burst searches identify in the detector data excess of power, i.e. signals with amplitude above the detector noise baseline, and distinguish genuine GWs from transient noise using the coincidence and/or the coherence among multiple GW detectors. A technical description of an algorithm used for burst searches is provided in the fourth chapter.

This chapter presents several astrophysical sources that emit or are expected to emit GW transients and that can be observed with an unmodelled approach. First, burst searches detect GWs from CBC, and played a fundamental role in the detection of the first GW event (Section 3.1). The sensitivity to these sources is lower w.r.t. template-based algorithms, but burst algorithm can also detect CBC with peculiar characteristics, or GWs from CBC that have been perturbed during their propagation.

In addition, several interesting astrophysical sources are expected to emit GWs but the waveforms are not known accurately, or their availability is limited. Among these sources there are core collapse supernovae (Section 3.3), isolated neutron stars (Section 3.4), cosmic strings (Section 3.5) and dark matter (Section 3.6). For each source, the main state-of-the-art results are presented.

3.1 Compact binary coalescences

The LVK collaboration reported about 90 GWs signals originated from the coalescence of compact binaries [1]. The first GW observation, GW150914, was made in low-latency by a burst search, and subsequently was found also by matched-filter analyses. Nowadays, CBC sources are modelled accurately, and template-based searches have a better sensitivity toward CBC w.r.t to burst searches. Indeed, if the GW waveform is known the matched filter, presented in Section 2.2.2, is the optimal technique to identify a signal. Instead, burst searches being sensitive to a wide range of possible signals, have a higher false alarm rate than template-based methods, and so their detection capability towards CBC is lower. Fig. 3.1 shows the GW events identified with template-based and unmodelled searches from 2015 to 2020. Burst searches have detected the

majority of the CBC events with SNR above 15, and template-based searches detect significant GW events also at lower SNR. The figure shows also the distribution of the total mass and the luminosity distance of GWs observed so far.

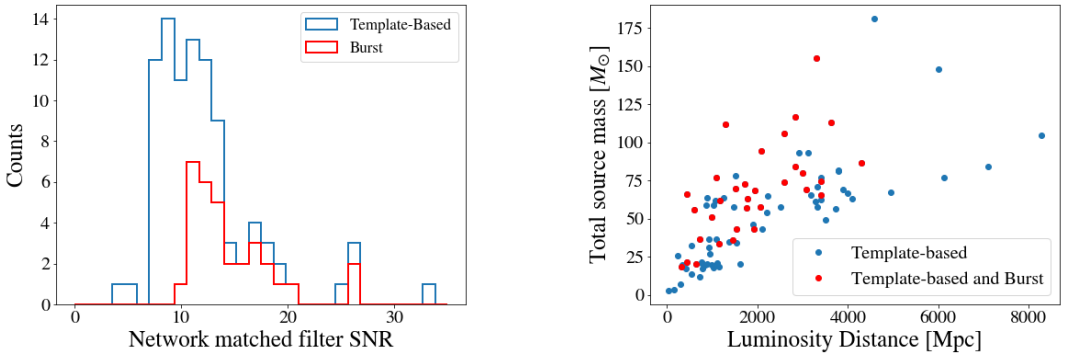

Figure 3.1: GW events originated from CBC identified only by template-based searches (blue), and by template-based and burst searches (red). (*left*) Histogram of network matched-filter SNR. Red indicates the events found by burst searches. The loudest events (SNR >24) are: GW150914 and GW190521 detected by both searches. The highest SNR event is GW170817 originated from the coalescence of two neutrons stars. It was not observed with burst searches due to its long duration. The other two loud events are GW190814, that was not observed with burst searches because LIGO Hanford was not in science mode, and GW200129 for which the data from LIGO Livingston had quality issues and were not used by burst searches. (*right*) Luminosity distance versus total source mass. Data are taken from the LVK catalogs [1, 23, 24].

Burst searches are crucial to identify and characterize the so called 'non-vanilla CBC', i.e. CBC with particular features such as physical parameters out of the parameter space covered by the waveform models, or systems with complex dynamics. The main phenomena that are expected to modify the GW waveforms of CBC and may be identified with burst searches are:

- **Orbital eccentricity**
  The GWs detected so far are consistent with quasi-circular CBC [1]. A feature that is difficult to study and measure is the orbital eccentricity. There is no confident detection of an eccentric BBH, but alternative interpretations of GW190521 as an eccentric BBH have been published [74, 75]. Orbital eccentricity is fascinating because it would be a signature of a dynamical formation channel of binaries or other non-standard scenarios. Several studies predict the formation of eccentric BBH in dense star clusters, with orbital eccentricity present up to the merger time, when the signal enters the GW detectors frequency band [76–78]. However, eccentric BBH detection is challenging. To date, eccentric waveforms are not included in template banks, and Ref. [79] shows that quasi-circular banks are not effective when searching for eccentric BBH, as the overlap between quasi-circular and eccentric waveform decreases with increasing eccentricity. This is clear looking at Fig. 3.2 that shows a comparison between a GW waveform with negligible[1] and moderate eccentricity for a BBH system with total mass of $50M_\odot$. The two waveforms are significantly different: the

[1]There are several possible estimators of eccentricity. Eccentricity equal to 0 indicates circular orbit, while eccentricity equal to 1 head-on collision. The precise definition of eccentricity is beyond the scope of this section. Figure 3.2 aims to show an example of a GW waveform in case of negligible and moderate eccentricity.

eccentricity induces a rapid dephasing and strong modulations of the GW amplitude during the inspiral phase, due to the time-dependent orbital velocity of the eccentric orbit. The inclusion of eccentric waveform in the template banks reduces the capability of rejecting transient noise, limiting the sensitivity to non-eccentric CBC signals [80]. Hence, burst algorithms are crucial to search for BBH system with high eccentricity. Ref. [81] presents the search for eccentric BBH in the third observing run using an unmodelled algorithm, and no eccentric BBH candidate event have been reported.

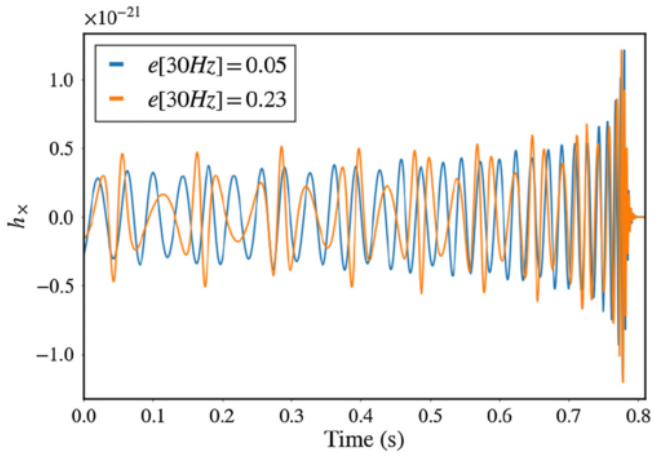

Figure 3.2: GW waveform $h_\times(t)$ for a BBH with total mass $M_{tot} = 50M_\odot$ with low eccentricity (blue) and moderate eccentricity (orange). The GW waveforms are computed with numerical-relativity simulations [80].

- **GW memory**
  GW memory indicates a permanent deformation of the spacetime after the passage of GWs. The effect of GW memory is to generate a difference in the GW amplitudes at late and early times w.r.t. the GW event. The most prominent type of GW memory is non-linear memory, also referred to Christodoulou memory [82]. Non-linear memory is related to the non-linearity of GR: it is not produced by the GW source itself but is rather an effect of the GW radiation. Hence, all sources of GWs are subjected to the memory effect. Most of the literature on modelling and searching for GW memory is related to CBC signals, see Ref. [83] for a review. The amplitude of the memory signal is much lower than the inspiral and merger part. To understand the effect of GW memory on GW interferometers, one has to remember that the test masses located at the ends of each arm cannot be considered in free-fall at low frequencies because they are maintained at the operating point by the control systems (see Section 2.2.1). Fig. 3.3 shows the GW memory associated to a CBC system: the memory signal is expected to increase monotonically during the inspiral phase, exhibits a jump during the merger, and saturates at the ringdown. As the current ground-based interferometers have a low-frequency cutoff at around 10Hz, the GW memory appears as a single cycle burst signal. The duration depends on the masses of the compact objects involved: heavier systems produce longer signals.
  Memory is an interesting source of GWs: it can be used to search for subsolar mass CBC, especially in the cases of very light systems ($M_{tot} < 0.4M_\odot$), whose merger signal is above the bandwidth of current detectors and the chirping signal is too weak to be detected in

the audio band [84]. Moreover, GW memory may be used with third-generation detectors to distinguish NSBH binaries from BBH [85].

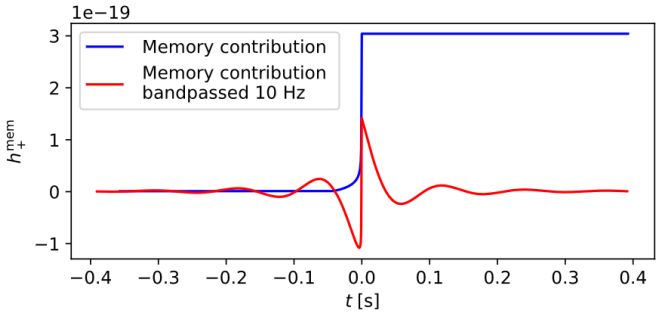

Figure 3.3: GW memory waveform in the case of a merger between two $1M_\odot$ BHs at a distance of 10kpc. The GW memory (blue line) appears as a GW amplitude difference before and after the merger time ($t = 0$). The low frequency cutoff due to the GW detector makes the signal appear as a GW burst (red line). This plot shows only the memory effect, the inspiral and merger amplitudes are much greater [84].

- **Lensing**
  Once GWs are emitted, they propagate outward at the speed of light. The cross-section of matter for GWs is extremely small [2], so GWs travel without being absorbed. However, galaxies and clusters of galaxies can act as gravitational lens, modifying the GWs while they travel in the space and producing multiple magnified and delayed images of the same GW signal. Lensing may limit the detection capabilities of template-based searches.

  Typically, lensed GW events are expected to have identical source parameters, with differences only in the inferred luminosity distances. Ref. [86] shows that lensing can also induce frequency-dependent phase shifts, resulting in a distorted waveform. For a wide range of the CBC parameter space, the SNR loss using an unlensed template banks when looking for a lensed signal is just a few percent. However, under certain conditions as CBC with higher modes, orbital precession and orbital eccentricity, the lensed image could have distorted waveforms and may not be detected by template-based searches [87]. In these cases, burst searches are necessary.

- **Alternatives theories to GR**
  GW observations allow testing GR in extreme regimes with an unprecedented accuracy. In particular, CBC are ideal systems to test strong-field GR [88, 89]. Recent results performed on GW observations can be found in Ref. [15]. Alternative theories of gravity propose modified gravitational dynamics, additional GW polarization modes [90], and the existence of exotic alternatives to BH, referred to as black hole mimickers. The GWs originated from the coalescence of BH mimickers can be confused with that from standard BHs. However, there are several features that distinguish the two [88, 89], as the mass-spin distribution inferred from GW signals, the presence in the GW waveform of spin-induced deformations [91, 92] or of tidal deformability [93]. Moreover, exotic compact objects may emit GW echoes, i.e. repeated GW transients occurring shortly after the BBH mergers, originated

[2] For comparison, the mean free path for photons in the Sun is of the order of cm, while for gravitons is about a factor 10^{80} higher. So the Sun is completely transparent to the GW radiation.

as echoes of the remnant object [94]. Such an outgoing GW radiation violate GR because it implies that the BH remnant is not fully absorbing. Theoretical GW echoes waveforms show a large variety of morphologies. Ref. [95] proposes an umodelled search for these signals on the post-merger of the detected CBC signals, and places upper limit values of the GW strain $h(t)$ and the energy that would have been detectable, achieving sensitivity at least competitive to that of template-based searches.

The characterization and the modelling of GW waveforms of alternative theories and of the merger of BH mimicker is still under development, thus burst searches are needed to identify unexpected signature in GW data, or in case of null measurement, to place constrains to alternative models.

Another possible situation in which GW waveforms may be distorted limiting the sensitivity of template-based methods is the overlapping of multiple CBC signals. As the detectors improve sensitivity, especially considering third-generation detectors, more likely CBC will overlap. In Ref. [45], the author of this thesis and collaborators investigate how the current template-based and burst searches behave with overlapping signals. The findings, reported in Appendix A, show that both approaches are able to identify overlapping signals until the time interval between the two merger times is larger than 1s. For closer signals, both approaches individuate just one signal by construction. Interestingly, the unmodelled algorithm reconstructs the secondary signal as uncoherent noise, suggesting that future developments could allow for the estimation of both signals.

3.2 Hyperbolic encounters

In dense stellar clusters, like galactic nuclei and globular clusters, compact objects are expected to encounters following hyperbolic orbits [96]. When the masses of the compact objects are between few and a hundred of solar masses, such scattering events may manifest as GW bursts in the frequency of current ground-based detectors [97]. The energy released in GWs depends mainly on the periastron distance and on the masses of the objects involved.

Hyperbolic encounter between compact objects are of great interest to investigate dense stellar environments [98], and primordial BH populations [99].

The seventh chapter will describe in details GW emission associated to this source, and will present a search for hyperbolic encounters in the data from the third LVK observing run.

3.3 Core collapse supernovae

Massive stars spend most of their lifetime burning hydrogen. Once hydrogen is exhausted, heavier elements are burnt in the core, and the stars alternate periods of nuclear burning, and contractions of the stellar core. If the star is enough massive, it becomes gravitationally unstable and the core collapse. A review on the different processes that lead to the implosion of the core can be found in Ref. [100].

Any asymmetric, accelerated mass motions in the supernovae core may generate GWs. Core collapse supernovae (CCSNe) are possible sources of multi-messenger observations with GWs: CCSNe have been observed in the electromagnetic spectrum, and low-energy neutrino were observed for SN1987A [101]. The observation of GWs can provide invaluable insight on the dynamics of these sources: GWs, as neutrinos, are produced at the central engine of the explosion, while electromagnetic emission originates from the expanding ejecta materials, thousands of kilometers away to the core.

The mechanism of CCSNe is complex and not completely understood, and so os their GW emission. There are several GW waveform models proposed for CCSNe. A common approach is multidimensional CCSNe simulations. In the case of non-rotating or slowly rotating progenitor stars, the main mechanism is neutrino-driven explosions in which the contribution of the neutrino heating has a significant role in creating the explosion. In rapid and differential rotation progenitor stars the magnetic field may play a dominant role in the explosion. The latter are referred to magneto-hydrodynamically driven explosions. There are also extreme emission models that are expected to induce large amplitude GWs. The frequency, duration and amplitude of the GW signals vary significantly among different simulations, and according to the characteristics of the progenitor star. As an example, Fig. 3.4 shows the GW emission in time and frequency domain for a 3D simulation for a progenitor star of $3.5M_{\odot}$. The modelling of CCSNe and the corresponding GW emission is an active field of research, more details can be found in Ref. [102].

For the purpose of this chapter, it is important to highlight that the emission of GWs from CCSNe is not completely understood, and the generation of the waveforms has a high computational cost. GWs waveforms are available only for certain initial conditions, and it is not possible to create template banks covering all the parameter space. Hence, waveform-independent approaches are necessary.

GWs from CCSNe are searched within all-sky generic searches, or targeting CCSNe sources observed in the electromagnetic spectrum [102, 103]. No GWs associated to CCSNe have been observed so far. The sensitivity of burst searches toward this source is evaluated injecting various CCSNe waveforms in the data and counting the simulation recovered with a certain FAR. Fig. 3.5 shows the detection efficiency versus the source distance achieved during the third observing run [103]. CCSNe are typically detectable with GWs only within a few kiloparsec. Extreme-emission models, that have stronger GW emissions but also lower expected rates, can be observed up to tens of kiloparsecs. The most promising opportunity for a multi-messenger observation of CCSNe in the electromagnetic spectrum, neutrinos, and GWs would be a CCSNe in our galaxy. Unfortunately, the rate is just one or two per century [102].

In addition, unmodelled algorithms performs triggered searches for GWs in the temporal and spatial location around CCSNe electromagnetic observations. Ref. [102] targets five CCSNe occurred during the first and second LVK observing runs within 20Mpc, and reports the minimum energy emitted in GWs needed to be detectable with 50% probability. The energy constraints are a few orders of magnitude larger than the energies predicted from multidimensional simulations, expected to be around $10^{-11}M_{\odot}c^2$ and $10^{-7}M_{\odot}c^2$.

3.4 Isolated neutron stars

Electromagnetic observations show that a fraction of the population of NS exhibits transient excitations. The two main types of excitations are pulsar glitches, and flaring activities from magnetars. Pulsar glitches are sudden increase in their rotational frequency. The main mechanisms to explain this phenomenon are star quakes and interactions between the stars' internal superfluid and their solid crust [105]. Pulsar glitches are expected to excite global oscillations of the neutron star that would lead to GWs on a timescale of up to $\sim$ 40s before the jump in frequency.

The GW emission is complex and depends on the glitch internal mechanism and on the equation of state of the NS. GWs associated to this source are searched with burst methods. The majority of the GW energy is expected to be due to the fundamental stellar oscillation mode, called f-modes, at a frequency around 2-3 kHz and with a morphology similar to an exponentially damped sinusoid. Assuming that the GW emission is completely described by the

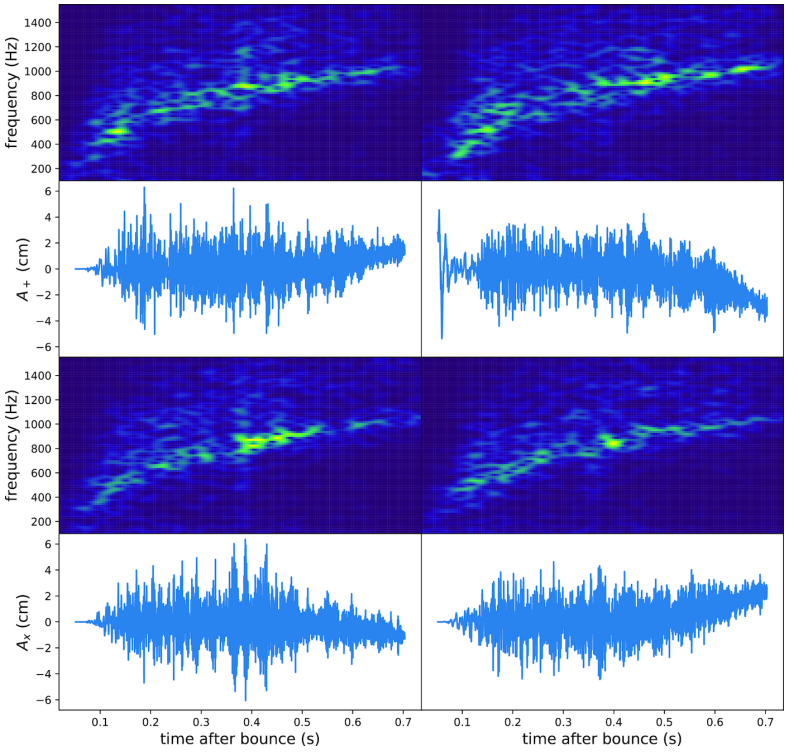

Figure 3.4: Example of the GW emission in time and frequency domain for a 3D simulation of CCSNe with an initial mass of 3.5 $M_\odot$. The two GW polarizations (A_+, $A_\times$) are computed for an observer at the pole (left), and for an observer at the equator (right). The GW signal is complex: in this case it peaks after $\sim$ 0.3s of the bounce, during the revival of the shock, at 800-1000 Hz [104].

f-mode oscillations and that the glitch energy is totally converted into GWs, it is possible to characterize the burst search sensitivity in terms of detectable glitch size $\Delta\nu_s$ [103]. Fig. 3.6 reports the detectable $\Delta\nu_s$ using O3 data, considering different NS masses, and two possible equation of states. The detectable glitch size is of the order of 10^{-4}Hz, while the actual glitch size measured from electromagnetic observation is between 10^{-8} and 10^{-4}Hz [103].

The second possible source of GWs associated with isolated NS are magnetars. Magnetars are highly magnetized NS that exhibit powerful X-ray and soft gamma-ray intermittent emissions [106]. The mechanism of these electromagnetic bursts involves excited cores and oscillations of the star crust, but it is not fully understood. Several models predict a GW counterpart to these events. The most promising GW signals are expected to be f-modes oscillations at high-frequency ($\sim$ 1-3kHz) and short-duration ($\sim$ 100ms), and quasi-periodic oscillations. These last are observed in the electromagnetic spectrum in the tail of giant flares, and are expected to be accompanied to long-duration GWs. Ref. [106] reports a triggered search for GWs associated with magnetars bursts, centred around the temporal and spatial location of the electromagnetic emission. During the third observing run, there were 13 magnetar bursts from two known magnetars and 3 from unknown source(s), but with characteristics typically of that of magnetars. No significant evidence of GWs associated with the magnetar bursts have been observed. The sensitivity of the analyses is assessed through a simulation campaign of generic waveforms, including

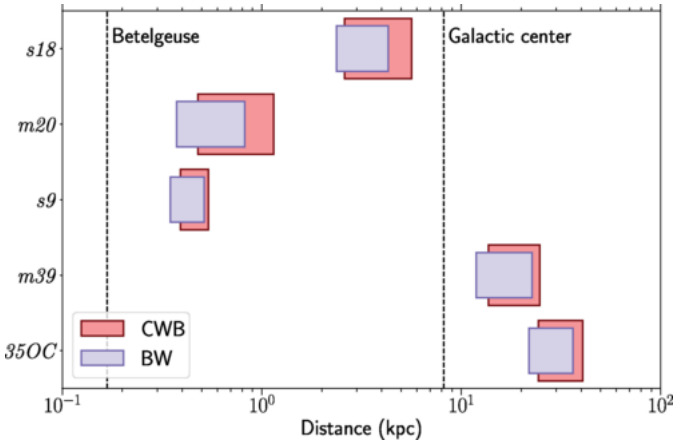

Figure 3.5: Distances at which 50% and 10% of CCSNe injections are recovered with all-sky burst searches on the data from the third observing run. Five different waveform models are considered [103]. The left side of the boxes indicates the 50% detection efficiency, while the right side the 10%. The different colors indicate two burst algorithms used, (CoherentWaveBurst in red and BayesWave in violet). These algorithms will be described in the next chapter.

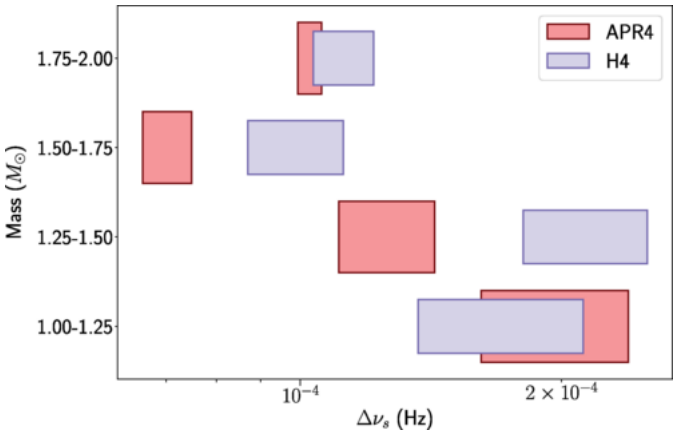

Figure 3.6: Detectable pulsar glitch size achieved in all-sky burst search in the data from the third observing run for different NS masses and two different equations of state (APR4 soft in red, H4 hard in violet). The boxes show the 50% detection efficiency, and their spread indicates the variation within the mass bin. The pulsar is assumed to have the same distance and spin of the Vela pulsar. Under these assumptions, the glitch size would need to be larger than $\sim 10^{-4}$ for 50% of the sources to be detected [103].

plausible GW waveforms from f-modes.

The author of this thesis contributed personally, both by performing the burst searches and as a member of the paper writing team, to the LVK collaboration search for GWs associated with magnetar bursts reported in Ref. [106].

3.5 Cosmic Strings

Cosmic strings are topological defects, i.e. stable configurations of matters formed after spontaneous phase transition in the early Universe [107]. Cosmic strings are extremely interesting as they could probe particle physics beyond the standard model, at an energy scale much larger than the one reached by current accelerators. In simple words, the formation of topological defects is the following: causal effects now and in the early Universe propagate at the speed of light c. At a time t, regions of the Universe distant to each other more than a distance $d = ct$ cannot know anything about each other. When a phase transition occurs, different regions of the Universe might fall into different minima, among a set of possible states. The boundaries between these regions with different minima are called topological defects. If there are only two possible minima, the interpolating regions between the different minima are called domain walls. Cosmic strings are predicted in more complicated theories, in which the minimum energy states possess 'holes', and the windings around such holes are the cosmic strings.

These phase transitions may have occurred at the grand unifications, corresponding to an energy scale of about 10^{16}GeV. Once formed, in an expanding Universe, the strings would be stretched, and then they would form a cascade of smaller loops. These could eventually decay through the emission of GWs. There are different models for the loop distribution, accounting for different production mechanisms of the cascade of loops.

Cosmic string loops oscillate periodically in time. The power of the GW emission is proportional $\Gamma_d G\mu^2$ where $\Gamma_d \sim 50$ is a numerical factor, and $G\mu$ is the string tension, a dimensionless quantity that depends on the string formation energy.

Cosmic strings are expected to emit short-duration GW bursts by means of string cusps and kinks. The first are points of the strings, and produce beamed GWs in the direction of the cusp. Kinks result from the collision of two cosmic strings, and propagate around the string. The collisions of kinks, called kink-kink, are expected to generate GWs that radiate isotropically. An example of a GW waveform generated by a cosmic string cusp is shown in Fig. 3.7.

Unmodelled and template-based searches are used to detect individual cosmic string emissions. In addition, the incoherent superposition of weak cosmic strings is expected to create a stochastic GW background (see Section 1.3).

Ref. [107] presents a search for individual GWs associated with cosmic strings, and the stochastic background. Individual cosmic strings are searched using a match-filtering search (see Section 2.2.2), separately for cusps, kinks and kink-kink collision waveforms. Different models yield different loops, so they also include a waveform model that interpolates the others, widening the parameter space. No candidate events have been reported. The loudest events are investigated with attention, but they all originated from a well-known family of glitches, called blip (see Section 6.1), whose waveform is similar to cosmic strings.

Burst searches also look for GWs from cosmic strings. The search sensitivity for this source is presented in Section 4.1.6. It is not immediate to compare the sensitivity achieved by the burst search and the match-filtering search proposed in Ref.[107] because the two methods employ different statistics and different injection sets [108]. As the GW waveform is simple and consists of a signal with a single cycle, template-based searches are not significantly more sensitive than burst searches as in the case of CBC. Injection studies enable to estimate the loop dimension that would have produced a significant emission, and compute the upper limit on the event rate [107].

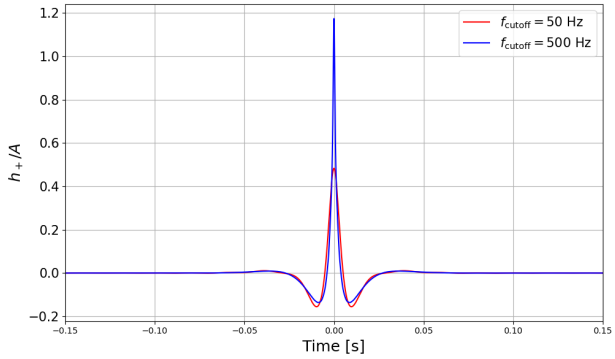

Figure 3.7: GW waveform expected by a cosmic strings cusp in time domain. The signal is linearly polarized ($h_\times = 0$). The high-frequency cutoff is a free parameter, linked to the fact that the GW emission is beamed: the higher the cutoff, the smaller the emission opening angle [108].

3.6 Dark Matter

Dark matter represents one of the greatest open question in cosmology: this hypothetical form of matter is expected to constitute about 80% of the Universe's gravitating matter [109]. Its existence is necessary to explain gravitational effects as the motion of galaxies and cosmic microwave background anisotropies. However, its nature and distribution are largely unknown.

GW observations are a promising channel to investigate dark matter. Several dark matter candidates might be explored with current and future GW detectors. A review on how exploiting GWs to probe dark matter can be found in Ref. [110]. Next, the main dark matter signatures that can be investigated with unmodelled searches for GW transients are briefly presented.

Among the possible components of dark matter, there are primordial black holes, hypothetical BHs formed soon after the Big Bang, before the formation of stars. There are several formation scenarios for such objects [110]. The merger of primordial BHs can potentially produce signals within the band of current GWs detectors [84]. In particular, the detection of GWs from the coalescence of sub-solar mass BHs would generate GWs with a signature incompatible with BH of astrophysical origins. Indeed, according to the theory of stellar evolution, BHs cannot have a mass below $1.4 M_\odot$. Primordial BHs might also experience close hyperbolic encounters that are expected to generate GWs bursts signal [111], as discussed in Chapter 7.

In addition, ground-based and future GW detectors may probe the environment surrounding compact objects. Large densities of dark matter may form around BHs. These environmental effects may induce modifications to the GW waveforms [112]. Unmodelled searches can be used to detect the discrepancies between standard and 'dressed' BHs. Dark matter may also form clouds of ultralight bosonic particles, referred to as bosonic clouds, that can emit GWs. The oscillations of these clouds might emit monochromatic GWs [26], while the collapse of the bosonic cloud may generate GW bursts [110].

Moreover, dark matter may collapse into exotic compact objects that could eventually form binary systems. The mergers of these systems may be observed with GWs, and are expected to have several differences w.r.t. the mergers of standard BHs, that can be identified with unmodelled searches see also Section 3.1.

Chapter 4

CoherentWaveBurst: a pipeline for unmodeled gravitational-wave data analysis

There exists two main approaches to detect GW signals embedded in the detector noise: template-based and burst searches. The firsts look for GW signals close to the waveform models contained in extensive template banks (see Section 2.2.2). Instead, burst searches do not assume a waveform model but basically look for excess of power that is coherent on multiple GW detectors. For this reason, they are often referred to as unmodelled algorithms.

There are multiple burst software running in low-latency during the LVK observing runs, and extensive searches for GW transients are performed offline as well. Burst searches are crucial to identify GW transients from the astrophysical sources described in Chapter 3. In addition, burst algorithms allow reconstructing the GW events with minimal assumptions and are able to identify discrepancies between theoretical models and measured data, which may reveal new physics. Moreover, burst searches provide crucial information on the detector noise that can be useful for diagnostic purposes during the observing runs to identify short-duration disturbances.

This chapter explains how unmodelled algorithms for GWs searches work. The methodological developments and analyses proposed in the next chapters of this thesis are based on the software Coherent WaveBurst (cWB) [12, 113], which is described in great detail in Section 4.1. Alternatives approaches are presented in Section 4.2.

4.1 Coherent WaveBurst

cWB analyses GW detectors strains and identifies excess of power that are coherent in the network of detectors [12, 113]. cWB input consists of the detectors' calibrated output (Section 4.1.1). Each detector time-series is transformed into the time-frequency (TF) domain through wavelet transform (Section 4.1.2). TF maps from each detector are whitened, and the regions with energy above the baseline detector noise are identified, and clustered together (Section 4.1.3). The single-detectors clusters are combined coherently with the corresponding ones in the other detectors, and a maximum likelihood statistic is used to extract the signal waveform and the sky localization. The coherent analysis represents the core of the burst analysis and so it is described in details in Section 4.1.4. To illustrate the different analysis stages, an example of a GW simulation from a BBH merger is shown along each section. Once cWB has identified

a list of triggers, i.e. excess of power coherent in the detectors, it assigns a significance to discriminate significant outliers from false alarms (Section 4.1.5). A further post-processing step is implemented using a machine-learning technique to increase the search sensitivity (Section 4.1.6).

cWB was the first algorithm to detect the first GW event GW150914 [11]. Since then, the algorithm had undergone several methodological improvements, and it has been employed for several studies. For reference, the main analyses performed with cWB are the following:

- all-sky short-duration searches: they target GW transients with duration < 1s on the data of each LVK collaboration observing runs [103, 114, 115].
- all-sky long-duration searches: they target GW transients with duration up to $\sim$ 100s which might originate from BNS mergers, and oscillations of isolated neutron stars.
- waveform consistency tests between the CBC waveform models and the waveforms reconstructed with minimal assumptions [1, 116].
- follow-up investigations on specific GW events. Among others, cWB has performed extensive studies on the first GW observation (GW150914) [117], and on GW190521, the first direct observation of a BH in the intermediate mass range between stellar mass and supermassive black holes, with the identification of higher order modes [118, 119].
- search for eccentric CBC [120].
- search for post-merger signals in known BNS [121] and BBH mergers [95].
- targeted search for GW transients from CCSNe [102]
- search for hyperbolic encounters of compact objects (see Chapter 7)

Next, the workflow of cWB is presented.

4.1.1 Input data

cWB analyses the calibrated detectors output $s(t)$ from each GW detector. The detectors outputs are a superposition of Gaussian noise, glitches and long-duration noise such as persistent narrowband lines, and potential astrophysical signals. Each time-series is sampled at 2048Hz. To better explain the various steps of the cWB analysis, a GW waveform model is injected into Gaussian noise. The injected signal corresponds to a CBC between two non-spinning BHs of masses $m_1 = 20M_\odot$, $m_2 = 40M_\odot$, merging at a distance of 400Mpc, modeled with the waveform approximant IMRPhenomPv3 [122]. Fig. 4.1 shows the corresponding GW waveform model and its superposition with real detector data. The figures of this simulation across the different analysis stages have been obtained with pycWB [123], a user-friendly and modular python version of cWB that has been recently proposed.

4.1.2 Time-frequency representation

The first step of the cWB analysis is to transform the time-series input into the time-frequency (TF) domain. In this representation, the space is covered by tiles, called pixels, and each pixel has an associated energy. A GW can be identified in the TF plane as an excess of power w.r.t. the detector stationary noise. There exists various methods to obtain a TF representation of a signal. In our case, the fundamental requirements for the TF transformation are to be fast and able to analyse in low-latency GW data, and to be able to localize short-lived transient signals

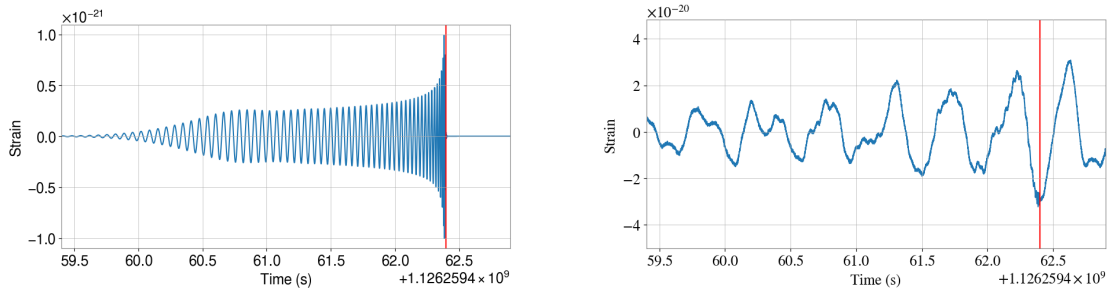

Figure 4.1: (*left*) Simulation of a GW from the CBC between two BHs of masses $m_1 = 20M_\odot$, $m_2 = 40M_\odot$, merging at a distance of 400Mpc. (*right*) The same GW simulation injected into real detector noise. The red line shows the merger time. Note the different scales of the strain amplitude on the y axis: the amplitude of the GW signal is lower than the typical fluctuations of the GW detector gaussian noise.

having a reduced spectral leakage. In addition, it is crucial that the energy content of the signal is conserved during the transformation, and that the inverse transform is well-defined in order to reconstruct back the GW waveform in the time domain.

In cWB the TF representation is computed with wavelet transformation, a powerful tool widely used in signal processing. The idea is to approximate an input signal, either a time-series or an image, with a class of simple wavelet waveforms. Wavelet transform is used in huge variety of tasks as for example denoising and compression, when most of the energy contained in few wavelet coefficients.

In cWB the input time-series $s(t)$ is transformed in the TF domain according to:

$$\omega_{nm} = \sum_t f_{nm}(t)s(t) \tag{4.1}$$

where $n, m \in \mathbb{N}$ indicate the discrete coefficients, and f_{nm} is the wavelet Wilson-Daubechies-Meyer filter, described in Ref. [124]. This transform projects the signal into an orthonormal basis: this enables a high computational efficiency, and an easy way to reconstructed back the signal to time domain. The product of the wavelet transform can be visualized as a time-frequency maps where each pixel has dimension Δf and Δt and the colourscale indicates the amplitudes (ω_{nm}) or the energy (ω_{nm}^2).

As discussed in the previous chapter, unmodelled searches look for GW transients that can have different durations and frequency evolutions. To be able to identify and reconstruct accurately a wide range of morphologies, cWB computes multi-resolution wavelet transforms: the input signal is decomposed into different sub-signals with different resolution levels, i.e. with different Δf and Δt. Fig. 4.2 illustrates the TF maps with different resolutions for the simulated CBC signal shown in Fig. 4.1 in the data of LIGO Livingston. The first plot on top has the best resolution in frequency (Δf=1Hz) and the worst time localization (Δt=0.5s). From top to bottom the resolution in frequency decreases and the time localization improves up to Δt=0.008s and Δf=64Hz. cWB produces a TF map for each GW detector, and for each TF resolution.

4.1.3 Data conditioning and clustering

The TF maps are conditioned, i.e. noisy lines are removed using a linear prediction filter [125]. Next, the pixels are whitened: the TF maps are normalized by the root-mean-square noise energy,

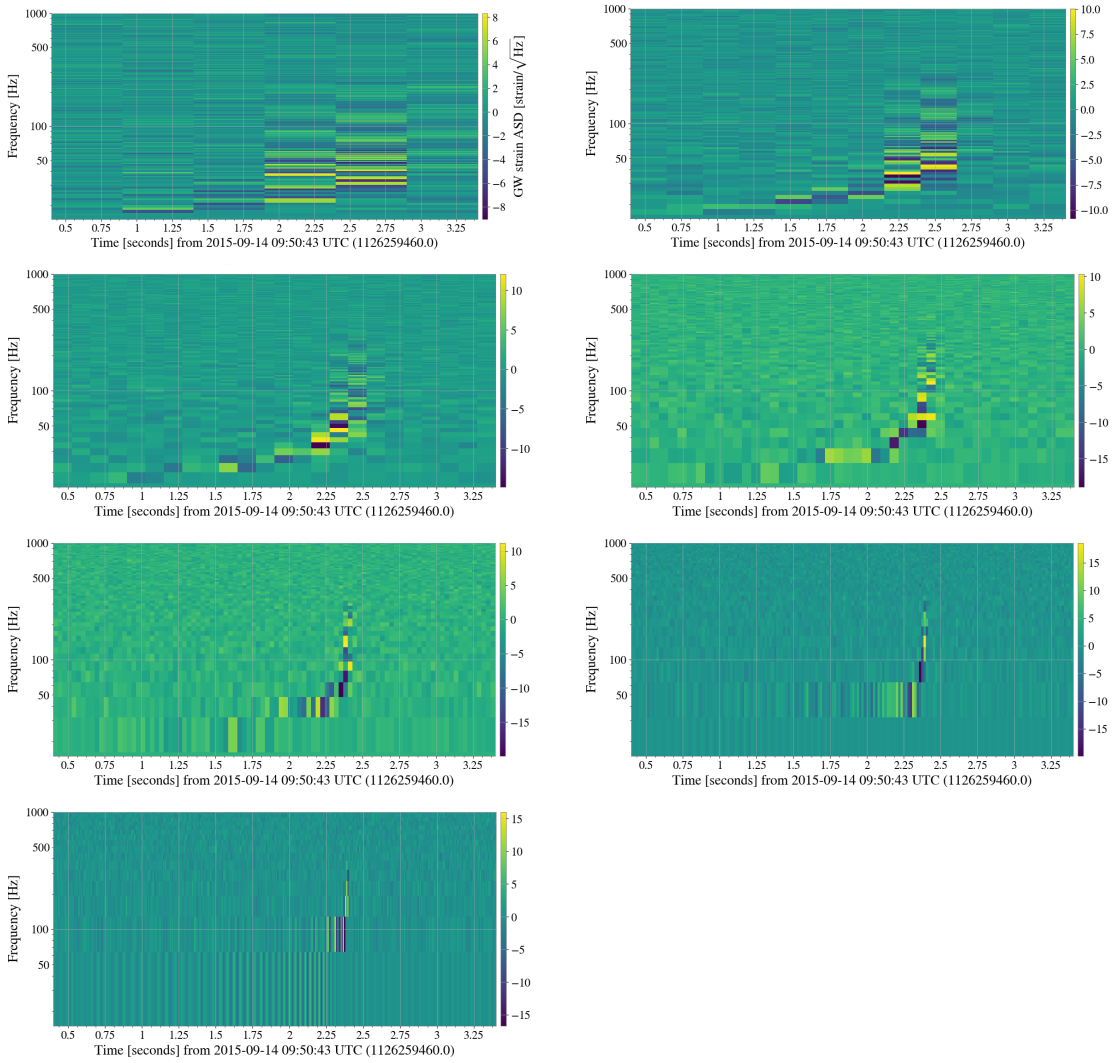

Figure 4.2: Wavelet TF maps with different resolutions for a simulated GW signal of a CBC in the data of LIGO Livingston. The injected signal in time domain is shown in Fig. 4.1. In the TF representation the chirp-like structure expected from BBHmergers is clearly visible. From top to bottom the resolutions in time are increasing: 1) Δt=0.5s Δf=1Hz, 2) Δt=0.25s Δf=2Hz, 3) Δt=0.125s Δf=4Hz, 4) Δt=0.062s Δf=8Hz, 5) Δt=0.031s Δf=16Hz, 6) Δt=0.016s Δf=32Hz, 7) Δt=0.008s Δf=64Hz

which is calculated at the finest frequency resolution. The root-mean-square energy is estimated on a certain data segment, which then is shifted. Both the window and the shift can be tuned by the user.

After the whitening, most of the pixels have an energy close to zero. A small fraction of the most energetic pixels, called 'black' pixels, are saved. The fraction of the black pixels saved is set by a tunable parameter and typically is a few percent. Neighbours pixels, located nearby the black pixels both in time and/or frequency, are also selected. cWB defines clusters of TF tiles as a connected group of black pixels and their neighbours. The user can choose to select neighbours pixels according to a certain pattern: for example, if the search is targeted to CBC signals which have a chirp-like signature in TF maps, neighbours pixels can be selected following a diagonal pattern.

Then, TF clusters from different resolutions are combined to form a single trigger. The gap in units of pixels between clusters according to which two nearby pixels are considered as a single trigger can be tuned according to the targeted signals: when searching for long GW signals wider gaps are admitted. At the end of the clustering stage, if an astrophysical signal or a transient noise is present in the data, cWB outputs a multi-resolution cluster for each detector.

4.1.4 Coherent statistic

GW data contains short-duration disturbances due to environmental or instrumental noise that can mimic GW signals, see Section 2.1.5. To mitigate the impact of glitches, data from multiple GW detectors are used: a transient signal is considered astrophysical when it is observed in two or more GW detectors located in different areas. Instead, a signal that occurs only in a single detector is likely a local disturbance[1]. There are two methods to use the information of a network of GW detectors: coincident and coherent analysis [127]. The former identifies a list of excess of power, or triggers, in each detector independently. Then the triggers from different detectors are correlated in time, to identify time-coincident signals. Instead, the coherent analysis first merges the data from the network of interferometers, and then looks for a common pattern in their responses. The signals find by the coherent analysis are not only temporal-coincident, but share also the morphology, the energy content and the source localization. Coherent methods use more complete information, resulting in a more efficient rejection of transient noise. However, they have a higher computational cost.

cWB, as suggested by the name, uses a coherent statistic. After the clustering stage, the data from K detectors are a discrete series $x_k[i]$ where i is the pixel index of the cluster. When a GW event occurs, the detector output contains the superposition of the detector response to the astrophysical signal $h[i]$(Eq. 2.5), and the detector noise $n[i]$:

$$x[i] = h[i] + n[i] \tag{4.2}$$

The aim of the analysis is to find the amplitudes of the GW polarizations (h_+ and $h_\times$) and the source localization (ϕ, θ) from the signal coherent on the GW detectors.

To start, the likelihood ratio Λ is defined as the ratio of the joint probability that the data contains a GW signal and the joint probability that there is only noise:

$$\Lambda(x) = \frac{p(x|h)}{p(x|0)} \tag{4.3}$$

[1]This approach assumes that the detectors noise are uncorrelated. The only known source of noise that can potentially produce correlated noise over global distances is magnetic fields from Schumann resonances. These resonances are excited by electric current in lightning, bouncing between the ionosphere and the Earth. This source of noise may limit especially the sensitivity to stochastic background searches at low frequencies with future detectors [126]. Hence, in the realm of searches for GW transients, the noise of the detectors can be considered uncorrelated.

For simplicity, the pixel index i will be neglected in the following equations. Considering the noise stationary and Gaussian with zero mean and standard deviation σ, not correlated among different detectors, the joints probabilities can be written as:

$$p(x|h) = \prod_k \frac{1}{\sqrt{2\pi\sigma}} \exp\left(-\frac{(x_k - h)^2}{2\sigma^2}\right) \tag{4.4}$$

$$p(x|0) = \prod_k \frac{1}{\sqrt{2\pi\sigma}} \exp\left(-\frac{x_k^2}{2\sigma^2}\right) \tag{4.5}$$

Substituting Eq. 4.4 and Eq. 4.5 in Eq. 4.3, the twice of the logarithm of the likelihood ratio becomes:

$$\mathcal{L} = 2\ln(\Lambda(x)) = \sum_k \frac{1}{\sigma^2}\left(2x_k h - h^2\right) \tag{4.6}$$

The previous equation can be written using the noise-scaled data vector $\mathbf{w}$:

$$\mathbf{w}[i] = \frac{x_1[i]}{S_{n,1}[i]}, ..., \frac{x_k[i]}{S_{n,k}[i]} \tag{4.7}$$

where S_n is the detector PSD defined in Section. 2.1.4. We also define the noise-scaled network response vector $\mathbf{g}$ that depends on sky position θ, ϕ according to the detector antenna patterns $F_+, F_\times$ defined in Eq. 2.5:

$$\mathbf{g}[i] = \begin{bmatrix} \frac{F_{1+}h_+[i]}{S_{n,1}} & \frac{F_{1\times}h_\times[i]}{S_{n,1}} \\ ... & ... \\ \frac{F_{k+}h_+[i]}{S_{n,k}} & \frac{F_{k\times}h_\times[i]}{S_{n,k}} \end{bmatrix} \tag{4.8}$$

$\mathcal{L}$ can be rewritten in a more compact form as:

$$\boxed{\mathcal{L} = 2(\mathbf{w}|\mathbf{g}) - (\mathbf{g}|\mathbf{g})} \tag{4.9}$$

The inner product is calculated over the TF pixels of the cluster. The solutions for the GW waveforms are found maximizing $\mathcal{L}$ varying $\mathbf{g}$, as showed below.

It is important to note that, when maximizing the likelihood, aligned detectors, i.e. detectors with the same antenna pattern, provide significantly different results than misaligned detectors [128]. The alignment depends both on the strain sensitivities and the angular orientation of the detectors. Next, the maximization of the likelihood ratio in the two configurations is shown: the aligned case is indicated with the letter A, while the misaligned case with M. For simplicity, two detectors are considered. In the first case, considering x_1 and x_2 the detector outputs with the same noise, Eq. 4.9 becomes:

$$\mathcal{L}_A = 2(x_1|g) + 2(x_2|g) - (g|g) \tag{4.10}$$

where g is the detector response to GW signal expressed as a scalar wave as it is the same for the two detectors. Varying $\mathcal{L}_A$ w.r.t. g gives:

$$g = x_1 + x_2 \tag{4.11}$$

and by substituting the solution into $\mathcal{L}_A$:

$$\mathcal{L}_{A,max} = x_1^2 + x_2^2 + 2x_1x_2 \tag{4.12}$$

Instead, in the misaligned case, the likelihood is:

$$\mathcal{L}_M = 2(x_1|g_1) + 2(x_2|g_2) - (g_1|g_1) - (g_2|g_2) \tag{4.13}$$

Varying $\mathcal{L}_M$ over the detector responses g_1 and g_2 gives respectively $g_1 = x_1$ and $g_2 = x_2$ and by substituting the solutions in the likelihood:

$$\mathcal{L}_{M,max} = x_1^2 + x_2^2 \tag{4.14}$$

Comparing Eq. 4.12 and Eq. 4.14 it appears that the likelihood statistic in the aligned case contains both the power and the cross-correlations terms, while the misaligned case, no matter how small the misalignment is, it contains only the power terms. The functional $\mathcal{L}_M$ is not approaching $\mathcal{L}_A$ in the limit of perfect alignment: this indicates that the maximum likelihood ratio statistics may not be the optimal statistic for a general network of GW detectors. This behaviour is typically referred to as *the two detectors paradox*.

This paradox has important consequences on defining an appropriate statistics for cWB analysis. To deal with the two detector paradox, a new coordinate frame is introduced [128]. To simplify the notation, we define the complex waveforms $u[i], \tilde{u}[i]$:

$$\begin{aligned} u[i] &= h_+[i] + ih_\times[i] \\ \tilde{u}[i] &= h_+[i] - ih_\times[i] \end{aligned} \tag{4.15}$$

and the complex antenna patterns $A, \tilde{A}$ normalized by the detector sensitivity σ_k :

$$\begin{aligned} A_k &= \frac{1}{2}(f_{+k} + if_{\times k}) \\ \tilde{A}_k &= \frac{1}{2}(f_{+k} - if_{\times k}) \end{aligned} \tag{4.16}$$

where the index k indicates the GW detectors and $f_+, f_\times$ are antenna patterns normalized by σ_k ($f_+ = F_{+k}/\sigma_k$ and $f_\times = F_{\times k}/\sigma_k$). In the following, for simplicity, we refer to multiple detectors using the vector notation such as $\mathbf{A} = (A_1, ..A_N)$. A coordinate transformation in the wave coordinate frame is performed by a rotation such as:

$$\begin{aligned} \mathbf{u'} &= \mathrm{e}^{i\gamma}\mathbf{u} \\ \mathbf{A'} &= \mathrm{e}^{i\gamma}\mathbf{A} \end{aligned} \tag{4.17}$$

The detector response $\mathbf{g}$ in this complex notation is:

$$\mathbf{g} = \tilde{\mathbf{A}}\mathbf{u} + \mathbf{A}\tilde{\mathbf{u}} \tag{4.18}$$

It is useful to define the network antenna patterns:

$$\begin{aligned} g_r &= \sum_{k=1}^{N} \frac{A_k \cdot \tilde{A}_k}{\sigma_k^2} \\ g_c &= \sum_{k=1}^{N} \frac{A_k^2}{\sigma_k^2} \end{aligned} \tag{4.19}$$

A transformation $g_c \to g_c'$ that is particularly convenient is the one which makes the imaginary part of g_c' null. We call this frame the *dominant polarization frame* (DPF). From Eq. 4.17, $g_c = |g_c|e^{2i\gamma}$, so that the transformation of the antenna patterns is:

$$\begin{aligned} \mathbf{f}_+' &= \mathbf{f}_+ \cos(\gamma) + \mathbf{f}_\times \sin(\gamma) \\ \mathbf{f}_\times' &= -\mathbf{f}_+ \sin(\gamma) + \mathbf{f}_\times \cos(\gamma) \end{aligned} \tag{4.20}$$

Some useful properties of the DPF are:

- having the imaginary part of g'_c null, is equivalent of having $\mathbf{f}'_+$ orthogonal to $\mathbf{f}'_\times$. Indeed:

$$\mathbf{A}'^2 = (\mathbf{f}'_+ + i\mathbf{f}'_\times)\cdot(\mathbf{f}'_+ + i\mathbf{f}'_\times) = \mathbf{f}'^2_+ + \mathbf{f}'^2_\times + 2i(\mathbf{f}'_+ \cdot \mathbf{f}'_\times) \tag{4.21}$$

  This property simplifies the evaluation of the likelihood.

- The transformation from the generic wave frame $(\mathbf{f}_+, \mathbf{f}_\times)$ to the DPF follows from the equation above. Indeed:

$$\mathbf{f}^2_+ - \mathbf{f}^2_\times + 2i(\mathbf{f}_+ \cdot \mathbf{f}_\times) = \mathbf{A}^2 = (\mathbf{A}'e^{i\gamma})^2 = |\mathbf{A}'^2|e^{2i\gamma} = |\mathbf{A}'^2|(\cos(2\gamma) + i\sin(2\gamma)) \tag{4.22}$$

  and so:

$$\begin{aligned} \cos(2\gamma)|\mathbf{A}^2| &= (\mathbf{f}^2_+ - \mathbf{f}^2_\times) \\ \sin(2\gamma)|\mathbf{A}^2| &= 2(\mathbf{f}_+ \cdot \mathbf{f}_\times) \end{aligned} \tag{4.23}$$

- the DPF takes its name from the following property:

$$|\mathbf{f}'_+| \geq |\mathbf{f}'_\times| \tag{4.24}$$

  The relationship above is derived looking at the antenna patterns defined in the generic frame $(\mathbf{f}_+, \mathbf{f}_\times)$ and the ones in the DPF $(\mathbf{f}'_+, \mathbf{f}'_\times)$, indeed:

$$|\mathbf{f}'_+|^2 = |\mathbf{f}_+\cos(\gamma) + \mathbf{f}_\times \sin(\gamma)|^2 = \frac{1}{2}(g_r + |g_c|) \tag{4.25}$$

  and

$$|\mathbf{f}'_\times|^2 = \frac{1}{2}(g_r - |g_c|) \tag{4.26}$$

  From the above equations, we can define the alignment factor α:

$$\alpha = \frac{|\mathbf{f}'_\times|^2}{|\mathbf{f}'_+|^2}, \qquad 0 \leq \alpha \leq 1 \tag{4.27}$$

  for aligned detectors $\alpha = 0$. Fig. 4.3, taken from Ref. [128], shows the alignment factor as a function of the sky coordinates for different detectors networks: for the two LIGO detectors, that are almost coaligned, $\alpha \sim 0$ almost for all sky positions. Adding more detectors, α increases for a larger sky area. However, even for a network of 4 detectors (including LIGO, GEO 600 and Virgo detectors) α is small for a considerable fraction of the sky. This has important consequences when computing the SNR given by a GW.

- In the DPF, the SNR is:

$$\text{SNR} = \sum_{k=1}^{N} \frac{g_k^2}{\sigma_k^2} \approx 2(g_r + |g_c|)(\langle h'_+\rangle^2 + \alpha\langle h'_\times\rangle^2) \tag{4.28}$$

  where h'_+ and $h'_\times$ are the GW polarization states in the DPF (to distinguish from h_+ and $h_\times$ that are the GW polarizations in the wave frame), and $\langle h'_+\rangle^2$ and $\langle h'_\times\rangle^2$ are the sums square energies carried by each component. The brackets indicate the sum over the samples of the time-series. The contribution of the second GW polarization $h'_\times$ is diminished by the network alignment factor α. For a network of coaligned detectors, the component $h'_\times$ of the GW signal cannot be detected and all the SNR comes from the dominant polarization. So the $h'_\times$ component adds little to the total SNR of the GW signals. Instead, the detector noise introduces the same contribution for each signal component. When the alignment factor is small, the second component of the wave adds more noise than signal.

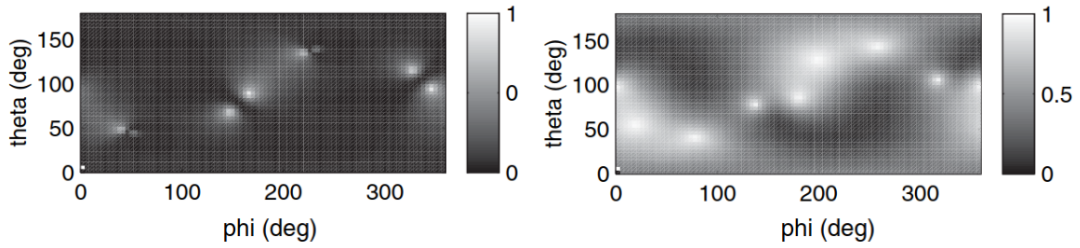

Figure 4.3: Alignment factor α (Eq. 4.27 for the network composed of the LIGO detectors (*left*) and for the four detectors network (LIGO, GEO600 and Virgo) (*right*) from Ref. [113].

To overcome this paradox, cWB introduces a constraint to the likelihood. The aim is to reduce the noise contribution, losing a negligible fraction of astrophysical events. This solution is effective when dealing with aligned detectors, as the LIGO detectors, while it is not optimal when including other detectors, as Virgo and KAGRA, whose orientation is different. The likelihood constraints and the search sensitivity of cWB with three detectors network HLV will be discussed in the next chapter.

To conclude this section on the coherent statistics, two fundamental quantities in cWB analysis are introduced. In the DPF, the GW response vector lives in the plane defined by $\mathbf{f}'_+$, $\mathbf{f}'_\times$. Varying the likelihood, we obtain a system of linear equations whose solutions are the GW components. The maximum of Eq. 4.9 is:

$$\mathcal{L}_{\mathrm{DPF},max} = \mathbf{w}[i]P[i]\mathbf{w}^T[i] \tag{4.29}$$

where the matrix P is the projection constructed from the units vectors e_+ and $e_\times$:

$$P_{nm} = e_{n+}[i]e_{m+}[i] + e_{n\times}[i]e_{m\times}[i] \tag{4.30}$$

where m and n are the detector indexes. The likelihood in Eq. 4.29 is a quadratic form that can be split in two components. The diagonal terms of the likelihood matrix are relative to a single detector, and describe the reconstructed normalized incoherent energy, or null energy E_n:

$$E_n = \sum_{i\in C}\sum_{n} w_n[i]P_{nn}[i]w_n[i] \tag{4.31}$$

Instead, the off-diagonal terms indicate the coherent energy E_c on the detector network:

$$E_c = \sum_{i\in C}\sum_{n\neq m} w_n[i]P_{nm}[i]w_m[i] \tag{4.32}$$

Fig. 4.4 shows the time-frequency representation of the coherent and the incoherent energy for the GW simulation presented in Fig. 4.1. The large majority of the energy of the signal is coherent in the detector network, with the characteristic chirp signature.

The combination of the coherent and uncoherent energy is used to define the correlation coefficient *cc*:

$$cc = \frac{E_c}{E_c + E_n} \tag{4.33}$$

the larger *cc* the higher the energy that is coherent in the network, indicating a possible astrophysical signal. Small values of *cc*, typically < 0.7 indicate instead single-detector glitches.

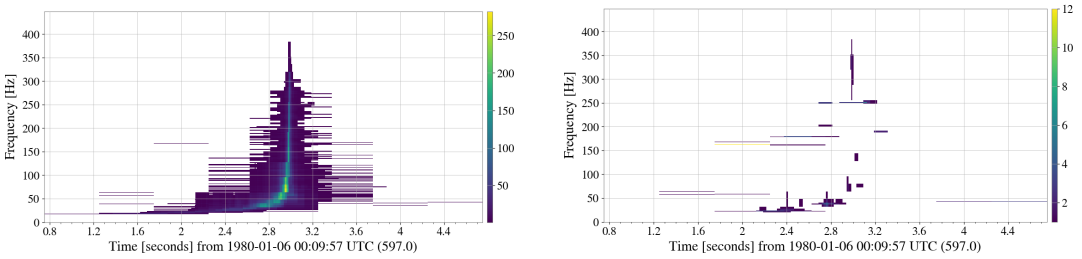

Figure 4.4: Time-frequency maps of the coherent energy, or likelihood (*left*) and the incoherent energy, or null (*right*). The simulated signal is the CBC of two black holes with masses $m_1 = 20M_\odot$ and $m_2 = 40M_\odot$, as in Fig. 4.1. The majority of the energy of the signal is coherent in the detectors network.

4.1.5 Significance estimate

Once cWB analyses a period of data, it provides as output a list of triggers, i.e. a cluster of pixels indicating an excess of power coherent on the detector network. Each trigger is characterized by its coherent energy E_c, incoherent energy E_n and several properties as the network SNR, central frequency, duration, ecc.

cWB associates to each trigger a ranking statistic ρ_0 that is roughly proportional to E_c/E_n. The precise definition of the ranking statistics is an active field of research, because it is strongly related to the algorithm search sensitivity. For the all-sky short-duration search on the data from the third observing run, the cWB ranking statistic was:

$$\rho_0 = \sqrt{\frac{E_c}{1 - X^2(\max(1, X) - 1)}} \tag{4.34}$$

where E_c is the coherent energy and $X = E_n/n$ with E_n noise energy and n the number of wavelets used. Larger values of ρ_0 suggest that the signal as an astrophysical origin, while small values are expected for glitches.

Next, cWB assigns a significance in terms of FAR to each trigger: cWB computes a background distribution using time-shifted data, as mentioned in Section 2.2.2. The data of one detector are time-shifted w.r.t. the other detector(s) data. The triggers coincident in this data by construction cannot be astrophysical GW signals, but they are due to interferometers' Gaussian noise and glitches. Such time slides are performed several times in order to accumulate sufficient statistics for the background. The FAR of an event with ranking statistic ρ_i is defined as:

$$\mathrm{FAR} = \frac{N_{\rho > \rho_i}}{T} \tag{4.35}$$

where $N_{\rho>\rho_i}$ is the number of triggers in the background distribution with $\rho > \rho_i$ and T the background time. Often the inverse FAR, denoted as IFAR, is used for convenience.

Once the background has been computed, a set of simulated signals is injected into the same data segment used for the background analysis. The detection efficiency of the simulations, defined in the next section, is referred to as *closed box* analysis. If the latter does not highlight issues in the analysis, the pipeline configuration is frozen and the actual data, referred to as *zero-lag* data, are analysed to see if there is a significant GW candidate.

A trigger in the zero-lag is considered a potential GW signal if it has an IFAR over a certain threshold, which depends on the search. During the third observing run, the threshold for

considering a trigger a candidate GW event is IFAR over one per 10 months for CBC template-based searches, and IFAR over one per 4 years for burst searches.

4.1.6 Increasing the search sensitivity with a decision-tree classifier

The previous section presented the background distribution and how it is used to assess the significance of a cWB trigger. Clearly, to increase the search sensitivity it is crucial to reduce the ranking statistics of the background triggers. Until the third observing run [103], the standard approach employed by cWB was to split the triggers in three different bins according to the parameters Q_a, Q_p. Q_a, Q_p are computed for each trigger from the waveform reconstructed by cWB in each detector. The first is basically the ratio between the peak amplitude of the cWB reconstructed waveform and the relative amplitude maximum before and after the peak. Q_p is defined modelling the reconstructed waveform with a CosGaussian function, where Q_p is the estimated Q factor. The precise definitions of Qa and Q_p are reported in Ref. [129]. Small values of Q_a and Q_p indicate triggers with a morphology similar to blip glitches, which populate the cWB background distribution. Two bins were created to collected triggers with low Q_a, Q_p ($Q_a = 0$ and $Q_p < 3$) and were referred as 'dirty' bins. The third bin collected the remaining cWB triggers, with morphologies different from blip glitches, and it was referred to as 'clean' bin. The significance was computed in each bin separately, so that the 'clean' bin had a much lower false alarm rate. The binning method is effective in increasing the sensitivity to GW events, as long as they have high values of Q_a and Q_p. However, the same data is analysed three times, and it is mandatory to include a trial factor equal to three that divides the IFAR computed for each trigger. This means that the more bins the less significant will be the candidate events. More details in the binning procedure in cWB can be found in Ref. [103].

Recently, the binning procedure has been substituted with a decision-tree classifier, called eXtreme Gradient Boosting or XGBoost [130]. XGBoost is a well-known ML algorithm used for classification task in several fields. XGBoost takes in input tabular values from two (or more) labelled classes and, during the training procedure, it learns how to discriminate the two classes. Once trained, given a set of tabular values the model returns as output a value $W_{\rm XGB}$ in the range [0,1] being 0 the label of the first class and 1 for the other. In our case, the two classes correspond to an astrophysical signal (label 1) and a noise signal (label 0). The XGBoost output, $W_{\rm XGB}$, is used to re-rank cWB triggers as [131]:

$$\rho \propto \rho_0 \times W_{\rm XGB} \tag{4.36}$$

where ρ_0 is defined in Eq. 4.34. In the training dataset, the noise class is represented with the background triggers, instead the signal class can be populated according to the GW source targeted. The tabular values used to train the model are a subset of cWB summary statistics. The choice of the input parameters depends on the search: when targeting a specific astrophysical population as BBH, the classification benefits from the inclusion of input parameters as the frequency and the duration. Instead, when performing an all-sky short-duration search the morphology-dependent parameters are not used to train the model. The XGBoost algorithm has several hyper-parameters that define the architecture of the network [2]. In cWB, the tuning of the

[2]The main XGBoost hyper-parameters used in cWB are: 1) the loss function is logistic, 2) the tress are built with the histogram methods, to reduce the computational time, 3) the number of estimators are 20,000 optimized using early stopping, where the training stops when the validation score stops improving, 4) the maximum depth of trees is 6. The higher the value, the more complex the model and more likely to overfit, 5) the learning rate is set to 0.03, 6) the minimum child weight, i.e. the minimum sum of the weights needed in a child, is set equal to 5. If the tree partition step results in a leaf node with the sum of weights less than this parameter then the building process will stop, 7) gamma, i.e. the minimum loss reduction required to make a further partition on a leaf node of the tree, is set to 2.0. A complete explanation of XGBoost settings can be found in Ref. [130].

hyper-parameters is performed with a grid search, and the values that maximize the classification accuracy, defined as the area under the precision-recall curve, are selected.

First, this post-processing method has been applied to search for BBH mergers with cWB [132]. Chapter 7 presents a model-informed search for GW from hyperbolic encounters between compact objects using cWB and the XGBoost algorithm tuned on this specific source. The XGBoost signal-noise separation has proven to be successful for all-sky GW bursts searches as well. The author of this thesis personally contributed to the application of XGBoost in such configuration. The results, which will be briefly discussed in the following, are reported in Ref. [133].

Applying a supervised machine learning algorithm, such as XGBoost, to a burst search is a challenging task because it is crucial to preserve the model-independent nature of the search. To achieve this task the two main aspects to pay attention to are: the selection of the input features from the cWB summary statistics, and the choice of the simulations to be included in the training dataset. Concerning the first point, seven cWB input features that do not depend on the waveform morphologies are employed[3]. Any parameter linked to the morphological characteristics of the signal as frequency and duration, is excluded. Secondly, the XGBoost algorithm is not trained on GW signals that follow an astrophysical distribution, but it is trained on a stochastic set of White Noise Burst (WNB) waveforms. WNB consist of white noise contained within an ad-hoc time-frequency range. The duration and the frequency span a wide range of values. In particular, we use two sets of simulations: WNB uniformly distributed in central frequency in the range [24, 996]Hz, bandwidth [10, 300]Hz, and duration logarithmically distributed between 0.1ms and 1ms, and WNB logarithmically distributed in central frequency [24, 450]Hz, bandwidth [10, 250]Hz and duration [1, 50]ms.

Next, the comparison of the cWB search sensitivity achieved with the standard post-processing and the ML-enhanced one are reported. Typically, the search sensitivity of burst searches is evaluated in terms of the root-mean-squared strain amplitude h_{rss} at which 50% of the injections are recovered with a certain IFAR threshold, computed for the GW components of the signal h_+ and $h_\times$ as:

$$h_{rss} = \sqrt{\int_{-\infty}^{\infty} (h_+^2(t) + h_\times^2(t))dt} \tag{4.37}$$

Fig. 4.5 shows the h_{rss50} achieved with the standard cWB search (using the binning procedure) and with the ML-enhanced search (using the XGBoost algorithm) at IFAR>100 years. To prove the robustness of XGBoost method, we report the comparison between the two configurations for several different morphologies, including ad-hoc waveforms as sine-Gaussian, Gaussian pulses and WNB, and astrophysical signals, as supernova, and cosmic strings. The XGBoost classification improves the detection efficiency for all the 53 signal morphologies considered. The strongest improvement is achieved for the Gaussian pulses and cosmic strings waveforms that have a few cycles similar to low-Q noise transients.

Fig. 4.6 reports the search sensitivity in terms of the detectable GW energy radiated isotropically from a generic source, defined as:

$$E_{\rm GW}^{\rm iso} = \frac{\pi^2 c^3}{G} r_0^2 f_0^2 h_{\rm rss50}^2 \tag{4.38}$$

[3]For the all-sky search presented in Ref. [133], the cWB summary statistics used to train the XGBoost model are seven: total energy over all frequency resolutions, correlation coefficient (cc defined in Eq. 4.33), quality of event reconstruction defined as the residual noise energy over the number n of independent wavelets describing the event, square of SNR over likelihood, effective correlated SNR (ρ_0), and the shape parameters (Q_a, Q_p) mentioned above and defined in Ref. [129]. Model-dependent summary statistics as central frequency, duration, bandwidth, and chirp mass are excluded as they are strongly correlated with the signal parameters.

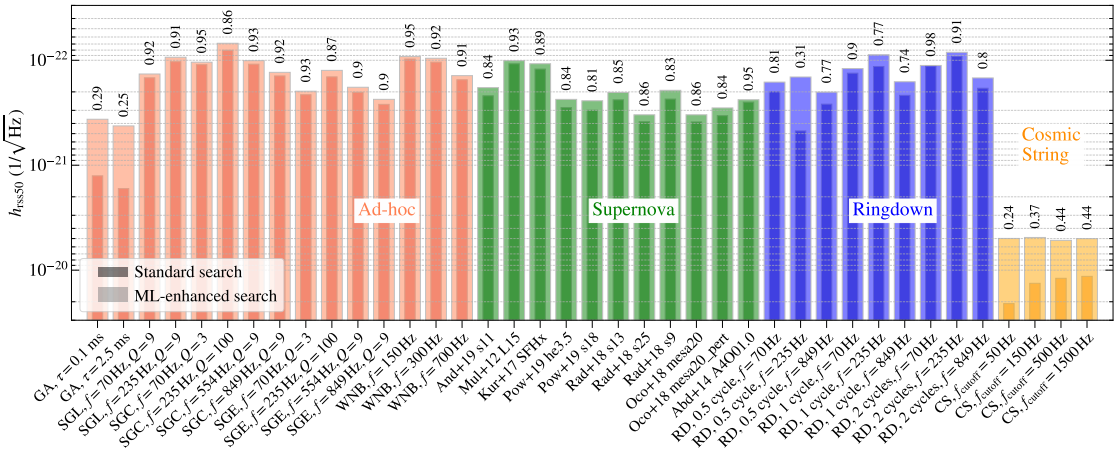

Figure 4.5: Search sensitivity in terms of $h_{\rm rss50}$ achieved with cWB with standard post-production procedure (darker colours) and with ML-enhanced cWB (lighter colors). The injections are performed in the LIGO network on O3 data and a significance threshold of IFAR$\geq$ 100 years is considered. The waveforms reported are: ad-hoc signals ordered according to central frequency (red), core-collapse supernovae (green), ringdown waveforms (blue), and cosmic strings (yellow). The values on the top show the reduction factor on $h_{\rm rss50}$ with respect to the standard search. Note that the $h_{\rm rss50}$ ordinate scale decreases going upwards, so the higher the bars the more sensitive the search [133].

where the source is assumed to be a standard siren at a distance r_0 of 10kpc, with a central frequency f_0. Since both cWB configurations do not report GW events in addition to known CBC, $E_{\rm GW}^{\rm iso}$ can be interpreted as the constraints on the product of luminosity distance and amplitude for burst sources. The ML-enhanced cWB allows setting tighter constraints across the whole frequency spectrum. Moreover, Fig. 4.7 focuses on the improvements achieved by ML-enhanced cWB on CCSNe waveforms. The figure presents the detection efficiency versus the distance of the source for three different CCSNe models. The XGBoost post-processing improves the detection efficiencies for the three models across all distances.

4.2 Alternative burst pipelines

The methodological developments and the analyses presented in the next chapters are based on cWB algorithm, that for this reason has been presented in great detail. There are several other pipelines that search for GW bursts. Next, the main algorithms used for GW burst searches within the LVK collaboration are briefly presented:

- **cWB - GMM** employs the same trigger production as cWB, as described up to Section 4.1.5, but uses a different ML-based algorithm to do the post-processing. Instead of using the decision-tree classifier XGBoost, a Gaussian Mixture Model (GMM) is trained [134]. This algorithm models a given dataset as a weighted sum of a collection of Gaussians. To improve the cWB signal-noise separation, it constructs two distinct models, one for signal and one for noise, in the multidimensional space of cWB trigger summary statistics. The input parameters should have a Gaussian distribution: before training the models, cWB summary statistics are re-parametrized or combined in order to have a distribution close

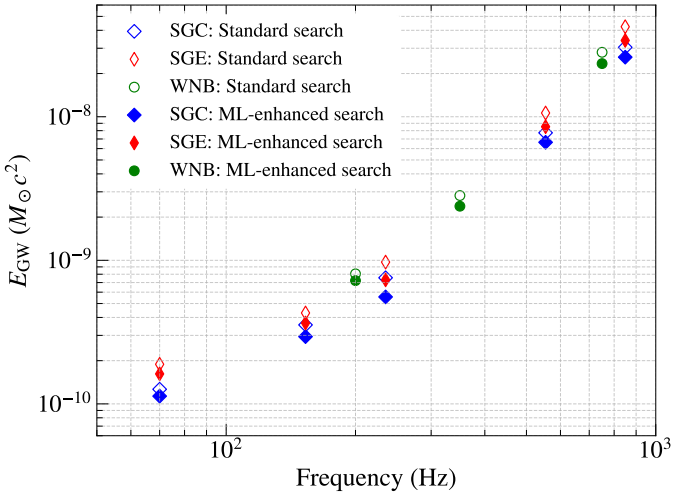

Figure 4.6: Radiated energy in GWs at 50% detection efficiency and IFAR≥ 100 years for a source distance of 10 kpc. The ML-enhanced cWB (full shapes) improves the constraints w.r.t. the standard ranking statistic (empty shapes) across the frequency spectrum for all tested morphologies [133].

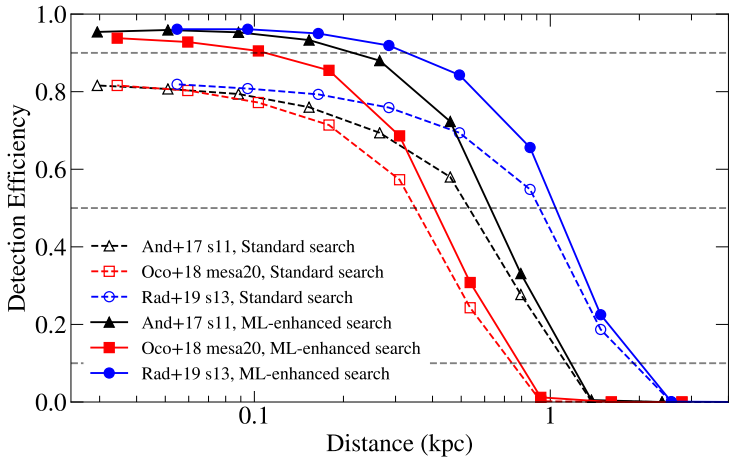

Figure 4.7: Detection efficiency vs distance for CCSNe waveforms, at IFAR≥ 100 years. The ML-enhanced search improves the detection distance at 50% detection efficiency. The probability of detections at a closer distance increases significantly [133].

to a Gaussian one. Once trained, a ranking statistic is defined as $\rho = W_s - W_n$, where W_s and W_n are the maximum likelihood statistics derived from the learned models for the signal and the noise, respectively.

- **Wavescan** is a burst pipeline for the detection and the reconstruction of GW transients [135]. The GW strains are represented in the TF domain using multiple short-time Fourier transforms. The optimal resolution at each TF location is dynamically selected. The triggers' ranking is based on the cross power statistic. The cross-power between two de-

tectors a,b calculated for each TF pixel is $C_{a,b} = r_a r_b P_a^2 P_b^2 / (r_a P_b + r_b P_a)^2$ where P is the wavelet power and r a weight coefficient to account for different detectors sensitivities. The post-processing is performed with the XGBoost algorithm, as described in Section 4.1.6.

- **BayesWave** is an unmodeled pipeline for the detection and reconstruction of GW signals, based on Bayesian statistics [136, 137]. BayesWave models the signal using Morlet-Gabor wavelets. The number of wavelet components is used to distinguish between GW signal and glitches: a GW signal is modelled with a high number of components, which increases with the number of detectors, while glitches are reconstructed with few wavelets. As a consequence, this algorithm as a lower search sensitivity towards simple GW waveforms [103]. The wavelet parameters and the number of wavelet to use are chosen using a reversible jump Markov Chain Monte Carlo. BayesWave computes the Bayes factor that the data contain a signal or there is only gaussian noise, and then the Bayes factor to distinguish between a true GW signal and a glitch. As the evaluation of the Bayes factor is computationally expensive, this algorithm is typically used to follow-up cWB candidate events with ρ_0 over a certain threshold [103]. BayesWave shows to efficiently separate glitches from signal [138] allowing a robust glitch subtraction that is crucial to infer accurately the physical parameters of the GW sources. In addition, it is used to perform consistency tests between the waveform reconstructed with minimal assumptions and the CBC waveform models [1].

- **oLIB** is an unmodelled algorithm for the detection and reconstruction of GW signals [139]. Excess of power are individuated in each detector by the Omicron algorithm [140], which performs a multi-resolution time–frequency analysis using a fast Q transform. Next, GW signals and transient noise are modelled with sine-Gaussian waveforms and the software computes the Bayes factors of the GW signal versus Gaussian noise, and of GW signal versus glitches. The joint likelihood ratio of these two Bayes factors is then used to assign the significance to each trigger, comparing with the time-shifted background distribution.

- **Xpipeline** is a software [141] used to search for GW bursts associated with an electromagnetic counterpart as gamma-ray bursts [142], magnetars bursts [106], and fast radio burst [143]. Xpipeline triggered searches are centred around the temporal and spatial position of the electromagnetic emission. This software performs a coherent analysis of GW data. First, the GW strains are divided into overlapping segments, and time-frequency maps are produced for each detector using Fourier transforms. Then, the most energetic pixels are selected and grouped together. Similarly to cWB, a likelihood statistic is maximized on a restricted portion of the sky to find the signal waveform. After candidate event identification, short-duration noise transient are vetoed comparing the coherent and incoherent energies.

- **MLy** is a machine-learning based pipeline to search for GW bursts in low-latency [144]. MLy uses a convolutional neural network and the Pearson cross-correlation between multiple GW detectors to identify GW signals and distinguish them from glitches. MLy learns the signal population using White Noise Burst waveforms, and the noise population from simulated detector noise and glitches. This approach allows controlling the glitch rate in the training data more easily and with a lower computational cost than using real background population from time-shifted data.

Chapter 5

Search sensitivity of three-detectors network in CoherentWaveBurst

Expanding the number of GW detectors has several benefits in GW astronomy, such as improving the source localization and the characterization of the GW signals. The impact of larger GW network on the detection rate is more complex, and strongly depends on the orientations and on the sensitivities of the detectors (Section 5.1).

This chapter discusses the two-detectors network, composed of the LIGO detectors, and three-detectors network, which includes also Virgo, in searches for GW bursts with the cWB pipeline. As the LIGO detectors are coaligned and senses only one GW polarization, cWB has introduced two likelihood regulators that constrain the likelihood solutions forcing the reconstruction of the LIGO dominant polarization. This strategy reduces significantly the false alarm rate, increasing the two-detectors search sensitivity (Section 5.2). To make full use of a non-aligned detector, as Virgo, the analysis has to open the search to both GW polarization components over the sky, relaxing the requirements on the signal coherence between participating detectors.

To evaluate the impact of relaxed likelihood regulators, first the two-detectors and three-detectors networks are studied though a set of simulations into Gaussian noise (Section 5.3). Next, the comparison on O3b data is presented: the latest enhancements of cWB and the use of relaxed likelihood regulators greatly improves the HLV search sensitivity (Section 5.4).

Moreover, the use of the three-detectors network for waveform consistency test between the unmodelled cWB reconstructions and the CBC models is also discussed in Section 5.5.

5.1 Network of GW detectors

Currently, the network of GW detectors is made of LIGO Livingston, LIGO Hanford, Virgo and KAGRA. In the 2030', LIGO India will join the network of ground-based GW detectors. The source localization capabilities and the detection rate prospects of the networks of GW detectors are reviewed in Ref. [37]. Large networks of detectors have several advantages: the more the detectors I) the better the sky localizations of the GW sources [37, 145], which is of primary importance for identifying a multi-messenger counterpart as in the case of GW170817 [14]; in addition II) more GW detectors increase the duty cycle of the observation. Current GW interferometers have a duty cycle of $\sim 75\%$ [1], limited by the fact that GW interferometers are

complex instruments with several optical cavities that have to be locked in resonance. More GW detectors guarantee a higher observational time that is fundamental to observe rare astrophysical events. III) A large network of detectors with different orientations improves the reconstruction of GWs and allows observing both polarization components of the GW waveforms.

Section 5.1.1 describes this latter aspect for the current GW network. Next, the use of three-detectors network for GW transient searches in the data from the third observing run is presented (Section 5.1.2).

5.1.1 The LIGO-Virgo network

This section describes the two-detectors network (HL), composed of the two LIGO interferometers, and the three-detectors network (HLV), which includes also Virgo. As the results presented in this chapter are based on O3 data, KAGRA is not considered.

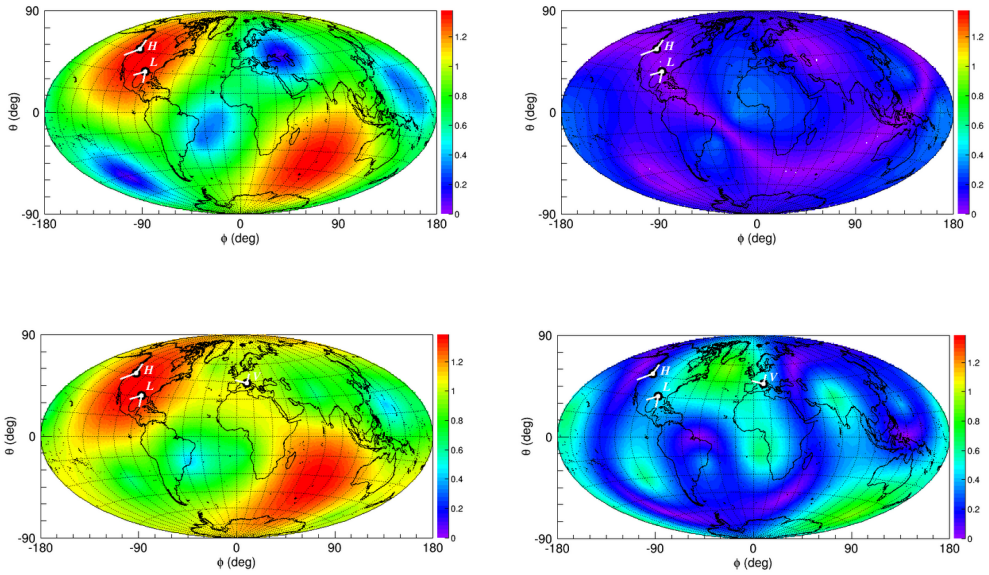

Figure 5.1: The network antenna patterns $|f'_+|$ (left column) and $|f'_\times|$ (right column) in the dominant polarization frame defined in Section 4.1.4. The first row considers the network of the two LIGO detectors (HL), the second row considers the LIGO and the Virgo detectors (HLV), assuming the same sensitivity to GWs for all the detectors. The addition of a detector with different orientation, as Virgo, improves the sky coverage reducing the blind spots of f'_+. Moreover, Virgo improves the response to the second polarization $f'_\times$. Antenna patterns for larger networks, up to five detectors are reported in Ref. [145].

The LIGO detectors are almost aligned, so their antenna patterns are similar. The addition of another detector with a different orientation, such as Virgo, improves the sky localization of GW signals and reduces the blind spot regions from which GW signals are unlikely to be detected. Fig. 5.1 shows the antenna patterns f'_+ and $f'_\times$ for the HL and HLV networks. From the figure, it is evident that the HLV network has a better sky coverage: HL f'_+ has four wide blind spots, while with the HLV network has only two regions with lower sensitivity.

Fig. 5.1 shows also another important aspect: a single detector, or two aligned detectors, is almost blind to one GW polarization per each direction [146]. Consider a simple case of a GW interferometer with arms along the x and y axis, and a GW passing perpendicular w.r.t. the detector plane. The plus polarization affects the distance between the beam splitter and one test mass in opposite phase with the other mass, so that $|L_x - L_y|$ is maximum. Instead, the cross polarization, that is rotated of 45° w.r.t h_+, affects both arms in the same way, so that the differential variation $|L_x - L_y|$ is null. Hence in this frame, the interferometer can not observe the cross polarization, and it is sensitive to only one component of the GW signal.

A network composed of detectors with different orientations, as HLV, senses the cross polarization from a fraction of the sky. The more the detectors with different orientations, the better the response to both GW components.

The detection of the both polarizations increases the characterization of the GW signals and the astrophysical generating processes. Ref. [147] proposes a method to estimate the waveform polarizations for burst searches using the HLV network with detectors operation at design sensitivity. The results achieved considering only Gaussian noise are promising showing a reliable reconstruction of both plus and cross polarizations. Ref. [148] presents a method to probe the GW polarizations for GW events with sky localization known, for example for an associated electromagnetic observation, using the four-detectors not-aligned network (HLVK).

Moreover, larger GW networks allow probing the polarization structure of GWs [90]. GR predicts that GWs have two tensor polarization modes, referred to as plus and cross (Eq.1.5). Alternative theories of gravity predict up to six independent GW polarization states (two tensor, two vector and two scalar modes). The observation of one of these additional polarizations would constitute a violation of GR. One of the two scalar polarization cannot be measured with differential arms detectors, so there remains five different polarization states that could be investigated with GW interferometers. To uniquely distinguish five polarizations, five not-aligned detectors are required. When fewer detectors are available, it is possible to study extreme polarization alternatives such as only tensor polarizations modes versus only vector modes versus only scalar modes, or it is possible to assume specific theoretical predictions for specific features given by the additional polarization states. A method to test alternative GW polarization states is the construction of the null stream, i.e. a linear combination of the detector outputs that, given the source localization, is blind to the polarization tensor modes [149]. At least three detectors are necessary to construct such null stream. Moreover, morphology-independent Bayesian analyses have been used to test GW polarization states [90].

5.1.2 The LIGO-Virgo network for burst searches

The previous chapter described in detail cWB, a software for burst searches that distinguishes potential astrophysical signals from glitches using the coherence among multiple detectors. The sky coordinates and the GW waveforms are reconstructed maximizing the cWB likelihood statistics (Section 4.1.4). cWB sky localization capabilities are discussed in Ref. [145]: the localization depends on several aspects as the signal strength, the signal morphology and its polarization. There is a significative gain in GW detection and pointing performances when at least three detectors are participating in the measurements.

The purpose of this chapter is to evaluate the search sensitivity, i.e. the capability of detecting GW signals, for the HL and HLV networks in burst searches. The LIGO detectors have been built to maximize the overlap between their antenna patterns, so that astrophysical GW signals are highly coherent in the HL network. Instead, the Virgo detector has a different orientation: this favours the sky coverage and enables the observations of both polarizations, but results in a lower coherence of an astrophysical signal in different detectors. Hence, a network composed of

Virgo and a LIGO detector (HV and LV) has a lower capability of rejecting transient noise based on the coherent and uncoherent energy (Eq. 4.34). cWB search sensitivity to GW burst is lower in HV and LV than the one achieved in the HL network, even assuming the same sensitivity for all the detectors.

At this point one should examine how is the HLV sensitivity w.r.t. HL network, and if the inclusion of a third detector improves the detection efficiency in burst searches. At first, one could imagine that the more the detectors, the more the SNR collected for an astrophysical signal, and so the better the search sensitivity independently from the alignment and sensitivity of the detectors. This is the case for template-based searches: for example, the pipeline pyCBC [64] uses a multi-detector ranking statistics that includes a network sensitive volume correction that accounts for different detectors sensitivities [150]. If a detector with lower sensitivity is added to the network, the search does not improve substantially, but there are no injections recovered in the two-detector HL analysis which were not seen in the HLV analysis. So, the HLV network can be analysed without the risk of missing weaker events, and the only drawback is an increase in the computational cost.

For burst searches the treatment is more complicated: for the all-sky short-duration LVK search on the third observing run, the Virgo data were analysed only when one of the two LIGO detectors was not operating. The HLV network achieved a lower sensitivity than the HL: Fig. 5.2 shows the cWB search sensitivity, measured in terms of h_{rss50} (Eq. 4.37), for a wide range of short-duration simulations recovered with an IFAR>100 years. These simulations were performed for the LVK all-sky short-duration search for GW burst in the third observing run [103]. The search sensitivity for the HL network is significantly higher than the one achieved with HLV for all the waveforms tested. As described in detail in the next section, cWB applies two likelihood regulators to reject the contributions yield from the polarization not observed by the HL network. These regulators effectively mitigate transient noise in HL analyses, while limit the contribution of a third detector with a different orientation to the measurements. The investigations in Section 5.3 and 5.4 will discuss with more detail these concepts.

Thus, the O3 zero-lag data of the HLV network (see Section 4.1.5) was not analysed. The contribution of Virgo for the all-sky burst searches was limited to the sky localization of the GW sources and the period of time when one of the LIGO detector was not operating [1].

Both the HL and HLV results in Fig. 5.2 are obtained using hard regulators on the likelihood, defined below. This choice has long been considered not optimal for the analysis of a network of GW detectors with different orientation, as HLV [103].

5.2 CoherentWaveBurst likelihood regulators

A GW network made of aligned detectors is sensitive only to one GW polarization (Fig. 5.1). Most of the SNR of an incoming signal is produced by the dominant polarization, denoted by convention by f_+, while the contribution of the second component is minimal. In these cases, the cWB likelihood (Section 4.1.4) can be constrained using the so called regulators. The regulators reject unlikely solutions of the likelihood maximization arising from the second component of the signal ($f_\times$). These solutions are likely not produced by a GW signal with comparable strength in both polarization components, but by terrestrial noise. The effect of the regulators is an

[1] The other burst pipeline contributing to the all-sky short-duration search in O3 was BayesWave (presented in Section 4.2). The performance of BayesWave on the HLV network is investigated in Ref. [151]: BayesWave ranking statistics increases with the number of detectors. Ref. [151] reports an increase in the detection efficiency of simulated signals into Gaussian noise using HLV w.r.t. HL. The results presented do not have a significance threshold and so it is not possible to compare the search sensitivity with cWB.

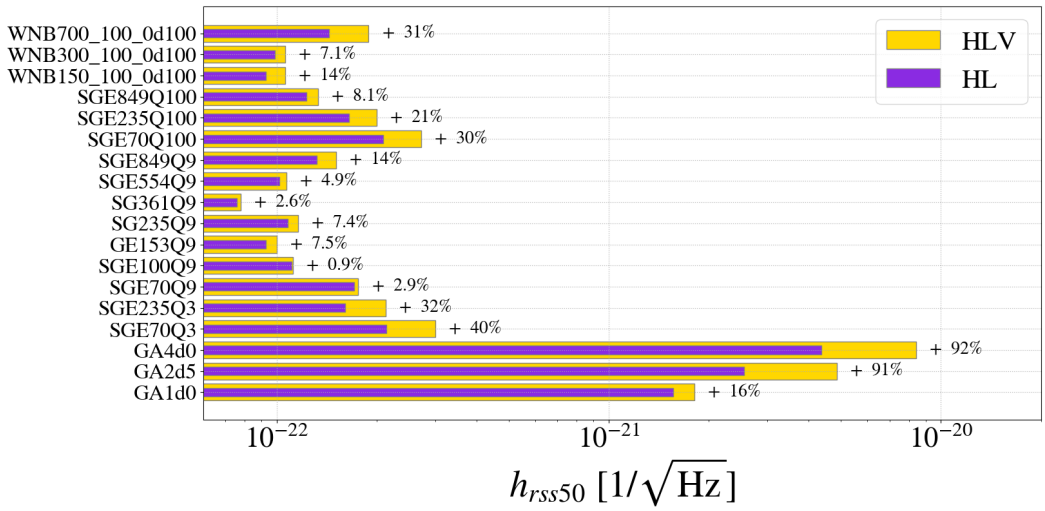

Figure 5.2: cWB search sensitivity, measured in terms of h_{rss50}, for the three-detectors network HLV (yellow) and two-detectors network HL (violet) on O3b data. A significance threshold of IFAR>100 years is considered. These results were prepared for the O3 all-sky short-duration LVK publication [103]: the post-processing is performed with the binning procedure, and not the XGBoost decision-tree presented in Section 4.1.6. The waveforms injected are Gaussian pulses (GA), sine-Gaussian (SG) and white noise burst (WNB).

effective reduction of the number of false alarms triggers, while loosing a limited fraction of potential signals.

The definition of the regulators is based on empirical arguments, determined comparing the distributions of various cWB statistics for false alarm triggers and signal simulations. To define the likelihood regulators, we introduce the dual stream likelihood analysis and the polarization phase transformation, following Ref. [146]. cWB likelihood (Eq. 4.9) includes the noise-scaled data stream $\mathbf{w}$ (Eq 4.8). In addition, one can build a second likelihood using the quadrature data stream $\tilde{\mathbf{w}}$ that is phase shifted by 90° w.r.t $\mathbf{w}$ (see Appendix B). Both time-series are analysed with the procedure detailed in the fourth chapter (data conditioning, time-frequency transformation and pixels clustering), resulting in the two likelihood $\mathcal{L}$ and $\tilde{\mathcal{L}}$. Clearly, the shifted data stream is equivalent to $\mathbf{w}$, but its likelihood might contain different contribution of the noise $n(t)$ and the signal $h(t)$, so that the signal reconstruction might be better using the dual streams.

Next, it is useful to define a phase transformation to the data $\mathbf{w}$ and $\tilde{\mathbf{w}}$ for an arbitrary shift phase λ applied to each sample as:

$$\begin{aligned} \mathbf{w}'[i] &= \mathbf{w}[i]\cos\lambda + \tilde{\mathbf{w}}[i]\sin\lambda, \\ \tilde{\mathbf{w}}'[i] &= \tilde{\mathbf{w}}[i]\cos\lambda + \mathbf{w}[i]\sin\lambda \end{aligned} \tag{5.1}$$

To compute the likelihood (Eq. 4.9), the same transformation can be applied to the detector responses $\mathbf{g}[i]$ (Eq 4.8) and its 90° shifted phase $\tilde{\mathbf{g}}[i]$. This phase transformation allows introducing the polarization phase transformation, defined as the scalar product of the network responses to a GW signal ($\mathbf{g}[i]$,$\tilde{\mathbf{g}}[i]$) and the antenna pattern $\mathbf{e}_+[i]$ as:

$$\cos\lambda \propto (\mathbf{g}[i]\cdot\mathbf{e}_+[i]), \quad \sin\lambda \propto (\tilde{\mathbf{g}}[i]\cdot\mathbf{e}_+[i]) \tag{5.2}$$

Thanks to this transformation, we can move to the signal polarization pattern: a pattern where different GW polarizations are observed by the network with distinct responses.

To describe the polarization of a generic wave, we adopt the following parameterization of a signal, neglecting for simplicity the pixel index i:

$$\begin{aligned} \mathbf{g} &= h_1 \mathbf{F}_+(\psi) + e h_2 \mathbf{F}_\times(\psi) \\ \tilde{\mathbf{g}} &= -h_2 \mathbf{F}_+(\psi) + e h_1 \mathbf{F}_\times(\psi) \end{aligned} \tag{5.3}$$

where h_1 and h_2 are the strain amplitudes, e is the wave ellipticity equal to the amplitude ratio of the GW polarization states, and ψ the polarization angle. These parameters are found maximizing the likelihood statistics. The antenna pattern vectors used above are related to the dominant polarization frame $(\mathbf{f}_+, \mathbf{f}_\times)$ as:

$$\begin{aligned} \mathbf{F}_+(\psi) &= \mathbf{f}_+ \cos(\gamma) - \mathbf{f}_\times \sin(\gamma) \\ \mathbf{F}_\times(\psi) &= \mathbf{f}_\times \cos(\gamma) - \mathbf{f}_+ \sin(\gamma) \end{aligned} \tag{5.4}$$

Applying the dual phase transformation to $\mathbf{g}$ and $\tilde{\mathbf{g}}$, the resulting signal responses are described by three vectors $(\mathbf{g'}_+, \mathbf{g'}_\times, \tilde{\mathbf{g}}'_\times)$ in the plane $(\mathbf{f}_+, \mathbf{f}_\times)$:

$$\begin{aligned} \mathbf{g}'_+ &= \mathbf{f}_+ h_0 N \\ \mathbf{g}'_\times &= -\mathbf{f}_\times h_0 \frac{1-e^2}{2} \sin(2\gamma) N^{-1} \\ \tilde{\mathbf{g}}'_\times &= \mathbf{f}_\times e h_0 N^{-1} \end{aligned} \tag{5.5}$$

where $h_0 = \sqrt{h_1^2 + h_2^2}$ and is a N normalization constant. The detailed derivation of the above equation, in particular for the $\tilde{\mathbf{g}}$ cross component is reported in Appendix B. Fig. 5.3 shows the polarization pattern $(\mathbf{g}', \tilde{\mathbf{g}}')$. The polarization pattern defined above simplifies in particular cases: for linearly polarized wave $e = 0$ and the 90° phase $\tilde{\mathbf{g}}'$ is null, for circular waves $e = 1$ and $\mathbf{g}'_\times = 0$, and for elliptical waves $0 < |e| < 1$. For aligned detectors, only the plus polarization can be measured, while the original GW polarization state cannot be reconstructed. The parameters e and ψ defined above are free parameters when looking for unmodelled GW signals, while they can be constrained when looking for GW with a certain polarization state. Loose constraints on h_0, e and ψ can be applied to search for GW signals with specific polarizations [145].

The polarization constrains are different from the likelihood regulators mentioned above, but are built from the same frame. The importance of each detector in the network depends on the sensitivity of the detectors, and the sky localization of the source. As mentioned before, aligned detectors have a lower sensitivity to the second component of the GW. This unbalance is express by the network alignment factor α, defined in Eq. 4.27. α is much lower than 1 for almost all sky direction for the HL network (see Fig. 4.27), hence the majority of the SNR of the signal is given only by $\mathbf{f}_+$. This a priori information can be used to exclude likelihood solutions due to $\mathbf{f}_\times$.

The hard regulators used in Fig. 5.2 constrain the likelihood analysis to ignore the $\times$ response of the network. cWB has two likelihood regulators, called Γ and Δ. Γ regulator is built looking at Eq. 5.5: the cross response $(\mathbf{g}'_\times, \tilde{\mathbf{g}}'_\times)$ are null when $\sin(2\gamma)$ and e goes to zero. Ref. [146] shows that for the HL network the majority of the Gaussian noise is concentrated in the region with low e and $\sin(\gamma)$, while signals injected with random polarization are concentrated in the region with $\sin(\gamma) \sim 1$. Hence, it is possible to define R:

$$R = \sqrt{e^2 + \sin^2(\gamma)} \tag{5.6}$$

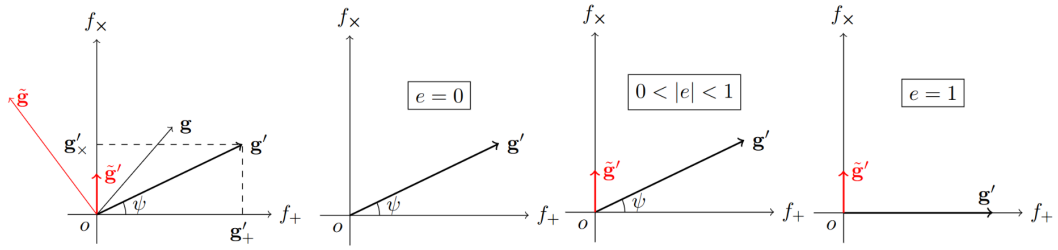

Figure 5.3: (*left*) Sketch of the polarization pattern $(\mathbf{g}', \tilde{\mathbf{g}}')$ obtained with the dual stream phase transformation (Eq. 5.1) in the dominant polarization frame $(\mathbf{f}_+, \mathbf{f}_\times)$. Black vectors indicate the 0° phase responses, and red vectors the 90° ones. The second, third and fourth figures show the signal polarization pattern responses in the linear case ($e = 0$), elliptical ($0 < |e| < 1$) and circular ($e = 1$).

and requiring R above a certain threshold R_0 allows rejecting a large fraction of noise, while loosing a small fraction of signals.

In particular, the implementation in cWB sets a condition to reject the cross response [152]:

$$R - 0.9 + (0.5 - 1/I_{net})(1 - \alpha) - \frac{F_{net} \times \ln(\Gamma)}{(2I_{evt})^2} < 0 \tag{5.7}$$

I_{net} is the network index which goes from 1 o the total number of detectors, and indicates the effective number of detectors available weighted by the antenna pattern. I_{evt} is the event index that represent the effective number of detectors contributing to the event weighted by the energy, α the network alignment factor, F_{net} the network antenna sensitivity ($F_{net} = \sqrt{(|\mathbf{f}_+|^2 + |\mathbf{f}_\times|^2)/2I_{net}}$). Γ can be set by the user in cWB production in [0,1]. To understand the condition in Eq. 5.7, we made few examples:

- If Γ=0, no constraint is applied.
- If $\Gamma = 1$, the condition is $R - 0.9 + (0.5 - 1/I_{net})(1 - \alpha) < 0$. For the HL network $I_{net} \sim 2$ and $\alpha \ll 1$ so the triggers with $R < R_0 \sim 0.9$ are rejected. The maximum value of R is 1, so this condition applies a strong rejection. If $\Gamma = 1$ and the network has more detectors, as HLV α is higher and $1/I_{net}$ is lower (lets imagine three detectors fully participating $1/I_{net} \sim 0.3$ and $\alpha \sim 0.5$), so $R_0 \sim 0.8$.
- If we lower Γ the term $\frac{F_{net} \times \ln(\Gamma)}{(2I_{evt})^2}$ is always negative and decreases the threshold R_0.

Typically, Γ is set to 1 (results in Fig. 5.2), and so it is called 'hard' regulator. In the following, we discuss lower Γ values, i.e. less constrained. When the regulator is applied ($R < R_0$) the signal components $\mathbf{g}'_\times$ and $\tilde{\mathbf{g}}'_\times$ are set to zero. The regulators are applied individually to each time-frequency pixel.

In addition, the Γ regulator is enhanced by a second condition [152]:

$$|\mathbf{f}_\times|^2 < \Gamma \frac{(I_{evt} - |\mathbf{f}_\times|^2)}{I_{net}} \tag{5.8}$$

the pixels where the condition is satisfied are set to zero. This condition suppress sky localizations where the network sensitivity is low. If $\Gamma = 1$, in the LH network $I_{net} \sim 2$ and $I_{evt} \sim 2$ so sky localizations where $|\mathbf{f}_\times| \lesssim 0.16$ are suppressed.

The second likelihood regulator, called Δ, controls the ratios between the contribution to the likelihood from different separate polarizations [146]. The definition of Δ is:

$$\Delta = I_{evt}^{-1} - \alpha|\nu(e_+) - \nu(e_\times)| \tag{5.9}$$

where I_{evt} is the event index, $\nu(e_+) = \sum_k e_+[i]^4$ and $\nu(e_\times) = \sum_k e_\times[i]^4$. The condition $\Delta > \Delta_0$, where Δ_0 is set by the user and typically is 0.5, is used to identify the cases when two or fewer detectors participate in the measurement. For two coaligned detectors $|\nu(e_+) - \nu(e_\times)|$ is null and $I_{evt} \leq 2$. The condition $\Delta > 0.5$ imposes a circular polarization ($\mathbf{g}'_+ = \mathbf{w}_+, \mathbf{g}'_\times = 0, \tilde{\mathbf{g}}'_\times = \tilde{\mathbf{w}}_\times$). For larger networks, I_{evt}^{-1} is lower, and the alignment factor α increases, so that Δ decreases and the constraint is unlikely applied. As the focus of the next sections is HLV network, the condition $\Delta > 0.5$ is not verified, so the Δ regulator is not investigated.

Releasing the regulators enhances the contribution of the non-aligned detector, Virgo in our case, and increases the SNR recovered from a signal. On the other side, softer regulators allow more transient noise to be recovered, increasing the false alarm rate. It is not possible to weight the contribution of these effects on the cWB search sensitivity *a priori*, but it is necessary to perform a set of simulations.

5.3 Likelihood regulator in LIGO-Virgo network with Gaussian noise

In the next sections, the effect of the Γ regulator is investigated. Ad-hoc waveforms characterized by different durations and frequencies are injected into Gaussian noise, and are recovered with cWB testing different values for Γ. The simulations are injected at 9 different h_{rss} amplitudes, between 5.5×10^{-24} $1/\sqrt{\text{Hz}}$ and 4.5×10^{-22} $1/\sqrt{\text{Hz}}$, to simulate signals with different SNR. The waveform families injected here are sine-Gaussian waveforms (SG) defined as:

$$\begin{aligned} h_+(t) &= h_1 \sin(2\pi f_0) \exp\{-t^2/\tau^2\} \\ h_\times(t) &= h_2 \cos(2\pi f_0) \exp\{-t^2/\tau^2\} \end{aligned} \tag{5.10}$$

where h_1, h_2 are the waveform amplitudes, f_0 is the central frequency, and τ is related to the Q factor as $Q = \sqrt{2}\pi f_0 \tau$. We consider both circular SG waveforms which assume an optimally oriented source, and elliptical polarization (SGE) which are uniform in cosine of the inclination angle between the total angular momentum and the line of sight. Moreover, we inject Gaussian pulses (GA) described by their duration and linearly polarized, and unpolarized band-limited white-noise bursts (WNB), defined by their lower frequency bound, bandwidth, and duration. The simulated signal sources are drawn from a uniform distribution in solid angle over the sky, as in Ref. [103].

The use of Gaussian noise simplifies the interpretation of the results, and significantly reduce the computational cost of these investigations. Indeed, when analysing real data the search sensitivity is greatly affected by the tail of the background distribution that contains loud glitches. To discuss robust results, it is necessary to accumulate enough statistics. In addition, in Gaussian noise the cWB post-processing can be done applying some simple cuts. In real GW data, an efficient post-processing is done by a decision-tree algorithm XGBoost (Section 4.1.6). This latter requires a certain amount of samples in the training dataset that would be prohibitive to accumulate for each of the configurations tested below.

For the investigations in Gaussian noise, we use $\sim$ 7 days of data, and we accumulate 3.8 years of background using time-shifts. We require only the correlation coefficient *cc* (Eq. 4.33) to

be > 0.7 and norm > 2.5[2] (standard cuts in all-sky searches [103]). For each tested configuration, we evaluate the search sensitivity in terms of $h_{\rm rss50}$ (Eq. 4.37), i.e. the strain amplitude at which 50% of the injections are recovered with a IFAR>1 year.

At first, we consider the HLV network assuming the Virgo to be as sensitive as LIGO Livingston in O3b (Section 5.3.1). Next, we consider the HLV network with the detectors PSD in O3b (Section 5.3.2).

5.3.1 LIGO-Virgo network with equally sensitive detectors

This section studies the effect of the Γ regulators on the HLV network assuming similar sensitivities for each detector, in particular we consider the LIGO O3b PSD for the LIGO detectors, and the LIGO Livingston PSD for Virgo (see Ref. [1] for the sensitivity curves). We test the value $\Gamma = 1$, which is the same used for analysing the HL network and imposes a hard likelihood constraint, and the value $\Gamma = 0.5$, referred to as soft, that apply a lower penalization to the cross responses.

The detection efficiencies, i.e. the number of recovered simulations, without a significance threshold, over the total number of injected signals, are 42% for HL, 44% for HLV with hard gamma, and 49% for LHV soft gamma. Fig. 5.4 shows the search sensitivity expressed in terms of h_{rss50} for ad-hoc simulations recovered with IFAR$>$ 1 year. The error bars on the h_{rss50} values are computed from the detection efficiencies at each injected amplitude. As one could expect, the HL network has a worse sensitivity across all the waveforms tested.

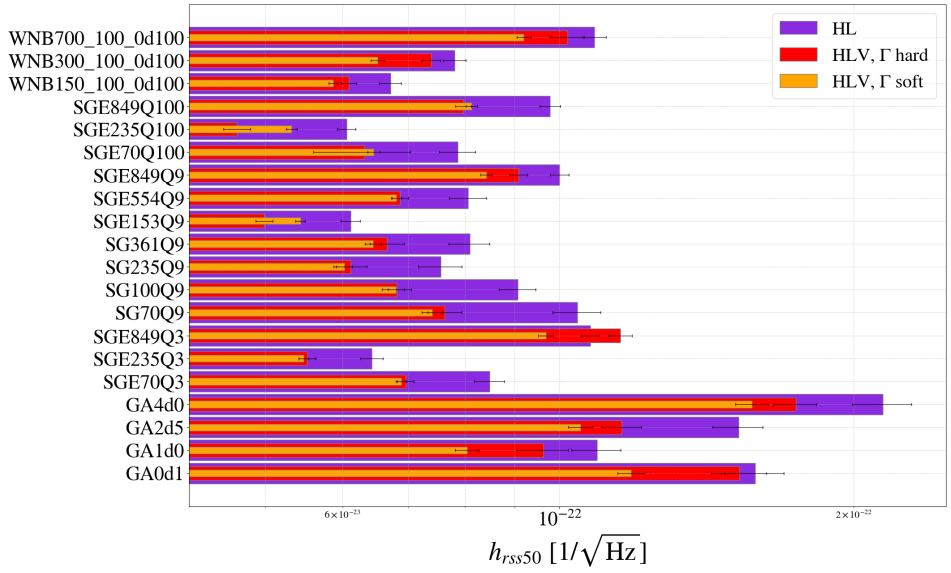

Figure 5.4: Search sensitivity measured in terms of h_{rss50} for a wide range of simulations injected in Gaussian noise and recovered by cWB with IFAR$>$ 1 year. Note that here we assume for Virgo the same ASD of LIGO Livingston. The HLV network with soft regulator (orange) performs better than the HLV hard regulator (red) for most of the waveforms. As expected, the HL network (violet) has a lower sensitivity.

[2]cWB norm is the ratio between the total energy over all time-frequency resolution levels and the reconstructed energy of the event.

The soft regulator on the HLV network enhances the sensitivity w.r.t. the hard regulator for the majority of the injections (for WNB the h_{rss50} is decreased by [-5, -13]%, for GA [-6,-20]%, SG +0.88% -13%). The hard regulator is better for sine-Gaussian (SG) waveforms with Q factor set to 100 ($h_{rss50} \sim +7\%$) . These waveforms have several cycles, without a strong modulation in amplitude. An example of such signal and the corresponding cWB reconstruction are shown in Fig. 5.5. The lower efficiency achieved by the soft regulators might be explained looking at the reconstructions of the sky positions. Typically, a softer likelihood regulator promotes

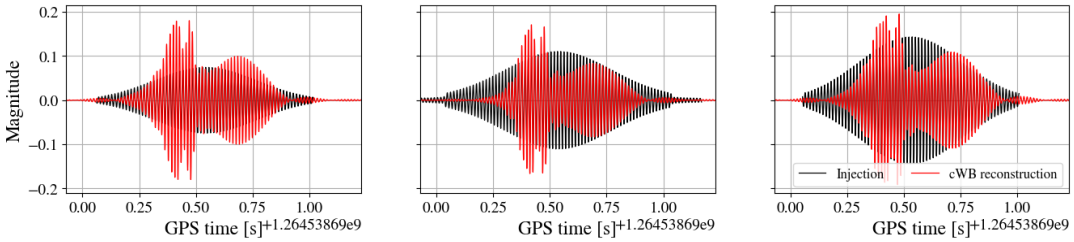

Figure 5.5: Example of a sine-Gaussian Q100 and central frequency at 70Hz injected waveform (black) and the corresponding cWB reconstruction (red), in LIGO Hanford (*left*), LIGO Livingston (*center*),and Virgo (*right*). The reconstructed network SNR is 10.9.

the importance of all the detectors in the network, and provides a better sky localization of the GW sources. This can be seen in Fig. 5.6 that reports the cWB localization precision, measured in terms of sum of sky pixels area with integrated sky probability equal to 50%. The first column shows the localization area for SG $Q100$ waveforms, while the second column is dedicated to WNB that have a long duration as SG $Q100$ but have several distinct amplitude peaks. Each figure in Fig. 5.6 contains signals injected at a fixed h_{rss} amplitude. Looking at WNB signals, the soft regulator reconstructs a smaller area, i.e. a more precise sky localization, both for low and high signal amplitudes. Instead, for SG $Q100$, the sky localization is better using hard regulator. Ref. [145] investigates cWB sky localization capabilities injecting SG with Q factor up to 9, and highlights that these waveforms have less accurate source localization w.r.t. other simulations. In addition, Ref. [153] observes a bias in cWB estimated position using HLV network which size and direction depends on the choice of the regulators. As SG waveforms with high Q factor have several cycles without sharp features in the signal envelope, the determination of the source localization is particularly difficult: especially for lower SNR signals, if the cWB peak reconstruction is not accurate (as in Fig. 5.5) it is possible that the signals from different detectors are not correctly superimposed, and the estimation of the time delay used to localize the source is inaccurate. In turn, if the sky localization is wrong, cWB does not recover correctly the coherent and uncoherent components of the signal resulting in a lower ranking statistics ρ, and in the end a lower search sensitivity.

To summarize, when the detectors have the same sensitivities, the soft Γ regulator for the HLV network achieves a better search sensitivity for the majority of the waveforms tested, and the HLV network is always better than HL with an improvement in h_{rss50} of [-15, -19%] for WNB, [-25, -31]% for GA, and [-10, -33]% for SG.

5.3.2 LIGO-Virgo network with realistic O3b sensitivities

This section investigates the impact of Γ regulator in a more realistic situation, i.e. considering the actual Virgo sensitivity. The sensitivity curves of the three detectors in O3b are reported in

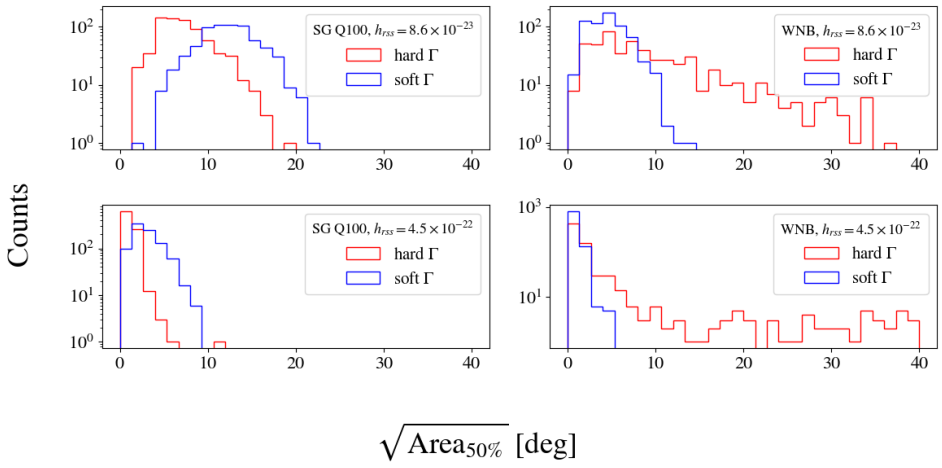

Figure 5.6: Sky area, measured in terms of sum of sky pixels area with integrated sky probability equal to 50% obtained with HLV network with hard gamma regulator (red) and soft regulator (blue). The first row contains signals injected at a fixed strain amplitude ($\sim 8.6 \times 10{-}23\ \sqrt{1/\text{Hz}}$), and the second row contained stronger signals ($h_{rss} \sim 4.5 \times 10{-}22\ \sqrt{1/\text{Hz}}$). For sine-Gaussian (SG) Q100 simulations the sky localization is enhanced using hard regulator, while for white noise bursts (WNB) is better using soft regulator.

Ref. [1]: at intermediate frequencies ($\sim$ 160Hz) the Virgo ASD is about a factor 2.5 higher w.r.t. LIGO, while at higher frequencies ($\sim$ 700Hz) the gap increases to about a factor $\sim$ 4.

As the sensitivity of the Virgo detector is lower, we expect a lower gain in using the three-detectors network w.r.t. the case presented in the previous section. Releasing the regulators enhances the contribution of Virgo, increasing the SNR collected from a signal. At the same time, softer regulators allow more transient noise to be recovered, increasing the false alarm rate. The more the gap of the Virgo sensitivity w.r.t. the other detectors, the more the second effect prevails, lowering the efficiency of the HLV network.

We inject the same ad-hoc waveforms and the detection efficiency found, without a significance threshold, are 42% for HL, 41% for HLV with hard Γ, and 43% for HLV with soft Γ. The HL network has a slightly higher efficiency for weaker signals (0.7% for HL and 0.55% for HLV hard and 0.52% for HLV soft at $h_{rss} = 5.5 \times 10^{-24} 1/\sqrt{\text{Hz}}$) while for stronger signals ($h_{rss} = 4.5 \times 10^{-22} 1/\sqrt{\text{Hz}}$) 91% for HL, 89% for HLV hard and 94% for HLV soft).

We evaluate the h_{rss50} at IFAR>1 year for the two HLV configurations as before ($\Gamma = 1$ and $\Gamma = 0.5$), and we find that the hard regulator outperforms the soft regulator for 18 over 20 waveforms tested. Using soft gamma, the h_{rss50} increases for SG Q=3 of [+8,+13]%, for Q =9 [+4,+20]% for SG Q =100 [+6,+14]%, and it is similar for WNB (+$\sim$ 2%), and for GA [3].

We test an intermediate configuration selecting a semi-soft regulator: $\Gamma = 0.8$. This value performs slightly better than the HLV hard configuration for 16 over 20 waveform. In Fig. 5.7, we compare the best HLV configuration ($\Gamma = 0.8$) with the HL: the HLV network performs

[3]In Appendix A.3, we investigate the capability of cWB to detect overlapping GW signals. We injected CBC GW waveforms in Gaussian noise from the HLV network using O3b ASD, as in this section. We evaluate cWB sensitivity using both hard and soft Γ regulator, and we obtain a higher detection efficiency with $\Gamma = 0.5$. The cWB configuration used in that case is slightly tuned towards CBC, having a diagonal pattern for time-frequency pixels selection and a post-production cut that remove triggers with central frequency above 512Hz. These constraints control the increase of false alarm rate produced by relaxed regulators.

better on 15 over 20 waveforms injected, with percentage of improvements between -0.42% to -17%. The HL network has a slightly better sensitivity for GA0d1, a short-duration single-cycle signal with the lowest frequency band, and for signals at high frequencies (as WNB at 700Hz, and SG at 849Hz and at 361Hz). This is expected, since at higher frequencies the Virgo ASD gets more distant from LIGO ones, and so the signals are less coherent and have a lower cWB ranking statistic ρ.

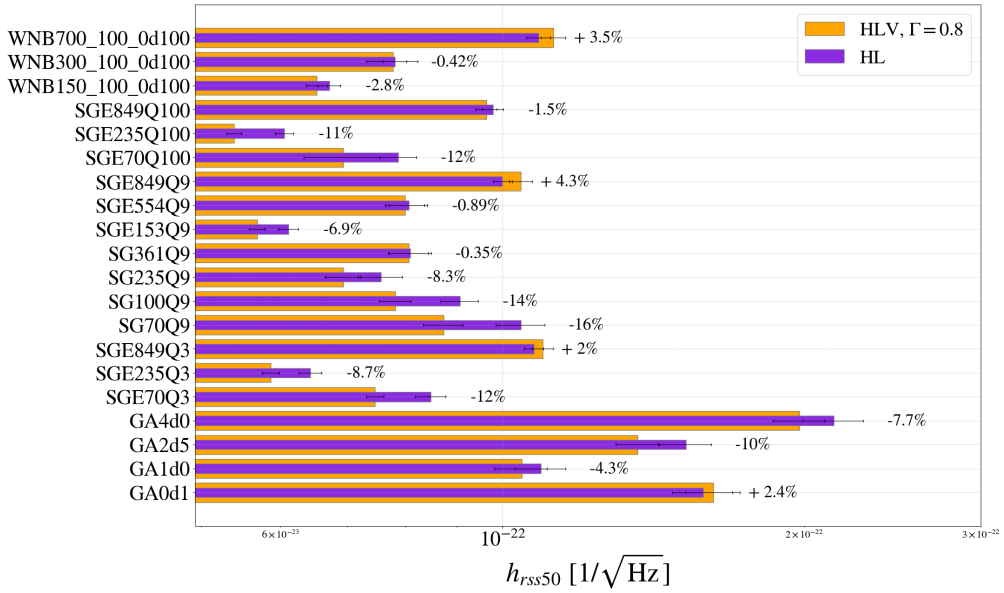

Figure 5.7: Search sensitivity for the HLV and HL networks for ad-hoc waveforms injected in Gaussian noise with O3b ASD. The HLV network with semi-soft regulator $\Gamma = 0.8$ (orange) performs better than HL network for most of the waveforms. A significance threshold of IFAR>1 year is considered.

5.4 Re-analysis of LIGO-Virgo network in O3b data

This section reports the cWB analysis of HL and HLV networks in the frequency range [16, 2048]Hz on a subset of 40 days of O3b data, collected between January 5 and February 14, 2020. This period was selected by the LVK collaboration to perform a mock-data-challenge to compare the search sensitivity of various bursts pipelines (see Section 4.2). The detectors' PSD are the same used in the previous section (Section 5.3.2). However, real data also contains glitches: the co-alignment of the LIGO detectors and the hard likelihood constraint on the HL network enable an efficient mitigation of transient noise, but at the same time the coincidence between a larger number of detectors also improves the rejection of glitches in larger networks. However, if the network has a detector with different orientation and different sensitivity the capability of rejecting transient noise is lower. Indeed, cWB might reconstruct glitch in Virgo data as coherent signals in HLV from the sky regions where the LIGO antenna pattern is low. In addition, as the Virgo sensitivity is lower, cWB might also reconstruct with HLV the same false alarm trigger found in HL. From the analyses done for the LVK all-sky short-duration burst search [103], the HL network shows a significantly better sensitivity than HLV (Fig. 5.2) and the HLV on-source

data were not analysed.

The results reported in the following have been obtained using slightly relaxed Γ regulator: from the tests reported in the previous section on Gaussian noise, $\Gamma = 0.8$ is the best configuration for the HLV network. In addition, to analyse real O3b data we employ the latest cWB configuration that uses the machine-learning based post-processing XGBoost (described in Section 4.1.6). This method shows to successfully improve the rejection of transient noise. In Ref. [133], we test the ML-enhanced cWB also on the HLV network: we employ the same XGBoost configuration and the same set of white noise bursts simulated signals to train the model as for the HL network. Compared to the standard HLV analysis, which was performed with the multiple binning procedure, XGBoost improves the search sensitivity for the majority of the waveform tested (48 out of the 53 waveforms including ad-hoc waveforms, ring-down cosmic strings and CCSNe). For that analysis, Γ was set equal to 1 for the HLV network. The application of XGBoost does not close the sensitivity gap between HLV and HL networks, likely because an extensive optimization was done for the HL network, and the selected configuration was then applied to the HLV network. The combination of relaxed regulators and XGBoost proposed here seems particularly favourable: indeed, the increase of the false alarm rate produced by softer regulators can be counterbalanced with a more efficiency glitch mitigation.

First, we see that the HLV with semi-soft regulator ($\Gamma = 0.8$) is better w.r.t. HLV with $\Gamma = 1$ for all the waveform tested (except GA0d1). The h_{rss50} improvement for WNB is [-3, -7]%, for GA [-18,-22]%, for SG Q =3 [-12,-21]%, for Q =9 [-11, -23]%, and for Q =100 [-4,-11]%.

Next, we compare the HL and HLV ($\Gamma = 0.8$) analyses. The detection efficiencies achieved for the HL network is 41.1% and for HLV 41.4%. As in the Gaussian case, at lower amplitudes the efficiency is higher in HL (0.96%) than HLV (0.57%), while at higher amplitude HL is 90% and HLV 92%. Fig. 5.8 shows the search sensitivity for the HL and HLV network, considering a significance threshold of 100 years. We notice that the results achieved in Gaussian noise (Fig. 5.7) are consistent with real data (Fig. 5.8): as expected, the search sensitivity decreases when considering real data due to increase of false alarm rate in the background distribution. For WNB and SG signals, the comparison between HL and HLV is similar in Gaussian noise and in real data. Instead, GA in the Gaussian case are better recovered by HLV network, while in real data HL is strongly preferred. GA have a morphology similar to blip glitches, hence in real noise it is more difficult to distinguish the injected signals from the spurious artifacts.

The recent developments in cWB and the relaxed Γ regulator result in a general improvement of HLV: Fig. 5.8 shows that the HLV network has a better sensitivity for 12 waveforms over 20. As expected, HL is better for waveform at higher frequencies, where the gap between Virgo and LIGO ASD is larger, and for GA. Comparing 5.8 with the results reported in Fig. 5.2, the gap between HL and HLV has significantly reduced.

Moreover, Fig. 5.9 shows the sky localization precision of the HL and HLV networks for all the simulations performed. As expected, the HLV network provides a significantly more precise sky localization. Fig. 5.9 reports also the percentages of simulations found only by the HL network, only by the HLV and by both, at fixed injected amplitudes and at IFAR>100 years. Only the simulations injected when the three detectors are operating are considering, so we do not consider the higher duty cycle of HL w.r.t. HLV. It is important to understand if a significant fraction of signals is lost without analysing one of the two networks. As expected, the stronger the injections the higher the fraction of simulations that are found by both networks. At lower amplitudes, $\sim 36\%$ of the simulations are found only by HL and $\sim 15\%$ by HLV. At the larger amplitude, $\sim 8\%$ of the simulations are found only by HL and $\sim 4\%$ by HLV.

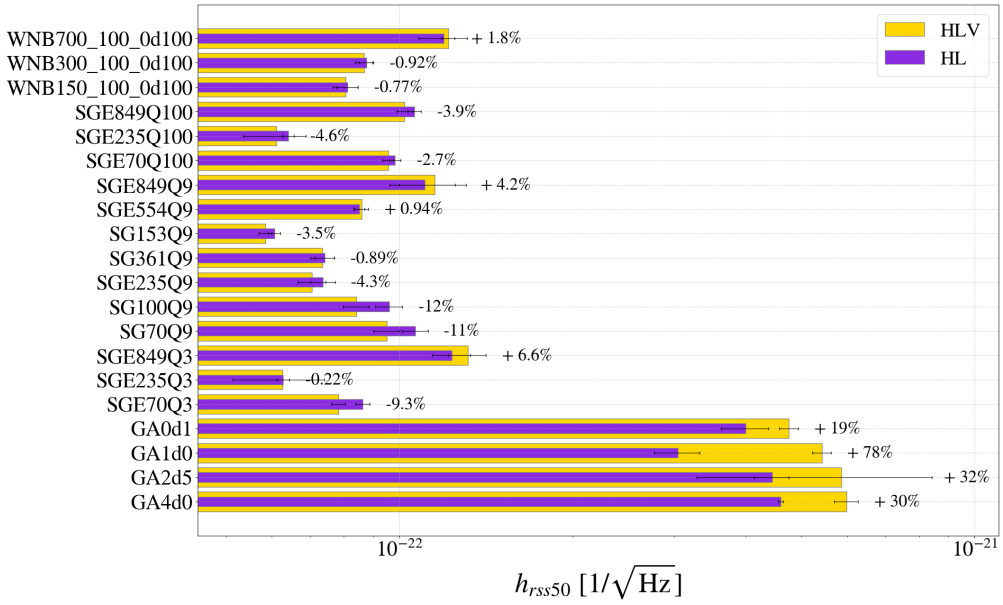

Figure 5.8: Search sensitivity for the HLV (orange) and HL (violet) network in O3b data. The HLV network has a semi-soft gamma regulator ($\Gamma = 0.8$), the best configuration among the three tested in Gaussian noise. The HLV network achieves a higher sensitivity for 12 over 20 waveforms tested. The HL network is better for GA and waveform injected at higher frequencies. A significance threshold of IFAR>100 years is considered.

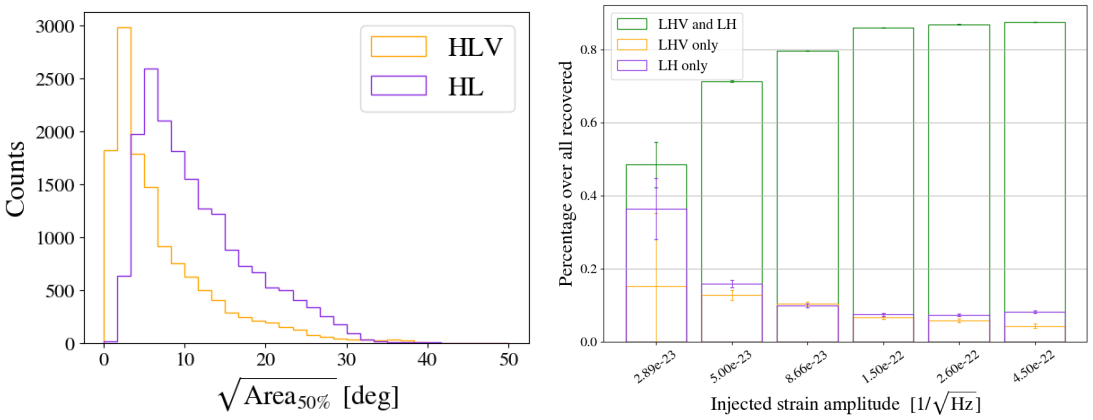

Figure 5.9: (*left*) Search area, measured in terms of sum of sky pixels are with integrated sky probability equal to 50% for all the simulations performed using the HLV (orange) and the HL (violet) network. The three-detector network improves the sky localization of the GW sources. (*right*) Percentages of injections at fixed strain amplitudes recovered only in the HL network (violet), in the HLV (orange) and in both (green). The error bars are simply $1/\sqrt{N}$, where N is the number of events recovered. A significance threshold of IFAR> 100 years is considered.

5.5 Waveform reconstruction with LIGO-Virgo network

Burst searches provide an unmodelled waveform reconstruction of the identified triggers. cWB reconstructs the GW waveforms from the maximization of the likelihood functional. The goodness of the reconstruction strongly depends on the strength of the signals, on the signal morphology and on the position of source in the sky.

Typically, the accuracy of the waveform reconstruction is evaluated by the match between the whitened injected waveform $x_{inj}(t)$ and its whitened reconstruction $x_{rec}(t)$:

$$\text{match}(x_{inj}, x_{rec}) = \frac{(x_{inj}|x_{rec})}{\sqrt{(x_{inj}|x_{inj})}\sqrt{(x_{rec}|x_{rec})}} \tag{5.11}$$

where the waveform product is defined as:

$$(x_A|x_B) = \sum_i^K \int x_{A,i}(t)x_{B,i}(t)dt \tag{5.12}$$

where K is the number of detectors. If the two signals are equal the match is 1.

The reconstructed waveforms are a crucial output of cWB analysis: the waveforms reconstructed with minimal assumptions are compared with the waveforms generated by CBC models using the inferred physical parameters (see Section 2.2.4). The results of such waveform consistency tests have been included in GWs catalog to validate the interpretation of GW events such as CBC. Deviations from PE might be due to the influence of unknown binary parameters, missing physics in the waveform models, deviations from GR, or noise artifacts.

The procedure of the waveform consistency tests is the following [116]: first, the match between cWB reconstruction and the waveform generated with the PE samples that yield the maximum likelihood (*maxL*) is evaluated. This match is referred to as the on-source match. If PE samples were wrong the match would be small. To quantify if there is a significant discrepancy between cWB reconstruction and CBC models the on-source match is compared with a null hypothesis: waveforms generated from PE samples are injected into the data around the time of the event (*off-source injections*) and the matches between the injected waveform and the cWB reconstruction are evaluated. Typically, thousands of injections are performed for each CBC event. Next, the on-source match is compared with the null distribution and a p-value is computed as the fraction of simulations with matches lower than the on-source match. The more the noise in the data (or the weaker the GW signal) the larger the null distribution, and the less is the statistical power of the null rejection.

The cWB waveform consistency test included in the third GW catalog [1] (Table 5 and Figure 12, 13) was performed with the HL network. Here, we investigate the use of the HLV networks for such waveform consistency test.

We focus on the GW event GW200224: this signal is consistent with a GW emission for the merger of a BBH system with component masses $m_1 = 40.0^{+6.7}_{-4.5} M_\odot$ and $m_2 = 32.7^{+4.8}_{-7.2} M_\odot$, originated at a distance of $1.71^{+0.50}_{-0.65}$Gpc, and observed with a network matched-filter SNR of 20 [1]. We inject $\sim$ 3000 waveforms generated from the PE posterior samples in a period of time around the event, considering three cWB configurations: HL network, HLV with $\Gamma = 1$ and HLV with softer regulator ($\Gamma = 0.5$). The median and the 90% symmetric interval for the off-source matches are: for HL $0.917^{+0.026}_{-0.040}$, HLV hard $0.915^{+0.028}_{-0.051}$, HLV soft $0.896^{+0.036}_{-0.044}$ [4].

[4] While doing this investigation, we notice that some values reported in the GW catalog [1] (Table V) are wrong. In particular, for GW200224 the on-source match computed by cWB is 0.93 and the off-source match is $0.92^{+0.03}_{-0.04}$, that has been incorrectly associated to another GW event (GW200311). The correct values are consistent with the results presented here.

Hence, the off-source distribution recovered using the HLV network does not have neither a higher mean value, neither a smaller 90% interval. The HLV network with soft regulator performs slightly worse than HLV with hard regulator. To understand why the HL network is preferred, we report the antenna pattern for the two networks and the comparison between the injected and the recovered source localizations in Fig. 5.10 and Fig. 5.11. The injected signals are localized in a region where the HL antenna pattern is $\sim 0.6 - 0.8$. The hard regulator on HL network forces the reconstruction of the dominant polarization seen by the LIGO detectors, so that the reconstructed sky localizations are in the two regions where the antenna pattern is maximum. As the HL network with hard likelihood regulator is highly effective in reducing the contribution of transient noise, the waveform reconstruction is accurate. The HLV network, as expected, has a more uniform the antenna pattern. A fraction ($\sim 40\%$) of the injections are accurately localized, and the corresponding matches are close to 1. At the same time, the HLV network, especially with softer regulator, reconstructs some injections with significantly biased sky positions. In particular, the signals recovered at $\phi < -120°$ are injected close to glitches in Virgo data. The HLV network with hard regulator does not allow reconstructing an event with sky position where the HL antenna pattern is so low. Instead, the soft regulator admits likelihood solutions in that sky position. The major fraction of the SNR is provided by the Virgo detector but, since the GW signal is superimposed with a glitch, the match is significantly low (< 0.75).

Hence, when the GW simulations are injected close to transient noise, the HLV network provides inaccurate reconstructed waveforms that enlarge significantly the off-source distribution, weakening the strength of the waveform consistency test.

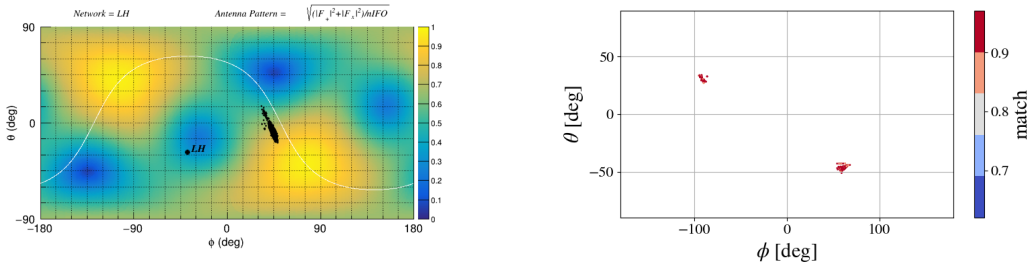

Figure 5.10: (*left*) Antenna pattern of the HL network. The black dots indicate the sky localization of the injected simulations from S200224 PE samples. The white line indicates the equal delay between LIGO detectors. (*right*) recovered sky localizations. The colour bar shows the match (Eq. 5.11). The likelihood regulators force the reconstruction where HL antenna pattern are maximum.

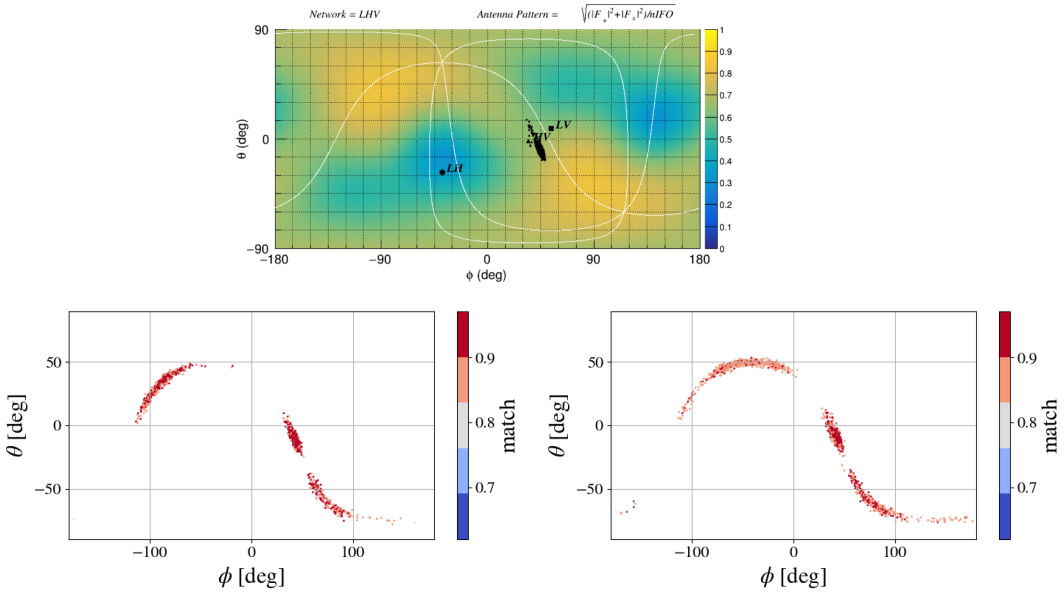

Figure 5.11: (*top*) Antenna pattern of the HLV network. The black dots indicate the sky localization of the injected simulations from S200224 PE samples. The white line indicates the equal delay between HL detectors, HV and LV. (*bottom*) Recovered sky localizations using $\Gamma = 1$ (left) and $\Gamma = 0.5$ (right). The colorbar shows the match (Eq. 5.11). The simulations recovered with a correct sky localization have a high match, while the simulations recovered far from the injected direction ($\phi < -120°$) have the lowest matches.

Chapter 6

An autoencoder neural network integrated into generic gravitational-wave searches to improve the rejection of noise transients

Short-duration disturbances, called glitches, occur with both high SNR and high rate in GW data. Glitches constitute one of the major challenge in the detection of GW events, especially for burst searches which do not assume the knowledge of the GW waveform. This chapter presents an autoencoder neural network integrated into cWB pipeline to improve the rejection of transient noise in GW burst searches.

Among various glitch classes there are blips, single-cycle short-duration signals whose origin is unknown (Section 6.1). The author of this thesis has developed an autoencoder neural network that learns the blip-like morphology as seen by cWB, and build a new statistic to identify and penalize such glitches (Section 6.2).

The inclusion of the autoencoder into cWB analyses improves the noise mitigation, reducing the ranking statistics of low-frequency glitches. This result in an increased search sensitivity: a wide set of morphology are injected into the data from the third observing run to demonstrate that the autoencoder improves the detection efficiencies (Section 6.3). The methodology and the results presented in this chapter have been published in Ref. [129].

6.1 Transient noise in CoherentWaveBurst

Glitches are short-duration transient noise contained in GW detector output that seriously impact GW data analyses (Section 2.1.5). To motivate the work presented in this chapter, it is important to recall here that the median rate of glitches with SNR>6.5 during the third observing run was $\sim 0.3\text{min}^{-1}$ in LIGO Hanford, $\sim 1\text{min}^{-1}$ in LIGO Livingston and 0.8min^{-1} in Virgo [1, 23]. The transient noise increases the false alarm rate of GW searches, and introduces biases when inferring the characteristics of GW sources. The identification and characterization of glitches is crucial: several works have been proposed in the latest years to tackle this problem. In

particular, ML-based methodologies appear as essential to classify glitches into different classes, according to their signature in time domain [54, 55] or in time-frequency evolution [56, 57]. A successful citizen-science project for the supervised classification of GW glitches is Gravity Spy [154], recently joined by GWitchHunter [155]: both couple a neural network together with human classification provided by citizen scientists.

One of the most concerning classes, responsible for a major fraction of unvetoed glitches in GW data is blip glitches [156–159]: typically blips have a short duration, of the order of $\mathcal{O}(10)$ms, and a broad frequency bandwidth $\mathcal{O}(100)$Hz. An example of a blip-like glitch as seen by cWB is shown in Fig 6.1.

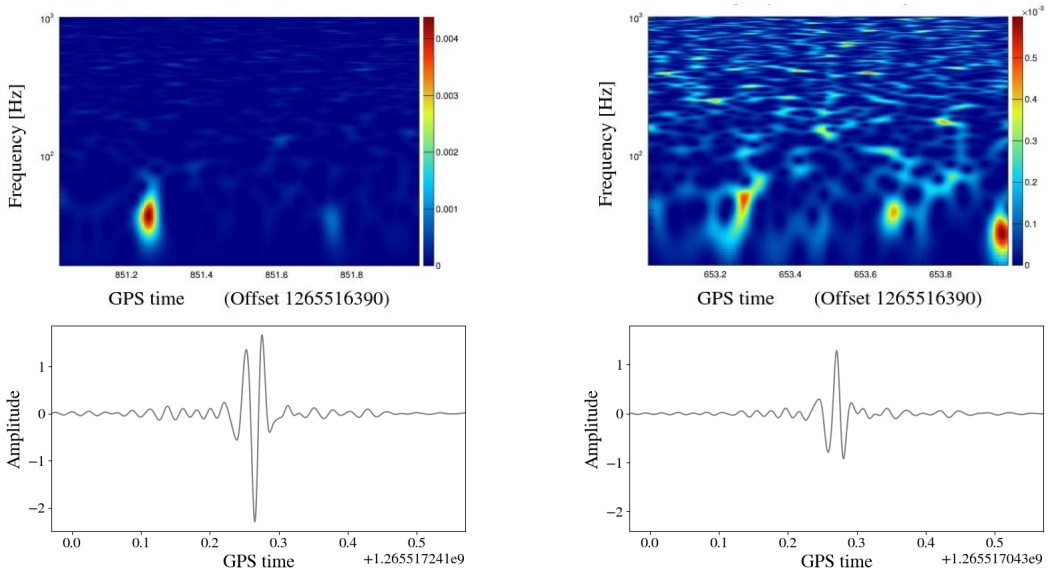

Figure 6.1: Example of a blip-like glitch identified by cWB in LIGO time-shifted data. The top row shows the time-frequency maps, while the bottom row reports the respective time-series. The glitch is reconstructed with SNR= 12 on LIGO Livingston (*left*), while the disturbance is weaker, SNR= 6, in LIGO Hanford (*right*) [129].

During the second observing run there were about 2 blips per hour in LIGO, increasing to 4 per hour in LIGO Livingston during the third observing run [49]. Their origin is still largely unknown: Ref. [156] finds that four subsets are correlated respectively with humidity, laser intensity stabilization, computer errors and power recycling cavity controls, however the established correlations concerns only a minority of the total number of classified blips ($\sim$ 8% in LIGO Hanford and $\sim$ 2% in LIGO Livingston during the first and second observing runs). There is no evidence of correlation with cosmic rays or errors in the data acquisition system [49].

Over the years, the pipelines for the detection of GW events have developed specific techniques to mitigate the impact of blip glitches. For example, the template-based algorithm PyCBC [64] designed a consistency test between the waveform of high-mass BBH mergers and of transient noise, and found that blip glitches have an excess of power at middle to high frequencies, which does not belong to the GW template [160].

cWB mitigates the impact of transient noise leveraging the coherence between different GW detectors. The triggers with network correlation coefficient cc (Eq. 4.33) below a certain threshold are considered non-astrophysical signals. However, as glitches occur with a high rate, there

is a non-negligible probability of having accidental coincidences in multiple detectors between independent glitches. In addition, single-detector transient noise could match part of the noise in the other GW detectors, especially in the case of glitches that have a simple time-frequency evolution as blips, as shown in Fig. 6.1. For these reasons cWB, as well as the other burst algorithms, is strongly affected by glitches, and setting a threshold on the correlation coefficient *cc* is not enough to mitigate transient noise. To reduce the false alarm rate caused by glitches an extra step, referred to as post-processing stage, is necessary. Currently, this is achieved with a decision-tree learning algorithm that automates the signal-noise separation in cWB (described in Section 4.1.6).

This chapter presents a novel approach to target transient noise in cWB, and shows to successfully improve the search sensitivity for all-sky GW burst searches.

6.2 Autoencoder neural network

An autoencoder neural network is an unsupervised learning neural network, i.e. an algorithm composed of several brain-inspired layers that can learn a task without having a labelled dataset. An autoencoder compresses the input data, a time-series or an image, into a lower dimensional space, called *latent space*, and then reconstruct it back to the original dimensional. The compression highlights the presence of characteristics features in the data. This architecture is widely used by the GW community for data denoising [161, 162], GW detection [163–165], and PE [73]. Here, the autoencoder performs an anomaly detection task: the training dataset is made of time-series from a single class of GW glitches. The neural network learns properly that specific morphology, and when it is applied to a morphology with a different signature the reconstruction is not accurate. The accuracy of the reconstruction measures how much a time-series is similar to ones present in the training dataset. The goodness of the autoencoder reconstruction is quantified with the mean square error (MSE) between the input data ($X_{i,\text{input}}$) and the autoencoder reconstruction ($X_{i,\text{ae}}$) as:

$$\text{MSE} = \sum_{i=0}^{n} (X_{i,\text{input}} - X_{i,\text{ae}})^2 \tag{6.1}$$

cWB reconstructs the waveform of the trigger in each detector. The MSE, as the other cWB morphological features Q_a and Q_p [129], is evaluated in each detector, and then it is weighted according to the SNR square of the trigger in each detector.

Next, the main characteristic of the autoencoder neural network are presented: first, Section 6.2.1 introduces neural networks, Section 6.2.2 describes the architecture implemented. Section 6.2.3 shows the input data fed to the algorithm, and Section 6.2.4 discusses the training dataset.

6.2.1 Introduction to neural networks

This section introduces briefly neural networks following Ref. [166]. Neural network are brain-inspired architectures, composed of several basic units referred to as 'neurons'. A neuron receives N input data $x_1, x_2, .., x_N$ with $x \in \mathbb{R}^n$, that can be tabular values, time-series or images. In supervised learning, each input data x as associated a label $y_i \in \mathbb{R}^m$. Each neuron computes the product $h_{W,b} \in \mathbb{R}^m$ as:

$$h_{W,b}(x) = f(W^T x + b) = f\left(\sum_{i=1}^{N} W_i x_i + b\right) \tag{6.2}$$

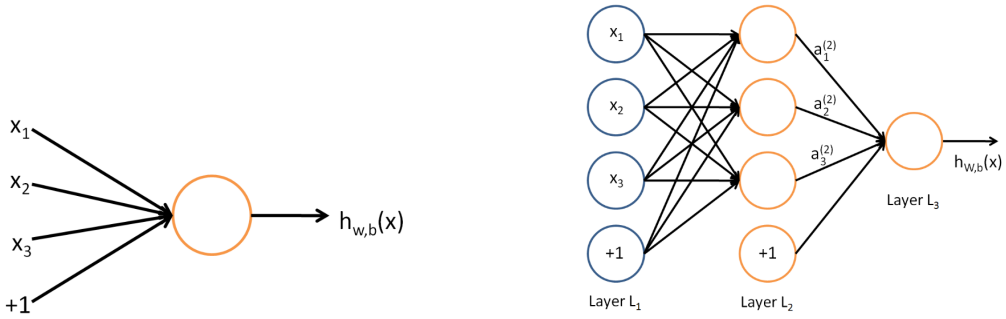

Figure 6.2: (*left*) Sketch of a neuron: the input data is a vector of three elements x_1, x_2, x_3, and the bias term is indicated with +1. The orange circle marks the activation function f. The output of the neuron is $h_{W,b}(x)$. (*right*) Illustration of a fully-connected neural network composed of an input layer L_1 and a hidden layer L_2 with four neurons each. The input data in represented with blue circles. Each x_i is connected to all the neurons in the subsequent layers [166].

where $W \in \mathbb{R}^{m \times n}$ is the weights applied to each input, b is a bias term, typically set to 1, and f is the activation function. There are various possible choices for f: one of the most common is the sigmoid function $f(z) = 1/(1 + e^{-z})$ that scales its input between [0,1]. A sketch of the operation of a single neuron is shown in Fig. 6.2.

A neural network is made of several neurons coupled together. Fig. 6.2 presents an example of a neural network with three layers where each neuron is connected to all the neurons of the following layer. The weights are denoted as $W_{ij}^{(l)}$ where j is the index of unit in the l layer and i is the index of the neuron in the following $l+1$ layer. The output of the i activation function in the l layer is indicated by $a_i^{(l)}$. Hence, for the network sketched in Fig. 6.2, the final output is:

$$h_{W,b}(x) = f(W_{11}^{(2)} a_1^{(2)} + W_{12}^{(2)} a_2^{(2)} + W_{13}^{(2)} a_3^{(2)} + b_1^{(2)}) \tag{6.3}$$

where $a_i^{(2)}$ is:

$$a_i^{(2)} = f(W_{i1}^{(1)} x_1 + W_{i2}^{(1)} x_2 + W_{i3}^{(1)} x_3 + b_1^{(1)}) \tag{6.4}$$

There exist several types of neural networks with different patterns of connectivity between neurons, developed for different tasks. The basic principles of the learning process is described next. During the training, the network tries to learn the function that maps the input x_i into the target y_i. The weights W that provide the output $h_{W,b}$ closer to y_i are found minimizing an error function, or cost function, of the form:

$$J(W, b; x, y) = \frac{1}{2} ||h_{W,b}(x) - y||^2 \tag{6.5}$$

At the beginning of the training, the weights W are assigned randomly, and the network takes the first data x_1, and evaluates the error function $J(W_{\text{random}}, b; x_1, y_1)$. Next, the weights are updated iteratively: the new values are derived by an optimization algorithm such as gradient descent that updates W as:

$$W_{ij}^{(l)} = W_{ij}^{(l)} - \alpha \frac{\partial J(W, b)}{\partial W_{ij}^{(l)}} \tag{6.6}$$

α is called 'learning rate' and it controls how fast the descent is. The same procedure is repeated with all the inputs. Typically, the weights are updated after analysing a ten of training samples, indicated as a 'batch size'. The whole training dataset is processed by the network in the same way several times, called 'epochs', of the order of hundreds to minimize the error function.

Given a certain difference between the network output $h_{W,b}(x_i)$ and y_i, it is not immediate to understand how each neuron has contributed to the final output and how its weights have to be updated. This task is typically performed by a back-propagation algorithm that backward the output error J from the final layer through the initial one. The contribution $\delta_i^{(l)}$ of each neuron i contained in the layer l is computed from the subsequent layer $l+1$ from the derivates of the activation functions as [166]:

$$\delta_i^{(l)} = \left(\sum_{j=1}^{s_{l+1}} W_{ij}^{(l)} \delta_j^{l+1} \right) f'(W_i^{(l)}) \tag{6.7}$$

So, the partial derivatives in Eq. 6.6 are:

$$\frac{\partial J(W,b;x,y)}{\partial W_{ij}^{(l)}} = a_j^{(l)} \delta_i^{(l+1)} \tag{6.8}$$

6.2.2 Architecture

This section describes the architecture of the autoencoder neural network that has been integrated into cWB. In this application, the input data consists of time-series x_i with n data points. The network is made of two components: an encoder f_E that compresses the input into a lower dimensional space, and a decoder g_D that converts the representation back to the original format. The autoencoder output is then $g_D(f_E(x_i))$. The encoder and the decoder are made of several convolutional layers, listed in Table 6.1. At the beginning of the training procedure the weights of the layers are set randomly. During the training procedure, the weights are updated by minimizing the difference between the input x_i and the autoencoder output, as mentioned above. The error function, or loss function, is defined as the MSE between the input and the output:

$$J(x_i) = \frac{1}{n} \sum_{i=1}^{n} ||g_D(f_E(x_i)) - x_i||^2 \tag{6.9}$$

Basically, during the training the network looks for an approximation of the identity function, but as the latent space as a lower dimension with respect to the input data, the algorithm learns a compressed representation of the data which should contain just the key features. In other words, the neural network performs a dimensionality reduction, but with respect to other tools as the Principal Component Analysis [167], it can learn non-linear and complex features.

A critical parameter of the autoencoder network is the dimension of the latent space: the smaller the latent space, the stronger the input compression and the less information is retained by the network. Several compression factors have been tested: we observe that using a higher compression the networks only learns loud blip-like glitches, and it struggles to recognize slightly different morphologies resulting from the combination of glitches and detector noise, and in the end the mitigation of background events is worse.

The network is built using the ML application programming interface Keras [168]. The layers employed in the architecture are:

- **Convolutional**: computes the convolution between the input x and the kernels, or filters. This type of neural network is commonly employed to analyse time-series and images

because it maintains the spatial structure of the data. Each layer has multiple kernels with dimension equal to $(m \times k)$, being m the length of the stride and k the number of kernels applied. The filters in the earlier layers usually learn low-level features, as edges, and the subsequent layers acquire more complex kinds of features, as corners and blobs. The activation function f is a ReLU function [169] that converts its input to positive numbers as $f(z) = \max(0, z)$.

Convolutional layers are one of the most recognized ML algorithms to extrapolate relevant features in time-series and images. In alternative, we have also tested long-short term memory (LSTM) layers [170]. LSTM is a recurrent neural network algorithm in which the output of a neuron i (Eq. 6.2) is affected also by the output of the previous neurons $i-1$ as $h_{i;W,b} = f(W^T(x_i, h_{W,b}(i-1) + b)$. Recurrent neural networks are widely used in time-domain analyses. In our case, we notice that using the LSTM layers in the autoencoder require a much larger computational time, and provided lower reconstruction capabilities, measured in terms of MSE (Eq. 6.1).

- **Max Pooling** (**Up pooling**) is applied after each convolutional layer, and it down-samples (or up-samples) the convolutional output $h_{W,b}$ picking the maximum value over a certain window. Here, a window equal to 2 is set, meaning that the maximum values between two adjacent values is selected. The sequence of convolutional and max pooling layers is a standard in the architecture of convolutional autoencoder, and it is repeated multiple times in the encoder to extract the most relevant features. In the decoder, the convolutional layers are alternated with Max Pooling layer that up-sample the representation repeating the data by 2.

- **Flatten** and **Reshape**: the first simply flatten the inputs from a shape $x^{a,b}$ to $x^{a \times b}$, while the second reshapes a given input into the desired shape.

- **Dense** is made of several basic units, called *neurons*, in which a weight multiplies the input as in $f(W^k x + b)$. In a dense layer, each neuron is fully connected to all the neurons of the previous layers. Here, the dense layer compresses the output of the encoder to the desired latent space dimension.

To train the autoencoder network the epochs, i.e. number of iterations of the entire training dataset, are set to 75. The number of training samples analysed before updating the weights, the batch size, is 16. The network weights are updated by the optimization algorithm ADAM [171]. The total number of network internal parameter is 349513. The training takes about 22 minutes using 16-core AMD opteron 6376 CPU, and the execution time for a single time-series evaluation is about 0.0032s.

6.2.3 Input data

The inputs of the autoencoder neural network are the time-series of cWB triggers. As described in Section 4.1.2 and 4.1.3, cWB removes the noisy frequency lines and whitens the input data. Next, cWB combines the most energetic pixels from different time-frequency resolutions into clusters. The waveform reconstructed by cWB is computed applying the inverse wavelet transform to the multi-resolution cluster for each detector. Thanks to this procedure, the cWB reconstructed waveform is cleaner than the raw GW strain.

Before entering the autoencoder, this time-series are windowed to 416 data-points (corresponding to $\sim 0.2s$ at a sample rate of 2048 Hz) and centred around the absolute maximum

Layer type	Output Shape (length, dimension)
Encoder	
Input	(416,1)
Convolutional	(416,128)
Max Pooling	(208,128)
Convolutional	(208,16)
Max Pooling	(104, 16)
Convolutional	(52, 16)
Flatten	(832)
Dense	(200)
Decoder	
Dense	(832)
Reshape	(52, 16)
Convolutional	(52,16)
Up Pooling	(104,16)
Convolutional	(104,16)
Up Pooling	(208,128)
Convolutional	(208,128)
Up Pooling	(416,128)
Convolutional	(416,1)

Table 6.1: The architecture of the autoencoder neural network proposed in this chapter [129]. Each line represents a layer of the network. The right column reports the output shape of each layer, which is also the input shape for the subsequent one. For example: the input data is a time-series with 416 data points. The first convolutional layer applies a kernel with k=128 filters [129].

value. We have tested different window lengths, from 200 to 800 data points. The choice of 416 represents a favourable compromise: the time-series contains the entire transient noise evolution and the information to be learnt is minimized. Finally, it is suitable when using neural networks to normalize the input data in amplitude between 0 and 1. Two examples of cWB reconstructed waveforms and their autoencoder reconstruction of blip glitches are shown in Fig. 6.3.

6.2.4 Training dataset

The proposed autoencoder is trained with time-series of a single class of transient noise. Here, we focus on blip glitches according to the Gravity Spy classification [154, 159][1]. To collect blip glitches as seen in cWB, first we run cWB analysis in each detector. Then, blip glitches are selected comparing the GPS time of cWB single detector triggers with Gravity Spy blip GPS time. Blip glitches are collected only from the two LIGO detectors, but such noises are present also in Virgo detector [156]. In order to increase the number of samples present in the training dataset, we exploit some techniques of data augmentation: these strategies are common in ML applications which need the largest possible data set. In particular, we include the vertical flip of each time-series, doubling the number of samples contained in the training dataset, and we create additional samples adding Gaussian noise into the retrieved blip time-series. This latter method also improves the capability of the autoencoder to individuate low SNR glitches. The training dataset contains 4608 glitches, occurred during the second half of the third observing run

[1]We select *blip* and *tomte* glitches from Gravity Spy families. The latter class has a time-frequency evolution similar to blip glitches, but is characterized by a larger low-frequency contribution.

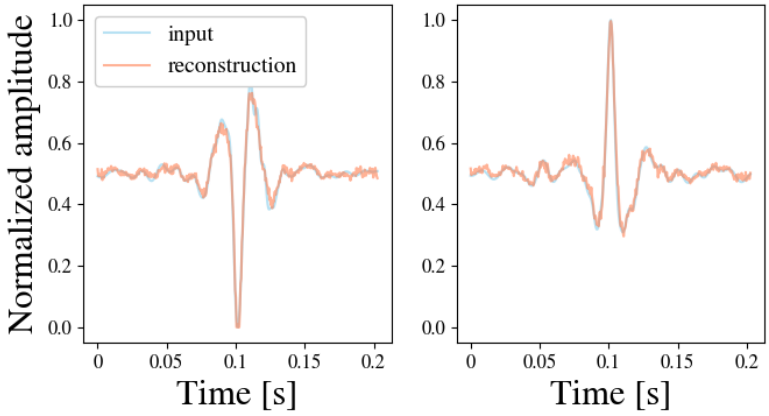

Figure 6.3: Two examples of blip glitches, according to the GravitySpy classification, as seen by cWB in LIGO Hanford. The autoencoder inputs x_i (in blue) are cWB reconstructed waveforms windowed and normalized as described in Section 6.2.3. The autoencoder reconstructions $g_D(f_E(x_i))$ (in orange) accurately matches the input data [129].

(O3b). The validation dataset, which ensure that the neural network is not overfitting, consists of additional 512 samples.

6.3 Results

For each cWB trigger, we compute the MSE (Eq 6.1) between the cWB reconstructed waveform and the corresponding time-series reconstructed by the autoencoder. The MSE is evaluated for each detector, and then the weighted SNR sum among different detectors is stored. MSE values close to zero means that the event is similar to a blip glitch, while higher MSE values suggest that the morphology is different. More detailed comparisons of the autoencoder MSE computed for the background triggers and for injected simulations are reported in Appendix C.

The MSE statistic is included in the list of summary statistics used by the XGBoost algorithm to separate signal from noise (Section 4.1.6). This configuration will be referred in the following as `XGBoost + AE` model, while the configuration without the autoencoder will be labelled simply as `XGBoost`. The cWB configuration and the XGBoost hyper-parameters are the ones used for the all-sky GW burst search presented in Ref. [133], and are identical for the two configurations in order to assess the improvement yield only by the addition of the autoencoder.

The proposed methodology is tested analysing 40 days of coincident data between the LIGO detectors, collected between February and March 2020. Using the time-shifting technique, we accumulate about 380 years of background (Section 4.1.5): 70% is used to train the XGBoost model and the remaining for testing. Similar performances are obtained with different training and testing percentages.

The impact of using the autoencoder on the cWB background distribution is presented in Section 6.3.1. Next, the `XGBoost + AE` and `XGBoost` configurations are tested on a wide set of possible GW signals, and the search sensitivities measured are reported in Section 6.3.2.

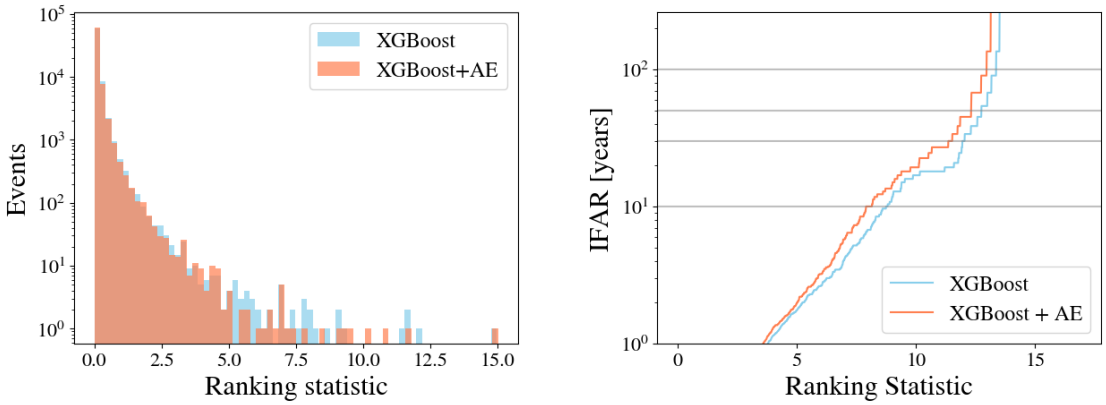

Figure 6.4: (*left*) Distribution of the cWB ranking statistic ρ of the background distribution, obtained with the `XGBoost` model (blue) and the `XGBoost + AE` one (orange). (*right*) IFAR versus the ρ for the background triggers for the two configurations. The `XGBoost + AE` model reduces the number of background triggers at $\rho > 5$. This means that at a fixed IFAR threshold the corresponding ρ is lower. The gray lines indicate the IFAR thresholds at which the search sensitivity is given in Fig. 6.6 and Fig. 6.7 [129].

6.3.1 Mitigation of transient noise

The addition of the autoencoder statistic into the XGBoost post-processing enables a more efficient mitigation of the glitches present in cWB background distribution. This effect appears from Fig. 6.4 and Fig. 6.5 that show the distribution of ranking statistic ρ (Eq. 4.36) for the background triggers. At $\rho > 5$, there are 28 triggers using the `XGBoost + AE` model, while with the `XGBoost` model there are 47 triggers. This improvement can be appreciated also in Fig. 6.4 (right), that shows the IFAR versus the cWB ranking statistic for the two models under consideration. At a fixed ρ, a potential GW signal detected by cWB has a higher IFAR, i.e. a higher significance thanks to the autoencoder, or on the other way around at a certain IFAR threshold the autoencoder enables to detect weaker GW signals.

Fig. 6.5 shows the distribution in frequency of the background distribution, showing that the autoencoder is effective in cleaning the low-frequency region, which is the one populated by blip-like glitches.

6.3.2 Improved search sensitivity

The reduction of the background distribution alone does not guarantee that the search sensitivity has improved. Indeed, a ranking statistic that strongly penalizes all the triggers would result in a clean background distribution, but at the same time, it would reject GW signals. To evaluate the effectiveness of the autoencoder for all-sky short-duration searches, we inject a wide range of possible GW signals in the same period of data, and we compute the associated search sensitivity. The simulation used in this test include ad-hoc signals (sine-Gaussian, Gaussian pulses, and white noise bursts) cosmic strings (Section 3.5) and CBC. For the latter, GW waveforms are computed using `SEOBNRv4PHM` approximant [172] where the BBH coalescences is described by a quasi-circular orbit, including both precession and higher order modes.

The search sensitivity is reported in terms of $h_{rss50\%}$ (defined in Eq. 4.37) and volume

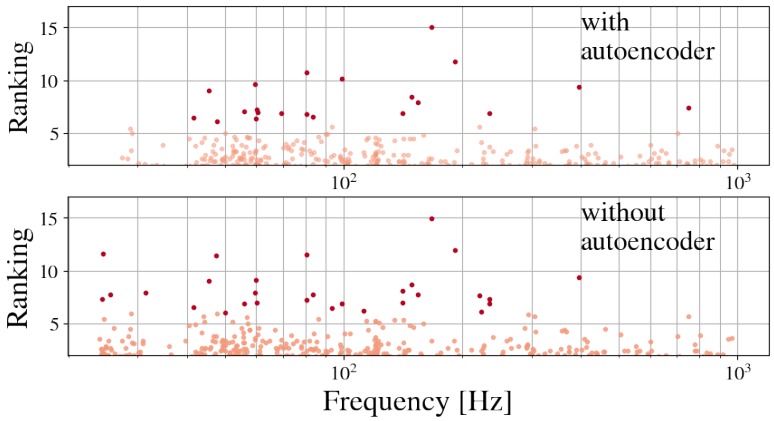

Figure 6.5: cWB ranking statistic ρ versus frequency for the background triggers. Triggers with $\rho > 6$ are highlighted in dark red. The top row refers to the `XGBoost + AE` model which includes the autoencoder network proposed in this chapter, while the bottom row refers to the `XGBoost` model. Thanks to the autoencoder the low-frequency region (below $\sim$ 50Hz) is cleaner.

sensitivity defined as [133, 173]:

$$\mathcal{V} = 4\pi (h_{\rm rss,0} r_0)^3 \int_0^\infty \frac{dh_{\rm rss}}{h_{\rm rss}^4} \epsilon(h_{\rm rss}), \tag{6.10}$$

where $\epsilon(h_{\rm rss})$ is the detection efficiency, computed as the ratio between the signals detected with an IFAR over a certain threshold and the total amount of injections, and $h_{rss,0}$ is a reference amplitude value at a nominal distance r_0. This metric, having a factor h_{rss}^{-4}, highlights the contribution to the sensitivity of the weaker signals.

Fig. 6.6 shows the comparison between the `XGBoost + AE` model and the `XGBoost` model for ad-hoc waveforms and cosmic strings at IFAR >50 years. The sensitivity volume achieved with the inclusion of the autoencoder is higher for all the waveforms considered: the improvement is 33% for cosmic strings, between 22-37% for Gaussian pulse, 8-44% for sine-Gaussian, and for WNB is 1.4 – 4.7%. In addition, we evaluate the performance of the two XGBoost models over different IFAR thresholds to validate that our method is robust (Fig 6.7). The improvements in $h_{rss50\%}$ and volume are consistent also at lower IFAR thresholds, and it is more evident on the waveforms that have a signature similar to blip glitches. At IFAR> 100 years, the search sensitivities achieved by the two models are comparable: this IFAR corresponds to the region of the background distribution with $\rho > 13$ where there is only a single loud glitch. Its ranking statistic ρ is not modified by the inclusion of the autoencoder. Such loud glitches are rare and to accumulate more statistic would require a huge computational cost. Instead, we consider relevant the improvement obtained at lower IFAR, that is the regime in which most of the GW signals detected lies.

For completeness, we report search sensitivity also for simulations of BBH mergers in Fig 6.8. The BBH waveforms are computed using SEOBNRv4PHM model [172], which describes BBH quasi circular orbits, including both precession and higher order modes. The masses follow a power law + peak mass function between 2 $M_\odot$ and 100 $M_\odot$, spins have magnitude randomly distributed between -0.98 and 0.98. The sensitivity volume achieved with the inclusion of the autoencoder is slightly enhanced at all IFAR thresholds, thanks to the cleaner background.

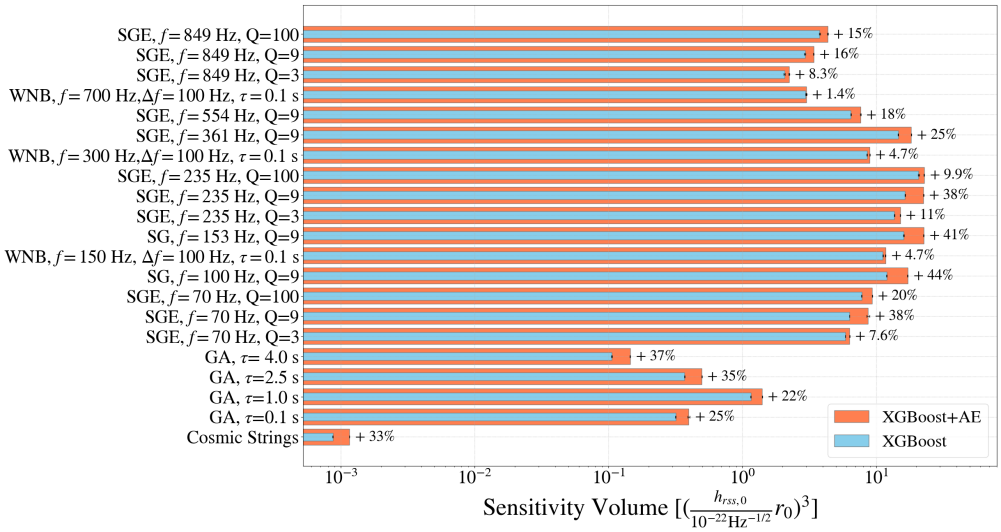

Figure 6.6: Sensitivity volume $\mathcal{V}$ (Eq. 6.10) obtained with cWB with the autoencoder statistic included in the XGBoost model (`XGBoost + AE`) in orange, and without it (`XGBoost`) in blue, at IFAR>50 years. The injected waveforms are: cosmic strings, Gaussian pulses (GA) with duration τ, then ordered according to frequency sine-Gaussian (SG) and SG elliptically polarized (SGE) characterized by central frequency f, and the quality factor Q, and White Noise Burst (WNB) with frequency bandwidth Δf, duration τ and lower frequency bound f. The percentages next to each bar indicate the improvements w.r.t to the volume obtained with the `XGBoost` model [129].

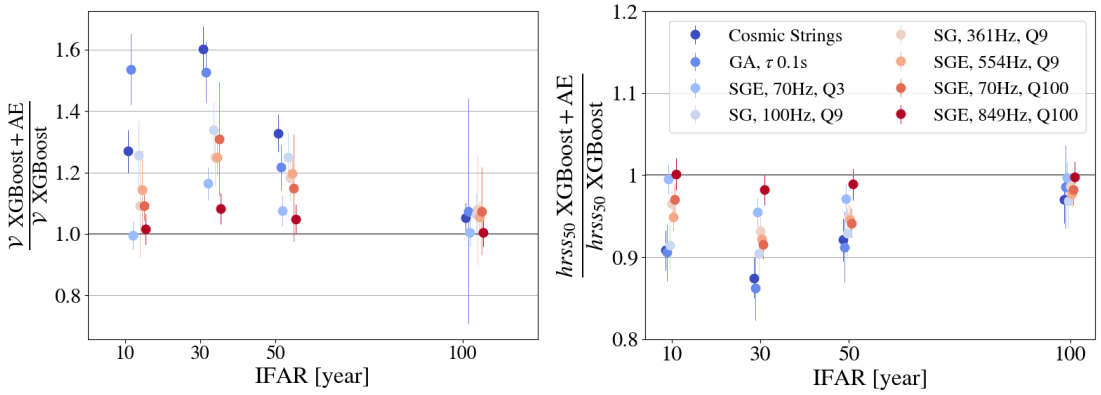

Figure 6.7: Ratio between the sensitivity volume $\mathcal{V}$ (*left*) and the h_{rss50} (*right*) evaluated including the proposed autoencoder (`XGBoost + AE`) and without using it (`XGBoost`) at different IFAR thresholds (10, 30, 50, 100 years). The waveforms injected are: cosmic strings, Gaussian pulses (GA) characterized by the duration τ, sine Gaussian (SG) with central frequency f, and the quality factor Q, and White Noise Burst (WNB) with bandwidth Δf, duration τ and lower frequency bound f. Data points are slightly shifted around the IFAR thresholds for a better visualization [129].

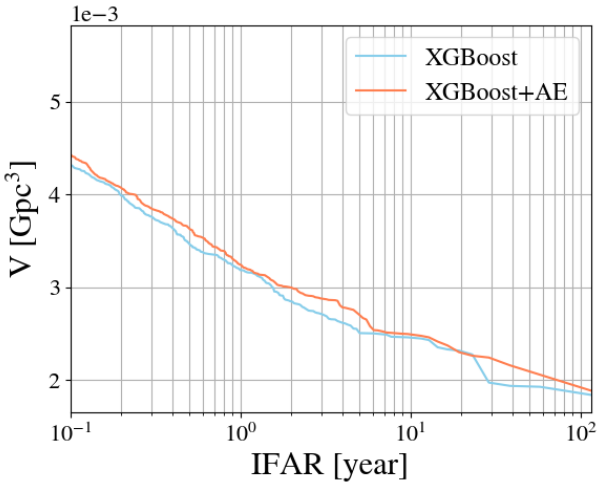

Figure 6.8: Observed volume versus IFAR for BBH mergers simulation. The volume obtained with the inclusion of the autoencoder (orange) is slightly higher w.r.t. the one obtained without the autoencoder (blue) [129].

Chapter 7

Search for hyperbolic encounters between compact objects in the third LIGO-Virgo-KAGRA observing run

Dense stellar environments, as galactic nuclei and globular clusters, are expected to host numerous compact objects, which may encounter on hyperbolic orbits. Such scattering events between compact objects, referred in the following as hyperbolic encounter (HE), are expected to release GW bursts. The GW emission would peak at the periastron, and when the mass of the objects involved is stellar mass, the frequency of the signal is expected to be in the bandwidth of current GW detectors. The detection of such systems would provide crucial information on compact objects distribution.

This chapter presents the search for GWs associated to HE between compact objects in the data of the second half of the third LVK observing run (O3b). The algorithm used is cWB, described in Chapter 4. The search performed is model-informed: cWB identifies generic excess of power, but some information of the signal expected from HE is included when doing the cWB post-processing (Section 4.1.6). To improve the noise rejection, the autoencoder neural network, presented in the previous chapter, is included in the cWB ranking statistic.

No GW events are found in addition to known CBC observations. For the first time, we compute the sensitivity volume achieved for HE, and we discuss the astrophysical implications of our findings.

The structure of this chapter is the following: Section 7.1 presents HE between compact objects, Section 7.2 describes the cWB configuration of the search, and the search results obtained on O3b data. Section 7.3 shows the prospects for the future observing runs of ground-based GW detectors, and Section 7.4 compares our results with the expected rates proposed in literature. This search has been published (see Ref. [174]).

7.1 Hyperbolic encounters between compact objects

As the detectors sensitivities increase, new sources of GWs may be detected. One such source class is HE between compact objects. Section 7.1.1 presents the orbit of such interactions, and

the corresponding GW waveforms in a simple case. Next, Section 7.1.2 overviews more complete GW waveform approximants.

7.1.1 Back of the envelope characterization

This section shows the geometry of a HE interaction under simplistic assumptions following Ref. [96], and derives the estimates of the energy released in the form of GWs and the corresponding GW waveform. Although the calculations are very simplified, it might be useful to understand the basic dynamics of HE.

To study the geometry of an HE system, we introduce a mass M_1 moving in the gravitational potential $\Phi(r)$ generated by a second object M_2 at rest in the origin of the reference frame. The position of the first object is specified by the radius $\mathbf{r}(t)$ and the polar angle $\phi(t)$. With this coordinates, the velocity of the first object is simply:

$$\mathbf{v} = v_r\hat{r} + v_\phi\hat{\phi}, \qquad \text{where} \qquad v_r = \frac{dr}{dt}, v_\phi = r\frac{d\phi}{dt} \tag{7.1}$$

The total energy per unit mass is:

$$E = \frac{1}{2}v^2 + \Phi(r) \tag{7.2}$$

Using the radial coordinates reported above, Eq. 7.2 becomes:

$$E = \frac{1}{2}\left(\frac{dr}{dt}\right)^2 + \frac{1}{2}r^2\left(\frac{d\phi}{dt}\right)^2 + \Phi(r) \tag{7.3}$$

and the angular momentum per unit mass is:

$$L = r^2\frac{d\phi}{dt} \tag{7.4}$$

We perform a change of variable $u = 1/r$ (and $du = -\frac{1}{r^2}dr$). The equation of the motion becomes:

$$\begin{aligned} L &= \frac{1}{u^2}\frac{d\phi}{dt}, \\ \frac{2E}{L} &= \left(\frac{du}{d\phi}\right)^2 + u^2 + 2\frac{\Phi(1/u)}{L^2} = \text{const.} \end{aligned} \tag{7.5}$$

The above equation differentiated w.r.t. u is:

$$\frac{d^2u}{d\phi^2} + u + \frac{1}{L^2}\frac{d\Phi(u)}{du} = 0 \tag{7.6}$$

The classic gravitational force acting on the mass M_1 is $F(r) = -GM_2/r^2$ and it is the gradient of the gravitational potential Φ, so the equation above can be written as:

$$\frac{d^2u}{d\phi^2} + u = \frac{GM_2}{L^2} \tag{7.7}$$

whose general solution is:

$$u(\phi) = C\cos(\phi - \phi_0) + \frac{GM_2}{L^2} \tag{7.8}$$

The constant C depends on the initial conditions and the polar angle ϕ_0 at the periastron distance between the two objects. C can be found differentiating the above equation w.r.t. time t:

$$\frac{du}{dt} = -C\sin(\phi - \phi_0)\frac{d\phi}{dt} \tag{7.9}$$

and going back to the variable r:

$$\frac{dr}{dt} = CL\sin(\phi - \phi_0) \tag{7.10}$$

At the initial condition when M_1 is at infinite distance, dr/dt corresponds to the initial velocity v_0 of M_1, considering the second object at rest and $\phi = 0$. L can be written as $L = bv_0$, where b is the orbital separation at periastron, also referred to as the impact parameter. The constant C is then:

$$C = \frac{1}{b\sin(\phi_0)} \tag{7.11}$$

The equation of the orbit from Eq. 7.10 is then [175]:

$$r = \frac{b\sin(\phi_0)}{\cos(\phi - \phi_0) - \cos(\phi_0)} \tag{7.12}$$

Knowing the initial conditions b and ϕ_0, the equation above determine the position of the moving object. From the orbit equation, it is possible to estimate the GW waveform generated during the interactions.

The amplitude of the GW waveform in the quadruple approximation (see Eq. 1.10) is given by:

$$h^{ij}(t, d) = \frac{2G}{dc^4}\ddot{Q}^{ij} \tag{7.13}$$

where d is the distance between the GW source and the observer, and Q^{ij} is the quadrupole mass tensor (Eq. 1.11):

$$Q_{ij} = \sum_a m_a(3x_a^i x_a^j - \delta_{ij}r_a^2) \tag{7.14}$$

where r_a is the magnitude of the vector radius of the a-th particle. Using Eq. 7.12, the expected strain amplitude $h \simeq (h_{11}^2 + h_{22}^2 + h_{12}^2)^{1/2}$ [96] is:

$$h = \frac{2G}{dc^4}\mu v_0^2 G(\phi, \phi_0) \tag{7.15}$$

where μ is the reduced mass of the system, and $G(\phi, \phi_0)$ is a function of the polar angle ϕ and the initial condition ϕ_0 [1] [96]. The energy emitted in form of GWs per unit time is:

$$\frac{dE}{dt} = -\frac{G\langle Q_{ij}^{(3)} Q^{(3)ij}\rangle}{45c^5} \tag{7.17}$$

[1] The definition of $G(\phi, \phi_0)$ in Eq. 7.15 is:

$$G(\phi, \phi_0) = \csc^2\phi_0[2[59\cos 2(\phi_0 - \phi) - \cos\phi(54\cos(2\phi_0) + 101)]\cos^2\phi_0 \\ -9\cos(3\phi - 4\phi_0) - 9\cos(3\phi - 2\phi_0) + 95\cos 2\phi_0 + 9\cos 4\phi_0 - \sin\phi[101\sin 2\phi_0 + 27\sin 4\phi_0] + 106]^{-1/2} \tag{7.16}$$

where Q_{ij} is differentiated w.r.t. time, and the brackets indicate the scalar product. Integrating in time, considering $M_1 = M_2$ the total energy emitted is of the form:

$$\Delta E = \int_0^\infty \left| \frac{dE}{dt} \right| dt = \frac{4 v_0^5 r_s M_1}{45 c^3} F(b, v_0) \tag{7.18}$$

where r_s is the Schwarzschild radius of the mass, and $F(b, v_0)$ a function of the initial conditions [2][96]. As expected, the energy released in GW increases with the masses of the objects involved. ΔE depends on the configuration and the kinematics of the system, and it increases with the initial velocity v_0 and the closer the interaction is, so for lower b.

7.1.2 Waveform approximants

The previous section introduces HE interactions, and derives the expected GW waveform under the assumption that the periastron distance between the objects is much larger than their Schwarzschild radius (Eq. 7.15). The characterization of the GW emission originated from HE under more general assumptions is an active area of research. There exist several approaches to model this interaction such as the post-Newtonian (PN) approximation [176, 177], post-Minkowskian expansion [178, 179], numerical relativity [180, 181] and the effective one body formalism [182–184]. Recently, it has been proposed an interpretation of the high-mass GW event GW190521 [1] as two BHs in a hyperbolic orbit leading to a direct capture [75]. In the following sections, we perform HE simulations to configure the search and to evaluate the sensitivity volume towards this source.

The waveform model considered is a 3 PN-accurate approximant [97]. PN waveforms assume a weak-field and are no longer valid when the BHs are too close and/or experience a GW capture. Ref. [177] indicates that the PN waveforms are accurate until the orbital separation b, between the involved objects is above $10GM/c^2$. In addition, the orbital eccentricity should not be lower than 1.15 when the impact parameter is $60GM/c^2$. In this study, this condition has been slightly relaxed, and the lower bound is eccentricity of 1.05. Even if the waveform might have some inaccuracy, it will not affect the search presented in this chapter because it is not a template-based search, but a burst analysis which do not make strong assumption on the morphology of the signal.

The parameter space covered by the injection set is the following: HE waveforms have component mass uniformly distributed in six bins ([2, 5], [5, 20], [20, 40], [40, 60], [60, 80], [80,100] $M_\odot$), impact parameter b is uniform in [60, 100]GM/c^2, and the orbital eccentricity is uniform in [1.05, 1.6]. For each mass bin, about 20 thousand injections are performed, resulting in 120 thousands injections overall.

These ranges are chosen to be as broad as possible, providing GW waveforms with a major fraction of energy in the frequency range of current GW detectors. Fig. 7.1 shows the relationship between the masses of the compact objects, the impact parameter and the peak frequency of the GW emission. In the frequency domain, the HE signal is broadband. The peak frequencies are in the lower boundary of current GW detectors for the most massive systems considered, and go up to $\sim$ 450Hz for NS masses [177]. In the time domain, HE from heavier masses and larger impact parameters have longer signals. The mass ranges considered in this study are expected to produce GW signals with a duration of less than a second.

[2]The function $F(b, v_0)$ is defined as:

$$\begin{aligned} F(b, v_0) = [720 b \tan^2\phi_0 \sin^4\phi_0]^{-1} \times (&268\phi_0 + 2328\phi_0 \cos 2\phi_0 \\ &+144\phi_0 \cos 4\phi_0 - 1948 \sin 2\phi_0 - 301 \sin 4\phi_0) \end{aligned} \tag{7.19}$$

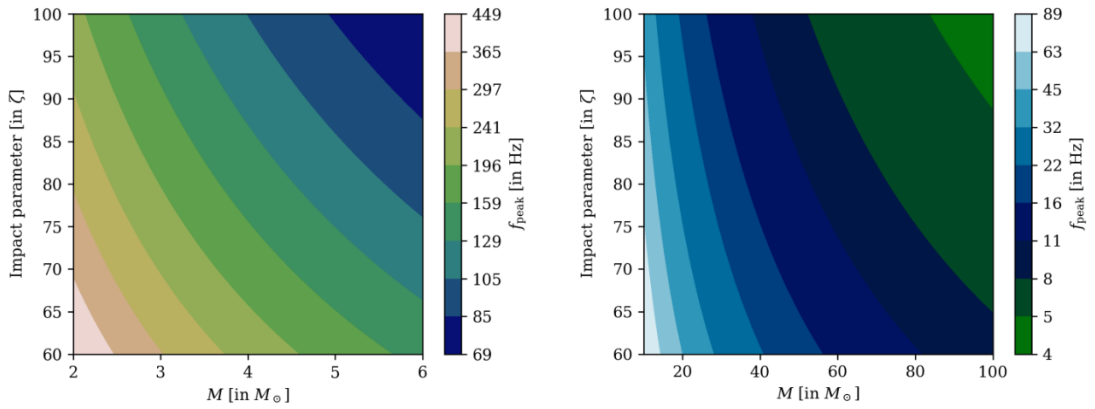

Figure 7.1: Contour plot of the peak frequency of the HE GW waveforms versus the total mass of the objects involved and the impact parameter, from Ref. [97]. The impact parameter is indicated in unit of $\zeta = GM/c^2$. The plot on the left refers to HE between NSs, while the plot of the right is for BHs. Here, the compact objects have equal masses, and the orbital eccentricity is fixed at 1.15.

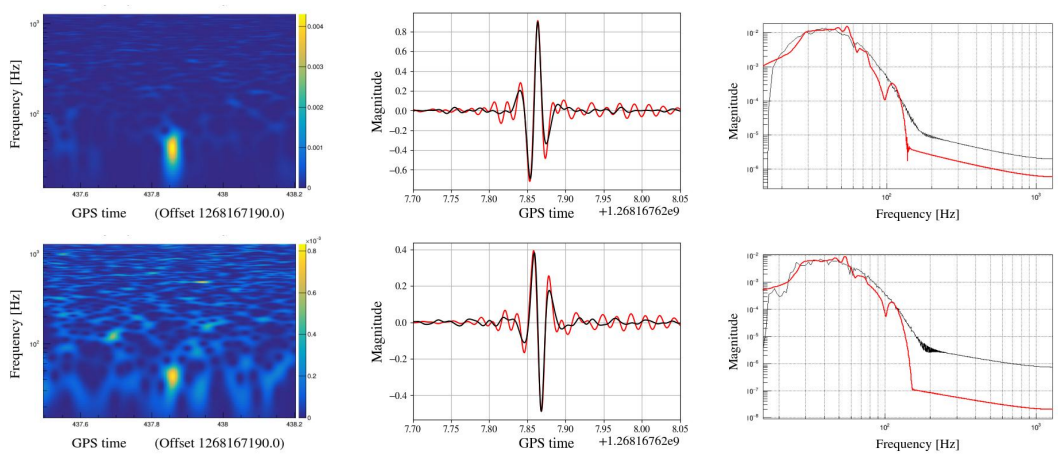

Figure 7.2: Example of simulated HE GW waveform injected in O3b data and reconstructed by cWB. The first row shows the signal in LIGO Livingston, and the second in LIGO Hanford. The first column reports the time-frequency spectrograms, the second and third columns show the injected waveform (black) and the corresponding cWB reconstruction (red) in time domain and in frequency domain. The HE signal is injected at a distance of 182 Mpc with masses $m_1 = 26.7M_\odot$ and $m_2 = 36.4M_\odot$, impact parameter 59.5 GM/c^2, and eccentricity 1.1. The simulation is recovered by cWB with network SNR of 14 [174].

Fig. 7.2 shows an example of an HE GW waveform injected into O3b data and recovered by cWB. The signal appears in the time-frequency representation as an excess of energy at around 40Hz. The waveform is accurately reconstructed by cWB both in time and in frequency domain.

7.2 Search in the third LIGO-Virgo-KAGRA observing run

This section presents the search for HE between compact objects in the second half of the third LVK observing run using the cWB pipeline. First, Section 7.2.1 describes the model-informed configuration developed specifically for this search. The results are presented in Section 7.2.2. No GW event associated with HE has been identified. Section 7.2.3 reports the sensitivity volume achieved, and the corresponding upper limits on the event rate. The properties of the HE simulations recovered by cWB are overviewed in Section 7.2.4.

7.2.1 A model-informed search

The search for HE is performed with the burst algorithm cWB, extensively described in the fourth chapter. As presented in Section 4.1.6, cWB adopts a decision tree learning algorithm, called XGBoost, to improve the separation between astrophysical GW signals and glitches. For this search, XGBoost is trained with a subset ($\sim 25\%$) of the HE injections performed, described in Section 7.1.2. The resulting configuration is called a model-informed search: it can be considered a middle way between a match filtering search, that looks for GW with a morphology similar to the waveforms contained in extensive template banks, and an unmodelled search. A model-informed search targets a specific GW source, but it is still sensitive to GW waveform that are not present in the training dataset. This configuration is particularly suited when the model waveforms are not precisely known, or they cover only a certain parameter space. Examples of model-informed search performed with cWB pipeline targeting BBH mergers and eccentric BBH are presented in Ref. [132, 185].

The XGBoost model is built using 10 cWB summary statistics: total energy over all time-frequency resolutions, correlation coefficient cc (Eq. 4.33), quality of the event reconstruction defined as $X = E_n/n$ with E_n noise energy (Eq. 4.33) and n the number of wavelets used, square of SNR over likelihood, incoherent energy over likelihood, root-mean-square noise for selected pixel over all layers, central frequency, effective correlated SNR, shape parameter Q_p [129], and the similarity score to blip glitches computed by the autoencoder neural network discussed in the previous chapter.

Figure 7.3 shows the detection efficiency versus IFAR for the HE model-informed search proposed here, and the all-sky short-duration search performed with ML-enhanced cWB [133]. The main differences between the two are the training data set used to build the XGBoost model (HE waveforms for the first, and white noise burst simulations for the second) and the cWB summary statistics used to build the model (the HE search includes also the central frequency and the autoencoder statistics). Moreover, the model-informed search does not apply the final correction to the ranking statistics described in Ref. [133] (appendix A). The latter is used to remove high SNR glitches, and it is based on two hand-tuned parameters. The choice of not using here this correction is part of the effort of cWB to investigate the implication of this penalization, and find a configuration with fewer hand-tuned corrections in preparation for the fourth observing run.

The detection efficiency improvement is evident in the three different mass bins presented in the figure, at different IFAR. In particular, the efficiency at IFAR$>$ 10 years using the HE model-informed search and the generic all-sky one [133] increases from 9% to 15% for component masses in the range [2, 5] $M_\odot$, from 11% to 18% in [5, 20] $M_\odot$, from 17% to 23% in [20, 40] $M_\odot$, from 18% to 24% in [40, 60] $M_\odot$, from 16% to 22% in [60, 80] $M_\odot$ and from 14% to 20% in [80, 100] $M_\odot$, respectively. At larger IFAR (>100 years) the two configurations have similar performance: this region is affected by loud glitches and the general gain achieved by the model-

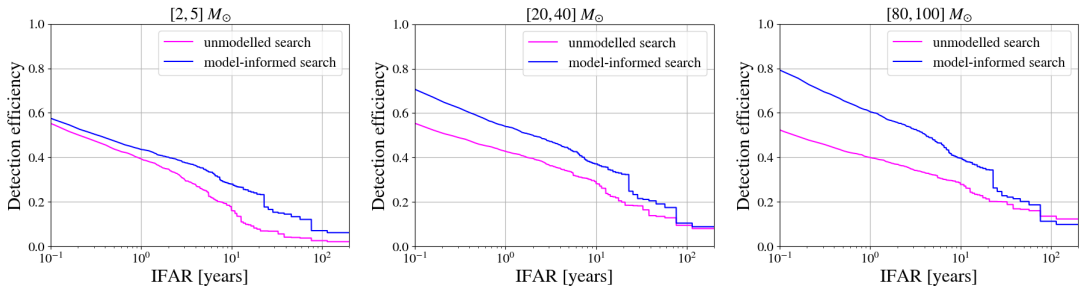

Figure 7.3: Detection efficiency versus IFAR for the model-informed search proposed in this section (pink) and the all-sky short-duration search (blue) [133] in three different mass bins ($[2,5]M_\odot$ left, $[20,40]M_\odot$ middle, $[80,100]M_\odot$ right). The model-informed search has a larger detection efficiency in the different mass bins and at different IFAR.

informed search is balanced by the removal of the ranking penalization correction mentioned above.

Before looking for GWs associated with HE, the cWB accuracy in recovering this type of signals is evaluated to ensure that cWB is a suitable algorithm for the proposed search. Fig. 7.4 shows the goodness of the cWB waveform reconstruction of HE signals, measured by the match defined in Eq. 5.11, versus the signal SNR. As expected, the accuracy of the reconstruction increases for higher SNR signals. The mean values of the match distributions are 0.938 ± 0.027 for HE with low masses ([2, 5] $M_\odot$), 0.958 ± 0.022 for intermediate masses ([20, 40] $M_\odot$) and 0.966 ± 0.016 for higher masses ([80, 100] $M_\odot$). Such results indicate that cWB reconstruction is robust, and the waveforms are reconstructed with high fidelity. The presence of eccentricity does not affect the cWB waveform reconstruction.

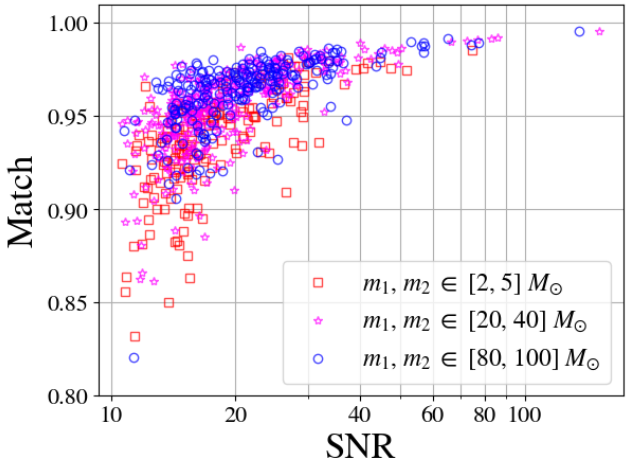

Figure 7.4: Match (Eq. 5.11) versus SNR of the injected waveforms for HE events detected with IFAR $>$ 10 years. HE signals have component masses between [2, 5] $M_\odot$ (red), [20, 40] $M_\odot$ (pink), [80, 100] $M_\odot$ (blue). The match distributions are peaked above 0.9 meaning that cWB reconstruction is accurate [174].

7.2.2 Search results

This section presents the results of the model-informed search described above in the O3b data, that started on November 1, 2019 and ended on March 27, 2020. We analyse the data from the two LIGO detectors. The addition of the Virgo detector, as discussed in the Chapter 5, does not increase the search sensitivity to single-cycle waveforms similar to Gaussian pulses (Fig. 5.8) due to Virgo lower sensitivity and its different alignment w.r.t. the LIGO detectors.

The coincident time between the two LIGO detectors during O3b is 95 days. Using the time-shift technique (Section 4.1.5), we accumulate around 305 years of background: 25% of the background triggers are used to train the XGBoost model, and the remainings are employed to assess the significance of the recovered triggers.

The results of the search are shown in Fig. 7.5. No significant event has been identified in addition to the known CBC observations [1]. The most significant trigger has a significance of $\sim$ 20 years and SNR of 8.5 and 8.6 in LIGO Livingston and LIGO Hanford, respectively. The peak frequency is at 89Hz, bandwidth of 37Hz and duration of 0.012s. This trigger is reported in the third LVK catalog [1] as the CBC event GW191222, observed with a template-based search at IFAR>1100 years and a distance of 3.0 ± 1.7 Gpc. The BHs involved in this event have component masses estimated at $m_1 = 45.1^{+10.9}_{-8.0} M_\odot$ and $m_2 = 34.7^{+9.3}_{-10.5} M_\odot$, being one of the most massive event observed during O3b. Hence, it has a short duration which can explain why it results the most significant trigger found by the HE search. There is no significant evidence of deviation w.r.t. the CBC template: the waveform consistency test [116] that compares the cWB unmodelled reconstruction with the waveform generated with the CBC model indicates that they are in agreement.

The fact that the model-informed search does not find significant CBC events is not surprising: the search proposed here is tuned towards HE signals that have a time-frequency evolution different from typical CBC signals.

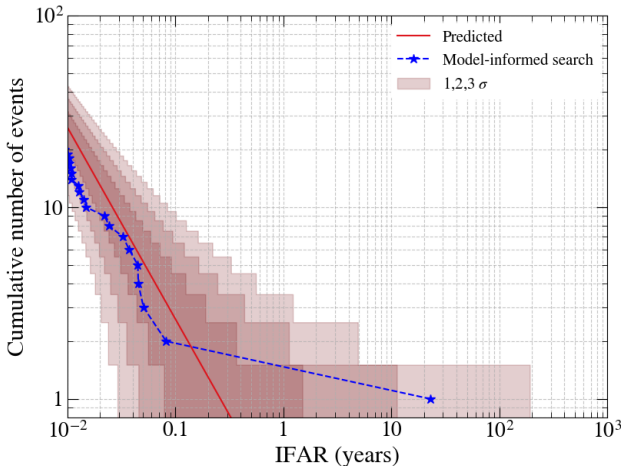

Figure 7.5: Cumulative number of events (blue stars) found by the model-informed search on O3b data versus their IFAR. The red solid line shows the expected mean value of the background distribution, 1σ, 2σ and 3σ Poisson uncertainty intervals are indicated with shaded region. There are no significant outliers, i.e. events with IFAR above the 3σ background distribution [174].

Mass range $[M_\odot]$	$[2,5]$	$[5,20]$	$[20,40]$	$[40,60]$	$[60,80]$	$[80,100]$
Volume $[10^5\mathrm{Mpc}^3\mathrm{year}]$	0.059±0.021	1.71±0.61	3.9±1.4	2.58±0.93	1.32±0.47	0.67±0.24
Distance [Mpc year]	11.2±1.3	34.4 ±4.1	45.1±5.4	39.5±4.7	31.6±3.8	25.2±3.0
Rate upper limit $[\mathrm{Mpc}^{-3}\mathrm{Myear}^{-1}]$	392±61	13.4±2.1	5.98±0.94	8.9±1.4	17.5±2.7	34.3±5.4

Table 7.1: Sensitive volume, distance and event rate for HE simulations recovered with an IFAR $>$ 10 years in each mass range. The largest volume is achieved for objects with masses in [20,40]$M_\odot$. The main contribution to the errors is given by the uncertainty in the GW detector calibration [174].

7.2.3 Sensitivity volume and rates upper limits

The results of the search presented in Fig. 7.5 do not show evidence for a significant GW event. In this section, the observable sensitivity spacetime volume $\langle VT\rangle$ achieved by the HE model-informed search is evaluated. $\langle VT\rangle$ indicates the portion of the Universe in which the proposed search would have found a HE with a certain significance, if any. To compute $\langle VT\rangle$, HE GW waveforms are uniformly injected in a volume V_0 defined up to a maximum redshift $z_{\max}$ [186]:

$$V_0 = \int_0^{z_{\max}} \frac{\mathrm{d}Vc}{\mathrm{d}z}\frac{1}{1+z}\mathrm{d}z \tag{7.20}$$

where $\frac{\mathrm{d}Vc}{\mathrm{d}z}$ is the differential co-moving volume and the term $\frac{1}{1+z}$ accounts for the Universe expansion. The maximum redshift $z_{\max}$ is selected so that the detection efficiency becomes negligible: $z_{\max}$=0.8 for lighter HE (masses between [2, 5] $M_\odot$), and $z_{\max}$=0.1 for the other ranges. The average sensitivity spacetime volume is computed from V_0 and the algorithm recovering efficiency as:

$$\langle VT\rangle = V_0\frac{N_{\mathrm{det}}}{N_{\mathrm{inj}}}T \tag{7.21}$$

where T the observation time, N_{inj} is the number of signals injected, N_{det} the number of events identified by cWB with a certain significance. A significance of IFAR$>$10 years is adopted, alternative choices of IFAR thresholds are discussed in Appendix D.

The uncertainty of the volume is due both the statistical errors and the GW data calibration errors. The first can be estimated from the binomial statistics as $dV_{stat} = \frac{1}{\sqrt{N_{det}}}\sigma(N_{det}/N_{inj})$ [186]. The statistical errors are $< 2\%$ in each mass range. The major contribution to the errors is related to the GW calibration error which in amplitude is $< 12\%$ [61]. The corresponding error on the volume is $< 36\%$.

Fig. 7.6 presents the sensitive volume into the different mass ranges. $\langle VT\rangle$ is maximum for HE with component masses in [20, 40] $M_\odot$ ($3.9\pm1.4\times10^5\mathrm{Mpc}^3\mathrm{year}$). The lowest volume is achieved for low mass systems: in this regime the GW energy released during the encounters is less, so only events that occur closer can be detected. At high masses, the frequency of the expected GW signals decreases, and a major fraction of the GW energy is in the spectrum where the detectors are less sensitive. From $\langle VT\rangle$ the sensitive distance D is evaluated, which basically corresponds to the radius of the observable volume. The maximum distance is for HE with component masses in [20, 40] $M_\odot$ at 45 ± 5.4 Mpc. The values computed in each mass range are reported in Tab. 7.1

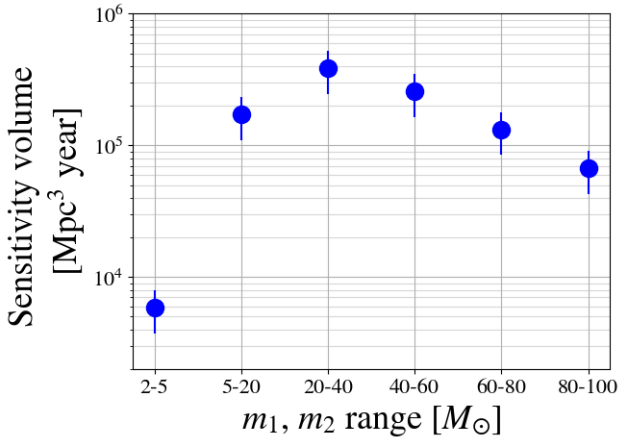

Figure 7.6: Sensitivity spacetime volume $\langle VT \rangle$ for different mass range considering HE simulations recovered with a significance larger than 10 years. The largest volume is achieved for compact objects with masses between 20 and 40 $M_\odot$ [174].

To validate the sensitivity measured, we compare the distance estimated with the values reported in Ref. [97], which injects the same waveform models on simulated Gaussian noise from Advanced LIGO PSD, and considers a simulation to be detected if the optimal SNR is above 8. With this method, GW signal from HE between two NSs and two BHs, optimally placed, are visible up to ~ 20 and ~ 170 Mpc respectively. These values are a factor of $\sim 2-4$ higher than our sensitivity distances, reported in Tab. 7.1. These differences can be explained by the fact that our search is based on real O3b data that contains non-Gaussian noise, and for which the detectors' PSD are lower than the one considered in Ref. [97]. In addition, the distance prospects are computed applying a detection threshold on the optimal SNR that, as discussed in Section 3.1, has a better performance than a burst search.

From the evaluation of the sensitive volume, we compute the upper limit rates for GW signals from HE, following Ref. [187]. The probability of detecting N events over an observing time T is given by the Poisson distribution for a process with rate λ and probability of successfully detecting a given event ϵ:

$$P(N|\epsilon\lambda) = \frac{(\epsilon\lambda)^N}{N!} \mathrm{e}^{-(\epsilon\lambda)} \tag{7.22}$$

The a priori probability of detecting n or fewer events is $\sum_{N=0}^{n} P(N|\epsilon\lambda)$. To set a rate upper limit, we select a confidence level $\alpha \in (0,1)$, so that

$$\sum_{N=0}^{n} P(N|\epsilon\lambda) = 1-\alpha \tag{7.23}$$

The 90% confidence level in case of a null detection ($n=0$) is simply:

$$\mathrm{e}^{-(\epsilon\lambda_{90\%})} = 1-0.9 \tag{7.24}$$

and so the rate upper limit is given by:

$$\lambda_{90\%} = \frac{-\ln(1-0.9)}{\epsilon} \tag{7.25}$$

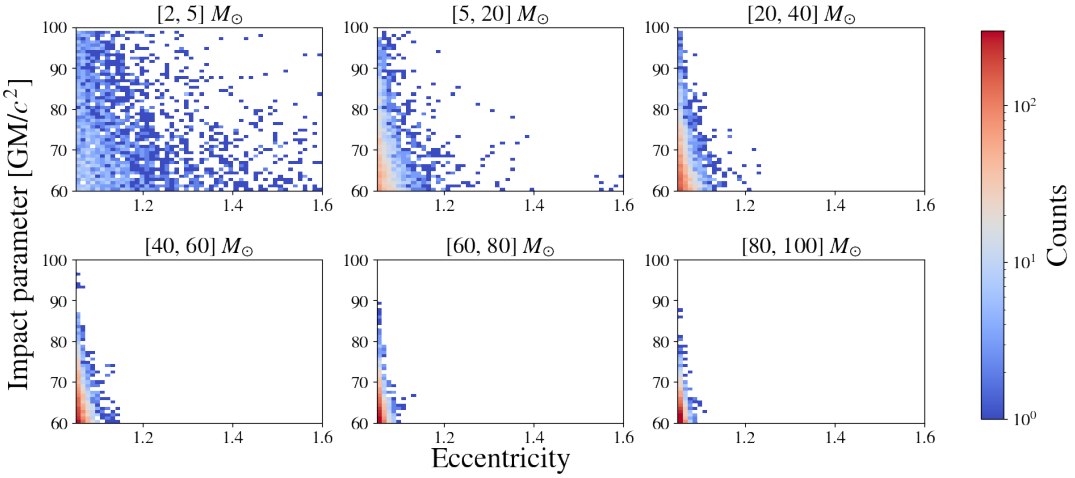

Figure 7.7: Orbital eccentricity versus impact parameter b for the HE injections recovered by cWB with IFAR> 10 years. Each plot refers to a specific mass range, indicated in the title, increasing from left to right. The injections are uniformly distributed in the parameter space represented, but strong selection effects are present, especially for massive systems [174].

In our case ϵ is the search sensitivity $\langle VT \rangle$. The error on the rate is estimated propagating the uncertainty on the volume. The most stringent constrain on the rate is $5.98 \pm 0.94 \mathrm{Mpc}^{-3}\mathrm{Myear}^{-1}$, achieved for HE with masses in [20, 40] $M_\odot$.

7.2.4 Properties of the hyperbolic encounter simulations recovered

This section shows the properties of the HE simulations recovered to discuss the capabilities of cWB and potential selection biases that might affect this source. As described in Section 7.1.2, the impact parameter and the eccentricity of the injected signals are uniformly distributed in [60, 100] GM/c^2 and [1.05, 1.6], respectively. Fig. 7.7 reports the distribution of these two parameters for the simulations recovered by cWB with an IFAR $>$ 10 years in each mass range. Only the simulations that lie on a limited region of this parameter space covered by the injection set are covered. In particular, when massive objects are involved only the events with low impact parameter and low eccentricity are recovered: indeed, the higher the impact parameter and the eccentricity, the lower the peak frequency. For massive systems, the HE signal frequency lies close to the low-frequency limit of current detectors. Such selection effects would have to be taken in consideration to infer the HE source population properties, especially in the case of a detection.

When looking for GW signals it is also important to assess the capability of the search algorithm to localize the source in the sky. This is important especially in the cases where an electromagnetic counterpart is expected to be associated with the GW events. In order to make a multi-messenger observation, the sky localizations areas of the two emissions (GWs and electromagnetic) should be confined and overlapping. GW events originated from the coalescence or the close encounter of BHs are not expected to be associated with electromagnetic counterpart, while this is the case when NSs are involved. Section 7.4 briefly presents the mechanism that is expected to produce an electromagnetic emission during HE between NS. Here, we report the cWB 90% credible area for HE with component masses in [2, 5]$M_\odot$ in Fig. 7.8. About

40% of the recovered simulations have a search area of $\sim 1000\,\mathrm{deg}^2$: such localization would make problematic the association with an electromagnetic emission. The localization improve significantly including more GW detectors in the analysis, as presented in the next section.

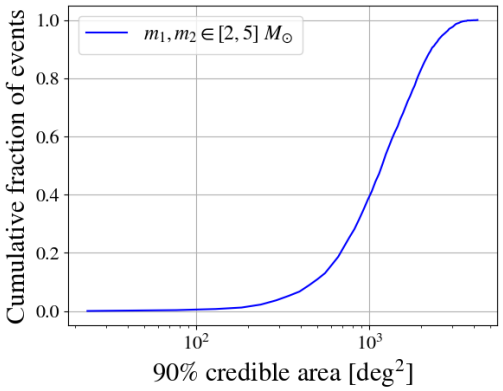

Figure 7.8: Cumulative fraction of simulations recovered with IFAR>10 years versus 90% credible area, for HE with component masses in [2, 5]$M_\odot$ in O3b data [174].

7.3 Prospects for future LIGO-Virgo-KAGRA observing runs

Ground-based GW detectors are continuously improving their sensitivities, hence the probability of detecting GW from new sources become more and more probable. This section presents the prospects of the search sensitivity expected for the next LVK observing runs (O4 and O5). Two possible detectors networks are taken into consideration: HLV (LIGO and Virgo detectors) for O4, and the network HLVK, which includes also the KAGRA detector, for O5 [3].

We inject HE between BHs with masses between [20, 40] $M_\odot$ as it is the range that provides the maximum sensitivity volume (Fig. 7.6). The volume V_0 in which the waveforms are injected is increased to account for the higher detector sensitivity. The simulated signals are added to Gaussian noise to represent the noise floor for future GW detectors, considering the detectors PSD presented in Ref. [37]. As the noise is Gaussian, we analyse the O4 and O5 data with cWB without applying the XGBoost signal-noise separation (Section 4.1.6). It is important to understand how the efficiency of cWB in this configuration differs to the one employed on real case scenario, in order to validate the volume computed for the prospects. To do so, we perform a set of injections on O3b PSD Gaussian noise and compare the results which the one reported in Table 7.1. The sensitivity on Gaussian data at IFAR >10 years is similar to the one achieved in real detector noise: at this significance threshold the XGBoost algorithm is very effective in removing background triggers. The differences between Gaussian noise and real data arise at higher IFAR where the background distribution in the Gaussian case disappears, while the real data presents a tail of high SNR glitches. Thus, we conclude that the search sensitivity prospects presented here do not depend on the Gaussian noise hypothesis.

[3]The cWB configuration adopted for this analysis is the same as the one used for the HL network in Section 7.2.2. The cWB Γ regulator is set to 1 (see Section 5.2 for the deinition of Γ). Chapter 5 shows that when using the data from larger detector networks, the search sensitivity can be enhanced releasing cWB likelihood regulators. Hence, the prospects presented could be improved.

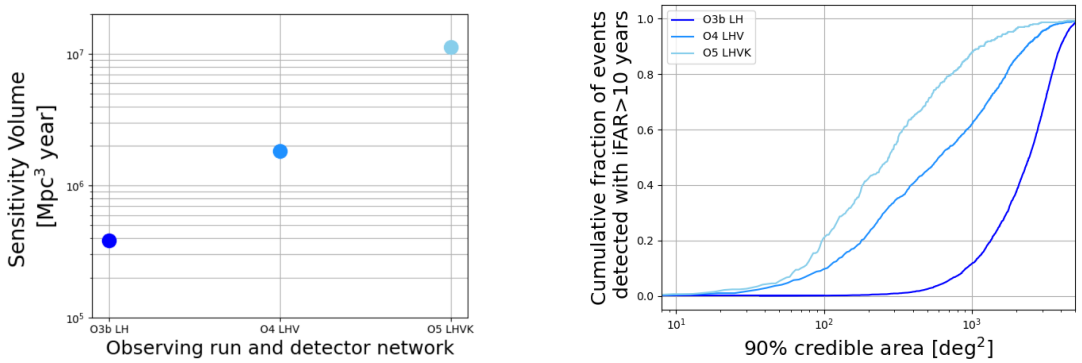

Figure 7.9: (*left*) Sensitivity volume $\langle VT \rangle$ for HE signals with component masses between $[20, 40]M_\odot$ for O3b and for future LVK observing runs (o4 and O5). A detection threshold of IFAR > 10 years is considered, as usual. (*right*) Cumulative fractions of events detected with IFAR > 10 years versus 90% credible area for the same set of injections in three different GW detector networks [174].

Fig. 7.9 presents the $\langle VT \rangle$ in O3b, and the prospects for O4 and O5. During O4, the HLV network may detect HE events up to a volume of $1.830 \pm 0.048 \times 10^6 \mathrm{Mpc}^3\mathrm{year}$, while in O5 HLVK may reach up to $1.133 \pm 0.052 \times 10^7 \mathrm{Mpc}^3\mathrm{year}$.

Similarly to the results shown in Fig. 7.8, we present the localization prospects for future observing runs. The larger the detector network analysed is, the better is the localization of the GW signals [37], especially when including detector with different alignment. Fig. 7.9 shows the 90% search area for HE with component masses in [20, 40]$M_\odot$ with O4 PSD for HLV network and O5 PSD for four-detectors network. As expected, the localization improves significantly: about 16% of the detected simulations are recovered with a search area of ~ 1000 deg^2 in HL, ~ 60%in HLV and 86% including also KAGRA.

7.4 Astrophysical implications

Several works investigate the expected rate event for HE. In this section, we compare our findings (Table 7.1) with the literature and discuss if constraints can be set on the astrophysical models. Using a simplistic consideration, the expected rate is given by the individual collision rate $\tau = nv\sigma$, being n the number density of compact objects, v their relative velocity, and σ the cross-section that depends on the impact parameter as $\sigma \sim \pi b^2$. The number of potential observation depends on the interplay between the energy released in GWs and the properties of the clusters HEs are originated from. The first, as discussed before, is determined mainly by the masses of the compact objects, and their minimum orbital separation b. Instead, n and v are fixed by astrophysical models of the stellar environments.

Ref. [98] investigates the case of HE between compact stars originated in globular cluster. The expected event rate per year is $9 \times 10^{-4}\mathrm{Mpc}^{-3}\mathrm{Myear}^{-1}$ that is a factor ~ 6000 lower than our most constraining rate. Ref. [99] presents the case of HE between primordial BHs. The expected rate per volume, assuming initial velocities between primordial BHs of 200km/s, is $\sim 0.016(\frac{b}{25GM/c^2})^2(\frac{M_{\rm PBH}}{30M_\odot})^{-2}\mathrm{Mpc}^{-3}\mathrm{Myear}^{-1}$. Considering $b = 80GM/c^2$ the expected rate is $\sim 0.16\mathrm{Mpc}^{-3}\mathrm{Myear}^{-1}$, that is a factor 40 below our best rate.

An interesting case is represented by HE involving a NS, which might be associated with an electromagnetic counterpart, referred to as shattering flares [188]. During a close encounter, a fraction of the kinetic energy of the orbit is transferred into resonant tidal coupling. If the energy of the system is enough, seismic oscillations of the NS might couple to the star magnetic field, resulting in a strong transverse electric field which accelerates particles. The luminosity of such shattering flares is estimated of the order of $\sim 10^{47} - 10^{48}$erg/s in the X-ray and soft gamma-ray bands. A multi-messenger observation of a HE between compact objects would be extremely interesting: the association of GWs with an electromagnetic counterpart would facilitate the event validation, distinguishing the GW event from glitches. In addition, it would provide great insight into the dynamics of the interaction and on the equation of state of the NS. To associate a GW signal with multi-messenger observation, it is crucial to have a precise sky localization. The search area inferred by cWB for HE simulation is discussed in Fig. 7.8 for O3b data and in Fig. 7.9 for future observing runs. Unfortunately, HE between NS are expected to be rare: the expected rate is of the order of $3 \times 10^{-6}\text{Mpc}^{-3}\text{Myear}^{-1}$ that is 8 orders of magnitude from our rate for HE component masses in [2, 5] $M_\odot$ [188].

Section 7.3 reported the sensitivity prospects for the next LVK observing runs: the sensitivity volume is expected to increase by a factor ~ 5 for O4, and by a factor ~ 27 for O5 with respect to O3b. From that estimates, in case of null detection of GW associated with HE, it would be possible to constrain extreme clusters models, and we might discuss primordial BHs density. Instead, the expected rate for HE between NS have an expected rate that is far below the current detector capabilities.

Conclusions

GW astronomy is an exciting field of research: the LVK collaboration has reported more than 90 GW signals from the first three observing runs and currently the fourth observational campaign is ongoing with an improved sensitivity of the second-generation of ground-based detectors. During the first part of the fourth observing run, 81 GW candidate events have been publicly reported [2].

To make the most of GW data, the identification and the reconstruction of GW transients are of crucial importance. Since the discovery of the first GW event, burst searches have contributed critically to the GW science, and in the next years have the potential to lead to the discovery of new GW sources and of unexpected features in GW events.

This thesis presents different original contributions to burst searches, based on the well-known unmodelled algorithm CoherentWaveBurst (cWB) [12, 113]. In the following, the main results achieved are summarized, and future perspectives are discussed.

Chapter 5 investigates the search sensitivity of the three-detectors network composed of the LIGO and Virgo detectors for burst searches. So far, the all-sky searches for short-duration GW bursts analysed the Virgo data only in periods of time when one of the LIGO detector was not operating because the inclusion of a third, not-aligned detector, decreased the search sensitivity [103]. The discovery potential advantages of a large network including Virgo were offset by an overall increase in the false alarm rate.

To enhance the contribution of Virgo data in burst searches, we investigate the effect of cWB likelihood regulators that force the reconstruction of the GW component sensed by the LIGO detectors [146]. In Gaussian noise, assuming the same sensitivity for all the detectors (Section 5.3.1), the relaxed regulators are preferred, and the use of the HLV network greatly improves the search sensitivity. Considering real detectors' sensitivity in Gaussian noise (Section 5.3.2), we show that the regulators can only be slightly relaxed because the three-detectors noise mitigation is less effective. In this case, the HLV shows a better sensitivity than HL on the majority of the simulated signals on average over the sky directions.

Next, we re-analyse a subset of the latest publicly released data, the third observing run or O3 for convenience, with relaxed regulators and using the recent cWB machine-learning based classification algorithm (Section 5.4): the relaxed regulators promote the contribution of Virgo detector and the increase of false alarms is mitigated by the classification algorithm. As a result, the search sensitivity of the HLV network is significantly enhanced: for several injected signals the three-detectors network is preferred over HL. HL is still more sensitive for high frequency signals, where the differences in spectral sensitivity between LIGO and Virgo is larger, and for single-cycle waveforms that have a morphology similar to transient noise.

In addition, we investigate the use of the HLV network to perform the waveform consistency tests used to compare the cWB unmodelled reconstruction with the waveforms generated from CBC models (Section 5.5). Studying a specific GW event from O3, we found that the HLV network weakens the statistical power of such tests, and HL should be preferred.

The investigations presented here are a first effort to characterize the current GW network. These studies were performed in preparation for the fourth observing run, but as the participation of Virgo was delayed, this project has been on hold. However, in the next years Virgo and KAGRA are expected to increase their sensitivity and LIGO India will join the network, so the understanding and the optimization of the performance of large GW network is of paramount importance to search and characterize GW sources. Moreover, progressing in these investigations is also crucial in preparation of the analyses of the data from the third generation detectors.

Chapter 6 proposes a machine-learning based algorithm to reduce the impact of glitches in burst searches. The autoencoder neural network implemented learns glitch morphologies from a dataset of GW time-series [129]. Being thought for burst searches, the network is trained only on noise samples, and no astrophysical motivated waveforms are taken into account. In particular, the autoencoder has been trained to identify blip glitches as they constitute one of the most common glitch family in GW data. Once trained, the network evaluates how much a cWB trigger is similar to the glitches contained in the training dataset. This similarity score is included in the ranking statistic of cWB [133], and shows to improve the rejection of low-frequency noise (Section 6.3). Thanks to this method, the search sensitivity towards a wide range of signals is enhanced. The most evident improvement is achieved for the simulations which have a morphology similar to blip glitches, as short-duration Gaussian pulses, few cycles sine-Gaussian waveforms and cosmic strings. The search sensitivity for BBH merger simulations is also slightly improved.

The autoencoder neural network proposed has been successfully integrated into the cWB existing infrastructure, but can similarly be included in the cWB post-processing done with Gaussian mixture model [189], or be applied to other search pipelines. In addition, the network can be trained on other morphology as well: for example, it might be used to target other glitch families that might appear in the future observing runs.

The methodological improvements presented in this thesis have been applied then to a specific scientific case. Chapter 7 presents the search for hyperbolic encounters (HE) between stellar mass compact objects in the data from the second half of the third observing run [174]. HE are scattering events between compact objects that might occur in dense stellar environments. When the masses of the objects are between few to hundreds of solar masses, the emission of GW bursts is expected in the frequency bandwidth of current ground-based detectors [97]. To search for these signals, we configure a cWB model-informed search where the XGBoost algorithm is trained with a subset of HE simulations. No significant event has been identified in addition to known observations of compact binary coalescence (Section 7.2.2).

For the first time, we published the sensitivity volume and the corresponding event rate for such sources. We inject 3 PN-accurate waveforms with component masses between $[2, 100]M_{\odot}$, impact parameter in [60, 100] GM/c^2 and orbital eccentricity in [1.05, 1.6] [177]. The maximum sensitivity is $3.9\pm1.4 \times 10^5 \mathrm{Mpc}^3\mathrm{year}$, achieved for HE with component masses between 20 and 40 $M_{\odot}$. Current detector sensitivities do not allow to constraint the astrophysical models of HEs (Section 7.4): the expected event rate for HE between primordial BHs is ~ 40 times lower than our expected rate, and the expected rate of HE originated in globular clusters is a factor $\sim$ 6000 lower [111]. We estimate the prospects for future observing runs including also Virgo and KAGRA detectors, which results encouraging for pursuing the searches of HE.

The methodological investigations presented in this thesis, in particular the improvements in the cWB search sensitivity using machine-learning based approaches and the characterization of the three-detectors network, are part of the efforts to enhance cWB in preparation for the

fourth observing run (O4), which started in May 2023 and it is currently ongoing. The author of this thesis is directly contributing to the search for all-sky GW transients on the data from the first part of O4, doing the analyses and writing the manuscript for the related LVK collaboration paper. Moreover, for the GW candidate events observed in O4 data, the author is testing the agreement between the waveform reconstructed with weak assumptions by cWB and the waveform generated by CBC models, as described in Section 5.5. These results have not been reported in this thesis because the data of the fourth observing run are not yet public.

GW science is an exciting field of research: the current detectors are continuously improving their sensitivities, increasing the rate of GW observations. In the next decades, third-generation ground-based detectors and the space-based detectors will further expand the horizon of GW astronomy. Burst searches have a huge discovery potential: they allow the detection of new GW sources, and allow testing if the theoretical models describe accurately the measured data. This thesis proposes several original contributions in this domain, enhancing the characterization of the algorithm cWB toward large detectors networks, improving the mitigation of transient noise, and searching for an interesting GW source that has not been observed yet.

Appendix A

Detecting overlapping GW signals

Current detection algorithms make the assumption that the data contains one signal at any time. However, as the GW detectors sensitivity improves, more likely the data will contain more than a GW signal close in time. This appendix presents the detection capability of overlapping GW signals with two pipelines currently used by the LVK collaboration: the template-based search pyCBC [64] and the unmodelled search cWB, described in detail in the fourth chapter. The search sensitivity is evaluated on simulated signals from the coalescence of BBH and BNS systems.

This section is organized as following: Section A.1 describes the injections performed, Section A.2 describes the search algorithms, focusing especially on cWB configuration, and Section A.3 presents the search results.

The findings reported here have been published in Ref. [45].

A.1 Injection sets

To study the capability of current detection algorithms of identifying overlapping signals, we inject BBH and BNS simulations into Gaussian noise of the three-detectors network composed of the LIGO and the Virgo detectors (HLV).

The GW waveforms from the merger of BBH are simulated with SEOBNRv4PHM approximant [172]. Component masses are drawn from recent PowerLaw + Peak binary mass distributions used within the LVK collaboration [16]. BH masses are in the range of [5, 100] $M_{\odot}$ and the mass ratios m_1/m_2 are in [0.1,1]. For BNS systems, the GW approximant is SEOBNRv4 [190], and component masses are in the range [1.14, 3]$M_{\odot}$. The BBH simulations have a distance in [200, 1300]Mpc, and BNS in [5, 200]Mpc, in order to obtain signals with SNR ranging between 5 and 50 in both cases.

Two CBC signals are injected together, investigating different regions of overlap. These regions have been defined considering previous studies on overlapping signals and their effect on the parameter estimation of their physical parameters [191]. The three regions are: I) a *strong bias* region where the two signals strongly affect each other, having their coalescence time t_c separated by $|\Delta t_c|$ <0.5s for BBH, and $|\Delta t_c|$ <0.01s for BNS. BNS systems merge at higher frequencies and the characterization of the signals is significantly biased when $|\Delta t_c|$ includes the last cycles before the merger; II) a *weak bias* region, where both signals are recovered slightly biased, but broadly correct. The coalescence time in this region differs by $0.5 < |\Delta t_c| < 2$s for BBH and to lower limit for BNS; III) a *negligible bias* region where the signals are separated

enough in time to not cause noticeable biases in the estimation of their physical parameters. This region is defined by $|\Delta t_c| > 2$s.

A.2 Detection algorithms

We compare the detection capabilities towards overlapping CBC signals using two different pipelines. the first is pyCBC [64], a template-based algorithms based on matched-filter (see Section 2.2.2). For each trigger, pyCBC returns a time that corresponds to the visible end of the signal in the data. We consider a simulation recovered if the merger time is within ± 0.1s within the end time.

The second algorithm is cWB, the burst pipelines described in detail in the fourth chapter. The configuration of cWB employed is the one used to search for BBH mergers: the time-frequency clusters are selected following a diagonal pattern, which mimic the chirp signal. In post-production, triggers with central frequency above 512Hz are removed. In the fifth chapter, we investigate the performance of cWB on the three-detectors network HLV, and we discuss the impact of likelihood regulators, in particular of the regulators Γ (Section 5.2). Fig. 5.7 shows that for signals in the intermediate frequency range (100-300Hz), the HLV network with released constrain outperforms significantly the HL network. For the study reported in this section, we perform a preliminary investigation both with $\Gamma = 1$ and $\Gamma = 0.5$. At IFAR>1 year, we obtain a detection efficiency of 47% with hard regulators, and 58% with soft regulator. Thus, for this study we set $\Gamma = 0.5$.

cWB, as it does not use templates, returns a mean time, weighted with energy, and an estimation of the end time of the reconstructed waveform. Using the same window time as for pyCBC results in high number of injection being rejected. So, we consider a signal recovered if it is within ± 2.5 w.r.t to the cWB end time.

A.3 Search sensitivity

This section discussed the detection efficiencies found by the two search algorithms on overlapping CBC. Fig. A.1 and Fig. A.2 show the percentage of recovered injections in the different bias regions for BBH and BNS simulations, respectively. As expected, the match-filter search has a higher detection efficiency for both types of signals. The difference is particularly evident for BNS: these systems produce a longer GW signal that match with GW waveform models contained in pyCBC's template banks for several cycles. At the same time, longer GW signals are more spread in time-frequency maps and the cWB collection of SNR is less efficient.

Inside the weak and strong bias regions, in some cases both the injections are found in the same trigger. This means that a single injection is counted twice. In Fig. A.1 and Fig. A.2, we report the percentages of unique triggers, i.e. the injections correctly reconstructed, removing the duplicated triggers.

As expected, the unique detection efficiencies decrease for weak and strong biases in cWB, and in the strong region for pyCBC. Both searches find signal pairing with close merger time, however often only one of the two signals is recovered.

To better understand cWB behaviour with overlapping signals, we report the time-frequency map of the likelihood and the null, which represent the energy that is coherent and uncoherent in the detector network. As described in Section 4.1.4, cWB maximizes the likelihood statistics over all sky direction, regardless of the number of signals that are part of the trigger. When a single signal is present, as in Fig. A.3, the pipeline maximizes the likelihood w.r.t. most of the signal energy is contained in the likelihood, while the null is almost empty.

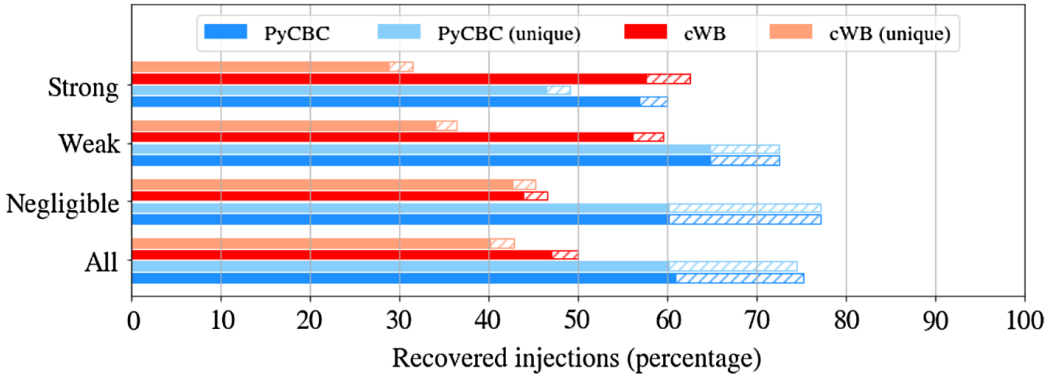

Figure A.1: Percentage of recovered injections by cWB (red) and pyCBC (blue) in different overlap regions for BBH merger injections. The shaded regions corresponds to a detection threshold of IFAR<1 year. The 'unique' column reports the percentage of unique triggers: when two signals are reconstructed at the same time, the duplicate event is removed [45].

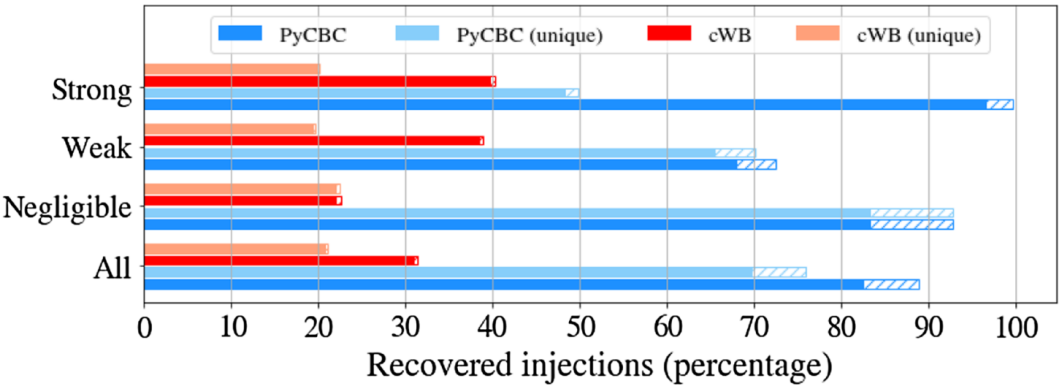

Figure A.2: Percentage of recovered injections by cWB (red) and pyCBC (blue) in different overlap regions for BNS injections. The shaded regions corresponds to a detection threshold of IFAR<1year. The 'unique' column reports the percentage of unique triggers when two signals are reconstructed at the same time, the duplicate event is removed [45].

Instead, when there are two close signals the likelihood is largely maximized w.r.t to the loudest signals with some contamination from the secondary signal, according to its energy. As shown in Fig. A.4, the majority of the energy of the primary signal is found in the likelihood. The energy of the secondary signal is split between the likelihood and the null according to the source localization: if it close to the position of the first signal the energy of the secondary signal will be largely in the likelihood, instead if the source positions o the two signals differ significantly, the energy of the secondary signal will be in the null. The energy found in the null contributes to the uncoherent energy E_c, lowering the cWB ranking statics (Eq.4.34). For this reason, overlapping triggers are penalized by cWB.

To improve the search sensitivity to overlapping signals, cWB should allow for the estimation of multiple likelihoods: if there are indications of another signal in the null, a second likelihood

maximization could be computed in the time-frequency pixels found in the null.

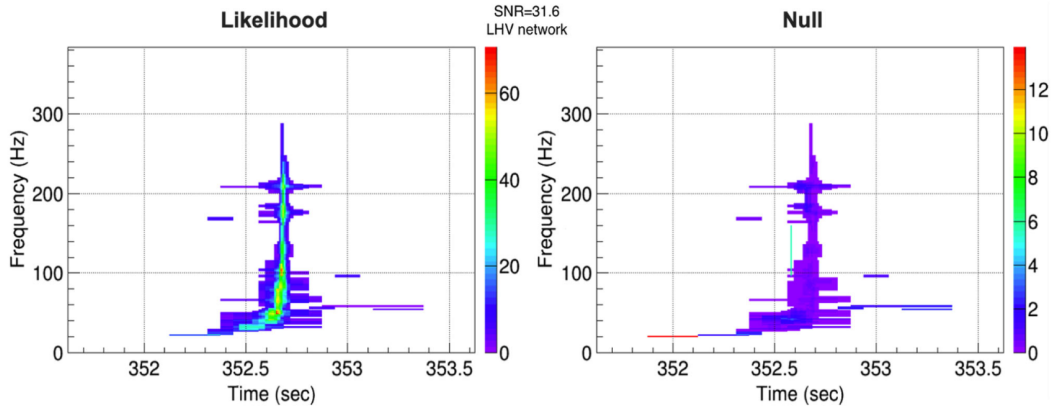

Figure A.3: Spectrogram of likelihood and null (coherent and uncoherent energy) computed by cWB for a single BBH event. Note the different colour scales for the two maps. As expected, the likelihood contains the majority of the signal energy. [45].

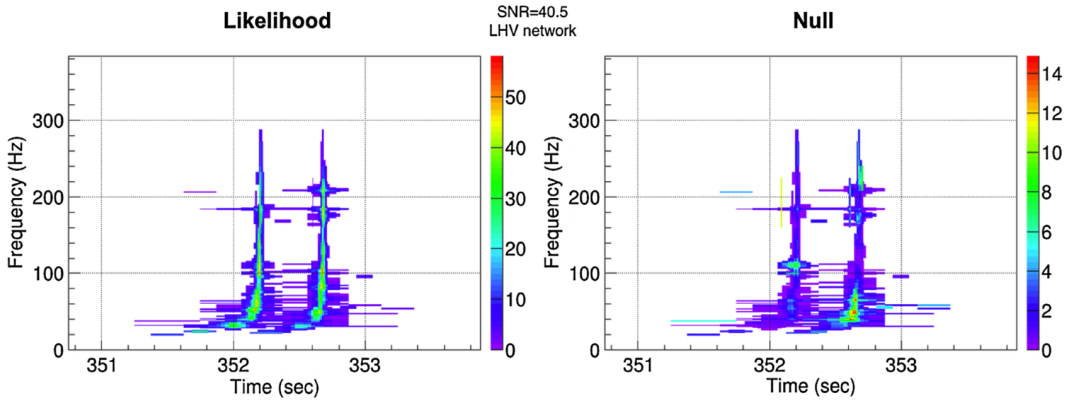

Figure A.4: Spectrogram of likelihood and null energy computed by cWB for two overlapping BBH signals. Note the different colour scales for the two maps. The likelihood is maximised with respect to the primary signal, i.e. the one favoured w.r.t. the other. Hence, a significant fraction of the energy associated to the second signal is contained in the null map [45].

Appendix B

Detector responses in the polarization pattern

In this section, we derive the equations Eq. 5.5, in particular we show that the 90° phase shifted component has only the cross component.

In Section 5.2, we introduce the following parameterization of the detector response $\mathbf{g}$ and the 90° phase shifted response $\tilde{\mathbf{g}}$:

$$\begin{aligned} \mathbf{g} &= h_1\mathbf{F}_+(\psi) + eh_2\mathbf{F}_\times(\psi) \\ \tilde{\mathbf{g}} &= -h_2\mathbf{F}_+(\psi) + eh_1\mathbf{F}_\times(\psi) \end{aligned} \tag{B.1}$$

where h_1 and h_2 are the strain amplitudes, e is the wave ellipticity and ψ the polarization angle. These parameters are found maximizing the likelihood statistics. The antenna pattern vectors used above are related to the dominant polarization frame $(\mathbf{f}_+, \mathbf{f}_\times)$ as:

$$\begin{aligned} \mathbf{F}_+(\psi) &= \mathbf{f}_+\cos(\gamma) - \mathbf{f}_\times\sin(\gamma) \\ \mathbf{F}_\times(\psi) &= \mathbf{f}_\times\cos(\gamma) - \mathbf{f}_+\sin(\gamma) \end{aligned} \tag{B.2}$$

Eq. 5.5 is derived applied the polarization phase transformation to $\tilde{\mathbf{g}}$ and $\mathbf{g}$. In the following we show the computation only for $\tilde{\mathbf{g}}$ for simplicity. The polarization phase transformation is:

$$\tilde{\mathbf{g}}' = \tilde{\mathbf{g}}\cos\lambda_i - \mathbf{g}\sin\lambda_i \tag{B.3}$$

where, neglecting the normalization constant is:

$$\cos\lambda_i \propto (\mathbf{g}[i]\cdot\mathbf{e}_+[i]), \quad \sin\lambda_i \propto (\tilde{\mathbf{g}}[i]\cdot\mathbf{e}_+[i]) \tag{B.4}$$

Hence, Eq. B.3 is:

$$\tilde{\mathbf{g}}' = \tilde{\mathbf{g}}\mathbf{g}_+ - \mathbf{g}\tilde{\mathbf{g}}_+ \tag{B.5}$$

From Eq. B.1 and B.2, we have:

$$\mathbf{g} = h_1(\mathbf{f}_+\cos\gamma - \mathbf{f}_\times\sin\gamma) + eh_2(\mathbf{f}_\times\cos\gamma + \mathbf{f}_+\sin\gamma) \tag{B.6}$$

$$\mathbf{g}_+ = \mathbf{f}_+(h_1\cos\gamma + eh_2\sin\gamma) \tag{B.7}$$

And,

$$\tilde{\mathbf{g}} = -h_2(\mathbf{f}_+\cos\gamma - \mathbf{f}_\times\sin\gamma) + eh_1(\mathbf{f}_\times\cos\gamma + \mathbf{f}_+\sin\gamma) \tag{B.8}$$

$$\tilde{\mathbf{g}}_+ = \mathbf{f}_+(-h_2\cos\gamma + eh_1\sin\gamma) \tag{B.9}$$

Substituting all the terms in Eq. B.5, and neglecting the vector notation for simplicity, we have:

$$\begin{aligned}
\tilde{g}' = &[-h_2(f_+\cos\gamma - f_\times\sin\gamma) + eh_1(f_\times\cos\gamma + f_+\sin\gamma)](h_1\cos\gamma + eh_2\sin\gamma)\\
&-[h_1(f_+\cos\gamma - f_\times\sin\gamma) + eh_2(f_\times\cos\gamma + f_+\sin\gamma)](-h_2\cos\gamma + eh_1\sin\gamma)\\
&= -h_1h_2f_+\cos^2\gamma + h_1h_2f_\times\sin\gamma\cos\gamma + eh_1^2f_\times\cos^2\gamma + eh_1^2f_+\sin\gamma\cos\gamma\\
&-eh_2^2f_+\cos\gamma\sin\gamma + eh_2^2f_\times\sin^2\gamma + e^2h_1h_2f_\times\cos\gamma\sin\gamma + e^2h_1h_2f_+\sin^2\gamma\\
&+h_1h_2f_+\cos^2\gamma - h_1h_2f_\times\sin\gamma\cos\gamma + eh_2^2f_\times\cos^2\gamma + eh_2^2f_+\cos\gamma\sin\gamma\\
&-eh_1^2f_+\cos\gamma\sin\gamma + eh_1^2f_\times\sin^2\gamma - e^2h_1h_2f_\times\sin\gamma\cos\gamma - e^2h_1h_2f_+\sin^2\gamma
\end{aligned} \tag{B.10}$$

The plus component is:

$$\begin{aligned}
\tilde{g}'_+ = f_+(&-h_1h_2\cos^2\gamma + eh_1^2\sin\gamma\cos\gamma - eh_2^2\cos\gamma\sin\gamma + e^2h_1h_2\sin^2\gamma +\\
&h_1h_2\cos^2\gamma + eh_2^2\cos\gamma\sin\gamma - eh_1^2\cos\gamma\sin\gamma - e^2h_1h_2\sin^2\gamma)
\end{aligned} \tag{B.11}$$

highlighting equal terms in different colours it is clear that $\tilde{g}'_+ = 0$:

$$\begin{aligned}
\tilde{g}'_+ = f_+(&-h_1h_2\cos^2\gamma + eh_1^2\sin\gamma\cos\gamma - eh_2^2\cos\gamma\sin\gamma + e^2h_1h_2\sin^2\gamma\\
&+h_1h_2\cos^2\gamma + eh_2^2\cos\gamma\sin\gamma - eh_1^2\cos\gamma\sin\gamma - e^2h_1h_2\sin^2\gamma) = 0
\end{aligned} \tag{B.12}$$

Instead, the cross component:

$$\begin{aligned}
\tilde{g}'_\times = &f_\times(h_1h_2\sin\gamma\cos\gamma + eh_1^2\cos^2\gamma + eh_2^2\sin^2\gamma + e^2h_1h_2\cos\gamma\sin\gamma\\
&-h_1h_2\sin\gamma\cos\gamma + eh_2^2\cos^2\gamma + eh_1^2\sin^2\gamma - e^2h_1h_2\sin\gamma\cos\gamma) =\\
&f_\times(eh_1^2 + eh_2^2) = f_\times eh_0
\end{aligned} \tag{B.13}$$

where we use $h_0 = \sqrt{h_1^2 + h_2^2}$. The result in Eq. B.13 is the one reported in Section 5.2 and in Ref. [146] unless a normalization constant.

Appendix C

Autoencoder statistics in CoherentWaveBurst

This appendix reports additional details about the use of the autoencoder neural network to mitigate glitches in burst searches, proposed in the Chapter 6.

As presented in Section 6.2.2, during the training procedure the autoencoder learns the time-series of blip glitches from a labelled dataset. Once trained, the autoencoder is applied to cWB triggers, and it evaluates how much each trigger under investigation is similar to a blip glitch.

In Fig. 6.3, we show the comparison between the autoencoder input and its reconstruction in the case of blip glitches. In that case, the autoencoder reconstruction accurately matches the input time-series. Fig. C.1 shows two examples of autoencoder reconstructions for non-blip waveforms. The autoencoder struggles to reconstruct the waveforms with a different morphology, which is not present in the training dataset, and the output are clearly different w.r.t. the input.

This similarity is measured using the mean square error (MSE) metric, defined in Eq. 6.1. In the following, the MSE between the cWB trigger and its corresponding autoencoder reconstruction is also referred to as autoencoder statistics.

Here, we report a series of figures about the autoencoder statistics to better understand the capabilities of the methods and its relationship with the other cWB summary statistics.

Fig. C.2 shows the cWB ranking statistic ρ (Eq. 4.34) versus the autoencoder statistics for the background triggers. The red line marks the autoencoder MSE mean values achieved on blip glitches contained in the test dataset, and the 90th percentile. About 10% of background triggers have a MSE lower than the 90th percentile, meaning that they have a morphology similar to blip glitches. It is not surprising that a larger fraction of background triggers shows also high value of MSE because cWB background contains trigger with different morphology, duration and frequency.

Fig. C.2 shows the autoencoder statistic distribution for a set of ad-hoc injections, including Gaussian pulses (GA), sine-Gaussian (SG) and white noise burst (WNB). As expected, the GA simulations have the most similar morphology to blip glitches, and a large fraction of these simulations overlap with the area populated by labelled blip glitches. Instead, the autoencoder is able to differentiate between blip glitches and WNB and the majority of SG waveforms. The SG with lowest autoencoder statistics are the one with low Q factor ($Q = 3$) and low frequency (70Hz). It is important to recall that the neural network proposed in the sixth chapter is trained on a single class of event. This is motivated by the desire to employ this method for all-sky unmodelled searches. At the same time, machine-learning based algorithms trained on a single class of events have a lower capability of distinguishing between different classes, than the

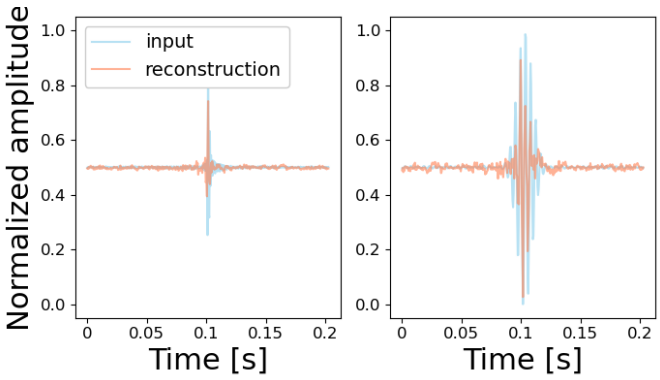

Figure C.1: Two examples of the autoencoder reconstruction of two injected signals, with a morphology different from blip glitches. The autoencoder inputs (in blue) are the waveform reconstructed by cWB, windowed and normalized as described in Section 6.2.3. The autoencoder reconstruction (in orange) does not match accurately the input data, especially in comparison with the reconstruction of blip glitches showed in Fig. 6.3

algorithms trained on multiple classes.

Similarly, Fig. C.3 shows the MSE autoencoder statistics versus the total mass of BBH merger simulations described in Section 6.3. The more massive the systems, the lower the frequency of the signal at merger and the shorter the GW signal contained in the detector bandwidth, so that for intermediate mass BH systems only the last few cycles before the merger can be observed. This results in a correlation between the mass of the BBH and the similarity to a blip glitches. From Fig. C.3, we found that the autoencoder neural network is not able to discriminate the majority of BBH mergers having total mass above $200M_{\odot}$.

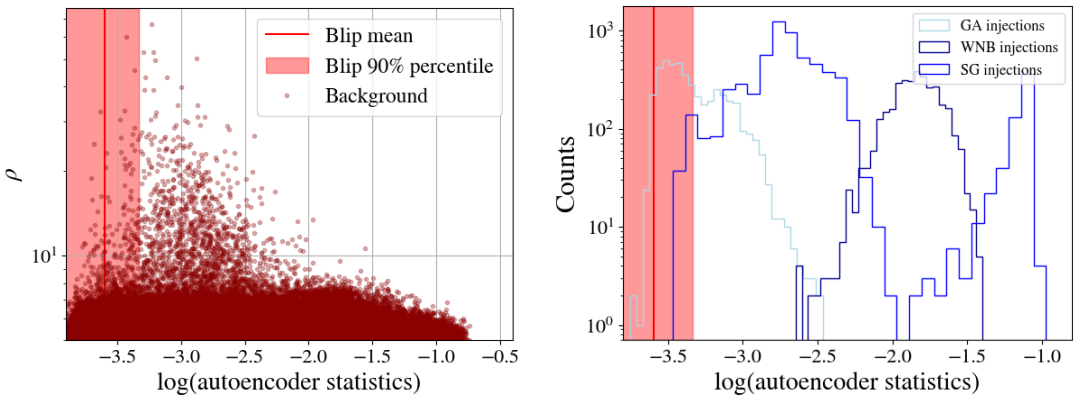

Figure C.2: (*left*) MSE autoencoder statistics versus cWB ranking statistics for background triggers. The red line marks the MSE mean values achieved on blip glitches from the labelled test dataset, and the red shaded area include the 90th percentile. About 10% of the background triggers are contained in the red region, meaning that they are consistent with blip glitches. (*right*) Histogram of the autoencoder statistics for ad-hoc simulations. The red line marks the MSE mean values achieved on blip glitches from the test dataset, and the red shaded area include the 90th percentile.

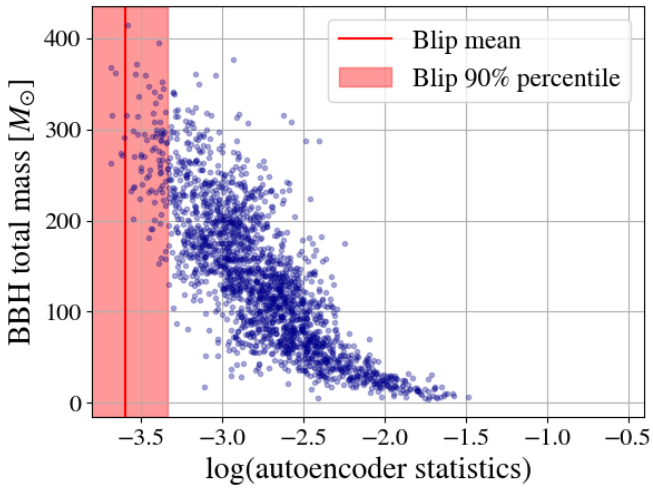

Figure C.3: MSE autoencoder statistics versus the total mass of the BBH merger simulations. The red line indicates the mean of autoencoder statistics achieved on the blip test dataset, and the shaded regions contains the 90th percentile of the labelled glitches from the training dataset. As expected, the more massive the system, the more similar to blip glitches.

Moreover, Fig. C.4 shows the autoencoder statistics versus the cWB correlation coefficient *cc*(defined in Eq. 4.33) background triggers and ad-hoc simulations. This plot is an example of correlation between different cWB features, and it is useful to understand why the machine-learning post-processing algorithm presented in Section 4.1.6 improved the search sensitivity. The higher the *cc*, the larger the energy coherent in the detector network w.r.t. the energy that it is not coherent in the detectors, suggesting a higher probability that it is a genuine signal. Instead, low *cc* values indicate that the signal is likely a glitch.

Before using XGBoost, cWB applied hand-tuned post-processing cuts to reduce the impact of transient noise. Typically, triggers with $cc < 0.7$ were discarded. Fig. C.4 shows clearly the limit of such cut: a fraction of the simulations has a lower correlation coefficient, while a certain amount of background triggers has higher *cc*. It is more efficient to apply a cut in this two-dimensional parameter space: the region between $cc > 0.7$ and logarithm of the autoencoder statistics > 2.3 contains more simulations than background and should not be discarded. Background triggers similar to blip glitches might also have high *cc* and should be discarded. XGBoost is a decision-tree learning algorithm that performs multidimensional correlations in a large parameter space, and shows to successfully be able to learn complex correlations between cWB features than enhanced the cWB search sensitivity.

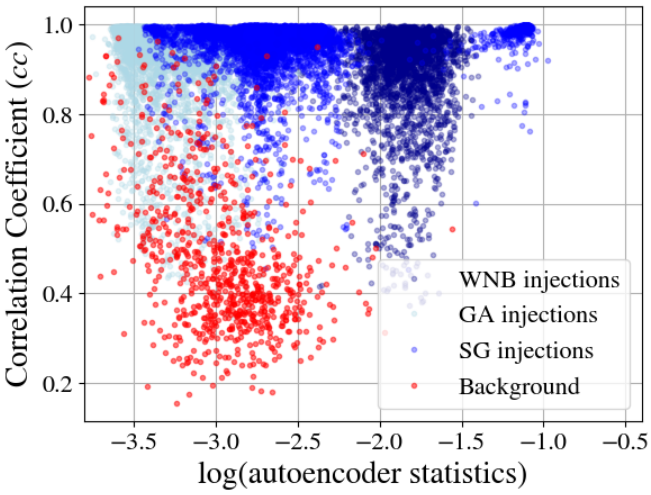

Figure C.4: MSE autoencoder statistics versus the correlation coefficient cc (Eq. 4.33) for background triggers (red) and ad-hoc injections (blue). Only the loudest background triggers are shown ($\rho > 10$, see Eq. 4.34). High values of cc indicate that the trigger is highly coherent in the detector network, and it is a potential astrophysical signal, while low values suggests it is a transient noise. Before using the XGBoost algorithm, cWB searches removed the triggers with $cc < 0.7$.

Appendix D

Choice of the significance threshold for the search of hyperbolic encounters

In the seventh chapter, we perform injections of HE GW waveforms in the O3b data to evaluate the search sensitivity of the proposed model-informed search. The HE waveforms are uniformly injected into a volume V_0 (Eq. 7.20), and from the number of injections recovered (Eq. 7.21), the sensitivity volume $\langle VT \rangle$, distance and event rate are estimated. The results presented in Section 7.2.2 and Section 7.3 consider a HE simulation as recovered if the cWB trigger has a significance of IFAR>10 years. cWB associates to each trigger a significance in terms of false alarm rate (FAR) computed from the background distribution (see Section 4.1.5). This latter is build analysing time-shifted data, so that the triggers that are coherent cannot be astrophysical signals by construction, but are non-Gaussian noises. The FAR of an event with ranking statistic ρ_i is given by:

$$\mathrm{FAR} = \frac{N_{\rho > \rho_i}}{T} \tag{D.1}$$

where $N_{\rho > \rho_i}$ is the number of background triggers with ρ larger than the event under investigation ρ_i, and T the total background time. The inverse false alarm rate (IFAR) is simply the inverse of Eq. D.1. Here, alternative significance thresholds are briefly discussed.

Fig. D.1 shows how the sensitivity volume $\langle VT \rangle$ varies with different IFAR thresholds for HE simulations with component masses between 20 and $40 M_\odot$ [174]. This mass range is the one that provides the largest sensitive volume on O3b data, and similar trends are obtained also with the other mass ranges. Higher IFAR thresholds constrain more the search sensitivity, but at the same time are more subjected to statistical fluctuations of the background distribution. Indeed, at high significance thresholds, the number of recovered simulations decreases, and it strongly depends on the high SNR tail of the background distribution, which contains few loud glitches. In this case, the number of recovered simulations might strongly depend on the amount of background computed. For these reasons, the choice of IFAR> 10 years has been adopted.

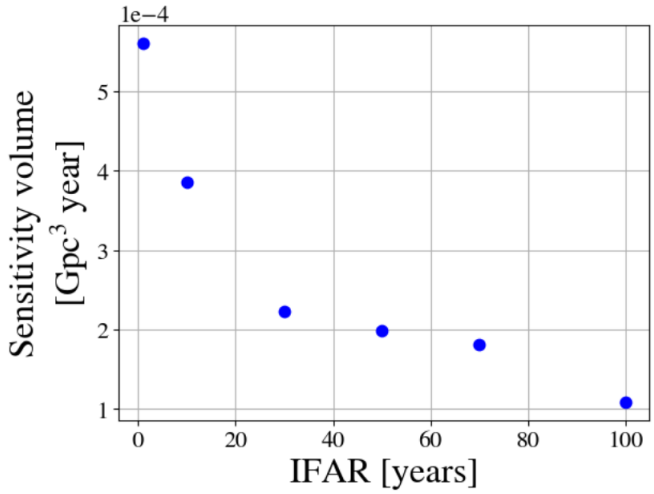

Figure D.1: Sensitive volume $\langle VT \rangle$ computed considering different significance thresholds for HE with component masses in [20, 40] $M_{\odot}$. The results reported in the seventh chapter consider IFAR$>$ 10 years [174]

Bibliography

[1] R. Abbott et al. *GWTC-3: Compact Binary Coalescences Observed by LIGO and Virgo During the Second Part of the Third Observing Run*. Nov. 2021. arXiv: 2111.03606 [gr-qc].

[2] LIGO-Virgo-KAGRA collaboration. *GraceDB*. 2024. URL: https://gracedb.ligo.org/superevents/public/O4/ (visited on 2024).

[3] Jorge L Cervantes-Cota, Salvador Galindo-Uribarri, and George F Smoot. "A brief history of gravitational waves". In: *Universe* 2.3 (2016), p. 22.

[4] Felix AE Pirani. "On the physical significance of the Riemann tensor". In: *Acta Physica Polonica* 15 (1956), pp. 389–405.

[5] Joseph Weber. "Detection and generation of gravitational waves". In: *Physical Review* 117.1 (1960), p. 306.

[6] Joseph Weber. "Evidence for discovery of gravitational radiation". In: *Physical Review Letters* 22.24 (1969), p. 1320.

[7] Russell A Hulse and Joseph H Taylor. "Discovery of a pulsar in a binary system". In: *The Astrophysical Journal* 195 (1975), pp. L51–L53.

[8] KL Dooley et al. "GEO 600 and the GEO-HF upgrade program: successes and challenges". In: *Classical and Quantum Gravity* 33.7 (2016), p. 075009.

[9] Junaid Aasi et al. "Advanced ligo". In: *Classical and quantum gravity* 32.7 (2015), p. 074001.

[10] Fet al Acernese et al. "Advanced Virgo: a second-generation interferometric gravitational wave detector". In: *Classical and Quantum Gravity* 32.2 (2014), p. 024001.

[11] Benjamin P Abbott et al. "Observation of gravitational waves from a binary black hole merger". In: *Physical review letters* 116.6 (2016), p. 061102.

[12] Marco Drago et al. "Coherent WaveBurst, a pipeline for unmodeled gravitational-wave data analysis". In: *SoftwareX* 14 (2021), p. 100678.

[13] T Akutsu et al. "Overview of KAGRA: Detector design and construction history". In: *Progress of Theoretical and Experimental Physics* 2021.5 (2021), 05A101.

[14] Benjamin P Abbott et al. "GW170817: observation of gravitational waves from a binary neutron star inspiral". In: *Physical review letters* 119.16 (2017), p. 161101.

[15] R Abbott et al. "Tests of general relativity with GWTC-3". In: *arXiv:2112.06861* (2021).

[16] R Abbott et al. "Population of merging compact binaries inferred using gravitational waves through GWTC-3". In: *Physical Review X* 13.1 (2023), p. 011048.

[17] CS Unnikrishnan. "IndIGO and LIGO-India: Scope and plans for gravitational wave research and precision metrology in India". In: *International Journal of Modern Physics D* 22.01 (2013), p. 1341010.

[18] M Punturo et al. “The Einstein Telescope: a third-generation gravitational wave observatory”. In: *Classical and Quantum Gravity* 27.19 (2010), p. 194002.

[19] David Reitze et al. “Cosmic explorer: the US contribution to gravitational-wave astronomy beyond LIGO”. In: *arXiv preprint arXiv:1907.04833* (2019).

[20] Pau Amaro-Seoane et al. “Laser interferometer space antenna”. In: *arXiv:1702.00786* (2017).

[21] Michele Maggiore. *Gravitational waves: Volume 1: Theory and experiments*. OUP Oxford, 2007.

[22] Benjamin P Abbott et al. “Properties of the binary black hole merger GW150914”. In: *Physical review letters* 116.24 (2016), p. 241102.

[23] R Abbott et al. “GWTC-2: compact binary coalescences observed by LIGO and Virgo during the first half of the third observing run”. In: *Physical Review X* 11.2 (2021), p. 021053.

[24] BP Abbott et al. “GWTC-1: a gravitational-wave transient catalog of compact binary mergers observed by LIGO and Virgo during the first and second observing runs”. In: *Physical Review X* 9.3 (2019), p. 031040.

[25] R Abbott et al. “All-sky search for continuous gravitational waves from isolated neutron stars using Advanced LIGO and Advanced Virgo O3 data”. In: *Physical Review D* 106.10 (2022), p. 102008.

[26] R Abbott et al. “All-sky search for gravitational wave emission from scalar boson clouds around spinning black holes in LIGO O3 data”. In: *Physical Review D* 105.10 (2022), p. 102001.

[27] R Abbott et al. “Search for gravitational waves from Scorpius X-1 with a hidden Markov model in O3 LIGO data”. In: *Physical Review D* 106.6 (2022), p. 062002.

[28] R Abbott et al. “Searches for gravitational waves from known pulsars at two harmonics in the second and third LIGO-Virgo observing runs”. In: (2022).

[29] R Abbott et al. “Search for continuous gravitational wave emission from the Milky Way center in O3 LIGO-Virgo data”. In: *Physical Review D* 106.4 (2022), p. 042003.

[30] R Abbott et al. “Narrowband searches for continuous and long-duration transient gravitational waves from known pulsars in the LIGO-Virgo third observing run”. In: *The Astrophysical Journal* 932.2 (2022), p. 133.

[31] R Abbott et al. “Search of the early O3 LIGO data for continuous gravitational waves from the Cassiopeia A and Vela Jr. supernova remnants”. In: *Physical Review D* 105.8 (2022), p. 082005.

[32] R Abbott et al. “Constraints from LIGO O3 Data on Gravitational-wave Emission Due to R-modes in the Glitching Pulsar PSR J0537–6910”. In: *The Astrophysical Journal* 922.1 (2021), p. 71.

[33] R Abbott et al. “All-sky, all-frequency directional search for persistent gravitational waves from Advanced LIGO’s and Advanced Virgo’s first three observing runs”. In: *Physical Review D* 105.12 (2022), p. 122001.

[34] Ryan Abbott et al. “Upper limits on the isotropic gravitational-wave background from Advanced LIGO and Advanced Virgo’s third observing run”. In: *Physical Review D* 104.2 (2021), p. 022004.

[35] R Abbott et al. "Search for anisotropic gravitational-wave backgrounds using data from Advanced LIGO and Advanced Virgo's first three observing runs". In: *Physical Review D* 104.2 (2021), p. 022005.

[36] J Abadie et al. "Calibration of the LIGO gravitational wave detectors in the fifth science run". In: *Nuclear Instruments and Methods in Physics Research Section A: Accelerators, Spectrometers, Detectors and Associated Equipment* 624.1 (2010), pp. 223–240.

[37] Benjamin P Abbott et al. "Prospects for observing and localizing gravitational-wave transients with Advanced LIGO, Advanced Virgo and KAGRA". In: *Living reviews in relativity* 23 (2020), pp. 1–69.

[38] Benjamin P Abbott et al. "A guide to LIGO–Virgo detector noise and extraction of transient gravitational-wave signals". In: *Classical and Quantum Gravity* 37.5 (2020), p. 055002.

[39] Junaid Aasi et al. "Enhanced sensitivity of the LIGO gravitational wave detector by using squeezed states of light". In: *Nature Photonics* 7.8 (2013), pp. 613–619.

[40] Fausto Acernese et al. "Frequency-Dependent Squeezed Vacuum Source for the Advanced Virgo Gravitational-Wave Detector". In: *Physical review letters* 131.4 (2023), p. 041403.

[41] L McCuller et al. "Frequency-dependent squeezing for advanced LIGO". In: *Physical review letters* 124.17 (2020), p. 171102.

[42] The Virgo Collaboration. *Advanced Virgo Plus Phase I - Design Report*. Tech. rep. The Virgo Collaboration, 2019.

[43] A Rocchi et al. "Thermal effects and their compensation in Advanced Virgo". In: *Journal of Physics: Conference Series*. Vol. 363. 1. IOP Publishing. 2012, p. 012016.

[44] Michael W Coughlin et al. "Implications of dedicated seismometer measurements on Newtonian-noise cancellation for Advanced LIGO". In: *Physical review letters* 121.22 (2018), p. 221104.

[45] Philip Relton et al. "Addressing the challenges of detecting time-overlapping compact binary coalescences". In: *Physical Review D* 106.10 (2022), p. 104045.

[46] Chris Pankow et al. "Mitigation of the instrumental noise transient in gravitational-wave data surrounding GW170817". In: *Physical Review D* 98.8 (2018), p. 084016.

[47] Ronaldas Macas et al. "Impact of noise transients on low latency gravitational-wave event localization". In: *Physical Review D* 105.10 (2022), p. 103021.

[48] Jack YL Kwok et al. "Investigation of the effects of non-Gaussian noise transients and their mitigation in parameterized gravitational-wave tests of general relativity". In: *Physical Review D* 105.2 (2022), p. 024066.

[49] Derek Davis et al. "LIGO detector characterization in the second and third observing runs". In: *Classical and Quantum Gravity* 38.13 (2021), p. 135014.

[50] F Acernese et al. "Virgo Detector Characterization and Data Quality during the O3 run". In: *arXiv preprint arXiv:2205.01555* (2022).

[51] R. Schofield. aLIGO LHO Logbook 52184, LIGO Laboratory. 2020.

[52] Joshua R Smith et al. "A hierarchical method for vetoing noise transients in gravitational-wave detectors". In: *Classical and Quantum Gravity* 28.23 (2011), p. 235005.

[53] Elena Cuoco et al. "Enhancing gravitational-wave science with machine learning". In: *Machine Learning: Science and Technology* 2.1 (2020), p. 011002.

[54] Nikhil Mukund et al. “Transient classification in LIGO data using difference boosting neural network”. In: *Physical Review D* 95.10 (2017), p. 104059.

[55] Jade Powell et al. “Classification methods for noise transients in advanced gravitational-wave detectors”. In: *Classical and Quantum Gravity* 32.21 (2015), p. 215012.

[56] Daniel George, Hongyu Shen, and EA Huerta. “Classification and unsupervised clustering of LIGO data with Deep Transfer Learning”. In: *Physical Review D* 97.10 (2018), p. 101501.

[57] Massimiliano Razzano and Elena Cuoco. “Image-based deep learning for classification of noise transients in gravitational wave detectors”. In: *Classical and Quantum Gravity* 35.9 (2018), p. 095016.

[58] Lee Lindblom. “Optimal calibration accuracy for gravitational-wave detectors”. In: *Physical Review D* 80.4 (2009), p. 042005.

[59] Ling Sun et al. “Characterization of systematic error in Advanced LIGO calibration”. In: *Classical and Quantum Gravity* 37.22 (2020), p. 225008.

[60] Benjamin P Abbott et al. “Calibration of the Advanced LIGO detectors for the discovery of the binary black-hole merger GW150914”. In: *Physical Review D* 95.6 (2017), p. 062003.

[61] Ling Sun et al. “Characterization of systematic error in Advanced LIGO calibration in the second half of O3”. In: *arXiv preprint arXiv:2107.00129* (2021).

[62] D. Estevez et al. *Online h(t) reconstruction for Virgo O3 data: start of O3*. Tech. rep. Virgo, VIR-0652B-19, 2019.

[63] L. Rolland et al. *pdate on h(t) uncertainties during O3*. Tech. rep. Virgo, VIR-0688A-20, 2020.

[64] Samantha A Usman et al. “The PyCBC search for gravitational waves from compact binary coalescence”. In: *Classical and Quantum Gravity* 33.21 (2016), p. 215004.

[65] Kipp Cannon et al. “GstLAL: A software framework for gravitational wave discovery”. In: *SoftwareX* 14 (2021), p. 100680.

[66] Qi Chu et al. “SPIIR online coherent pipeline to search for gravitational waves from compact binary coalescences”. In: *Physical Review D* 105.2 (2022), p. 024023.

[67] Florian Aubin et al. “The MBTA pipeline for detecting compact binary coalescences in the third LIGO–Virgo observing run”. In: *Classical and Quantum Gravity* 38.9 (2021), p. 095004.

[68] Francesco Di Renzo. “Gravitational-wave event validation by Advanced LIGO and Advanced Virgo detectors”. In: (2022).

[69] R Abbott et al. “Constraints on the cosmic expansion history from GWTC-3”. In: *The Astrophysical Journal* 949.2 (2023).

[70] Nelson Christensen and Renate Meyer. “Parameter estimation with gravitational waves”. In: *Reviews of Modern Physics* 94.2 (2022), p. 025001.

[71] Stephen R. Green, Christine Simpson, and Jonathan Gair. “Gravitational-wave parameter estimation with autoregressive neural network flows”. In: *Phys. Rev. D* 102 (10 2020), p. 104057. DOI: 10.1103/PhysRevD.102.104057. URL: https://link.aps.org/doi/10.1103/PhysRevD.102.104057.

[72] Michael J Williams, John Veitch, and Chris Messenger. “Nested sampling with normalizing flows for gravitational-wave inference”. In: *Physical Review D* 103.10 (2021), p. 103006.

[73] Hunter Gabbard et al. “Bayesian parameter estimation using conditional variational autoencoders for gravitational-wave astronomy”. In: *Nature Physics* 18.1 (2022), pp. 112–117.

[74] Isobel Romero-Shaw et al. “GW190521: orbital eccentricity and signatures of dynamical formation in a binary black hole merger signal”. In: *The Astrophysical Journal Letters* 903.1 (2020), p. L5.

[75] Rossella Gamba et al. “GW190521 as a dynamical capture of two nonspinning black holes”. In: *Nature Astronomy* 7.1 (2023), pp. 11–17.

[76] Marco Dall’Amico et al. “Eccentric black hole mergers via three-body interactions in young, globular and nuclear star clusters”. In: *arXiv preprint arXiv:2303.07421* (2023).

[77] Alessandro A Trani et al. “Compact object mergers in hierarchical triples from low-mass young star clusters”. In: *Monthly Notices of the Royal Astronomical Society* 511.1 (2022), pp. 1362–1372.

[78] Johan Samsing. “Eccentric black hole mergers forming in globular clusters”. In: *Physical Review D* 97.10 (2018), p. 103014.

[79] Duncan A Brown and Peter J Zimmerman. “Effect of eccentricity on searches for gravitational waves from coalescing compact binaries in ground-based detectors”. In: *Physical Review D* 81.2 (2010), p. 024007.

[80] Antoni Ramos-Buades et al. “Impact of eccentricity on the gravitational-wave searches for binary black holes: High mass case”. In: *Physical Review D* 102.4 (2020), p. 043005.

[81] AG Abac et al. “Search for Eccentric Black Hole Coalescences during the Third Observing Run of LIGO and Virgo”. In: *arXiv preprint arXiv:2308.03822* (2023).

[82] Demetrios Christodoulou. “Nonlinear nature of gravitation and gravitational-wave experiments”. In: *Physical review letters* 67.12 (1991), p. 1486.

[83] Marc Favata. “The gravitational-wave memory effect”. In: *Classical and Quantum Gravity* 27.8 (2010), p. 084036.

[84] Michael Ebersold and Shubhanshu Tiwari. “Search for nonlinear memory from subsolar mass compact binary mergers”. In: *Physical Review D* 101.10 (2020), p. 104041.

[85] Shubhanshu Tiwari, Michael Ebersold, and Eleanor Z Hamilton. “Leveraging gravitational-wave memory to distinguish neutron star-black hole binaries from black hole binaries”. In: *Physical Review D* 104.12 (2021), p. 123024.

[86] Liang Dai and Tejaswi Venumadhav. “On the waveforms of gravitationally lensed gravitational waves”. In: *arXiv preprint arXiv:1702.04724* (2017).

[87] Jose María Ezquiaga et al. “Phase effects from strong gravitational lensing of gravitational waves”. In: *Physical Review D* 103.6 (2021), p. 064047.

[88] Emanuele Berti et al. “Testing general relativity with present and future astrophysical observations”. In: *Classical and Quantum Gravity* 32.24 (2015), p. 243001.

[89] Vitor Cardoso and Paolo Pani. “Testing the nature of dark compact objects: a status report”. In: *Living Reviews in Relativity* 22 (2019), pp. 1–104.

[90] Katerina Chatziioannou et al. “Morphology-independent test of the mixed polarization content of transient gravitational wave signals”. In: *Physical Review D* 104.4 (2021), p. 044005.

[91] NV Krishnendu, Chandra Kant Mishra, and KG Arun. "Spin-induced deformations and tests of binary black hole nature using third-generation detectors". In: *Physical Review D* 99.6 (2019), p. 064008.

[92] Tatsuya Narikawa, Nami Uchikata, and Takahiro Tanaka. "Gravitational-wave constraints on the GWTC-2 events by measuring the tidal deformability and the spin-induced quadrupole moment". In: *Physical Review D* 104.8 (2021), p. 084056.

[93] Nathan K Johnson-McDaniel et al. "Constraining black hole mimickers with gravitational wave observations". In: *Physical Review D* 102.12 (2020), p. 123010.

[94] Vitor Cardoso and Paolo Pani. "Tests for the existence of black holes through gravitational wave echoes". In: *Nature Astronomy* 1.9 (2017), pp. 586–591.

[95] Andrea Miani et al. "Constraints on the amplitude of gravitational wave echoes from black hole ringdown using minimal assumptions". In: *Phys. Rev. D* 108 (6 2023), p. 064018. DOI: 10.1103/PhysRevD.108.064018. URL: https://link.aps.org/doi/10.1103/PhysRevD.108.064018.

[96] Salvatore Capozziello et al. "Gravitational waves from hyperbolic encounters". In: *Modern Physics Letters A* 23.02 (2008), pp. 99–107.

[97] Subhajit Dandapat et al. "Gravitational Waves from Black-Hole Encounters: Prospects for Ground-and Galaxy-Based Observatories". In: *arXiv preprint arXiv:2305.19318* (2023).

[98] Sajal Mukherjee, Sanjit Mitra, and Sourav Chatterjee. "Gravitational wave observatories may be able to detect hyperbolic encounters of black holes". In: *Monthly Notices of the Royal Astronomical Society* 508.4 (2021), pp. 5064–5073.

[99] Juan Garcia-Bellido and Savvas Nesseris. "Gravitational wave bursts from Primordial Black Hole hyperbolic encounters". In: *Physics of the dark universe* 18 (2017), pp. 123–126.

[100] Hans-Thomas Janka. "Explosion mechanisms of core-collapse supernovae". In: *Annual Review of Nuclear and Particle Science* 62 (2012), pp. 407–451.

[101] Kazuto Hirata et al. "Observation of a neutrino burst from the supernova SN1987A". In: *Physical Review Letters* 58.14 (1987), p. 1490.

[102] BP Abbott et al. "Optically targeted search for gravitational waves emitted by core-collapse supernovae during the first and second observing runs of advanced LIGO and advanced Virgo". In: *Physical Review D* 101.8 (2020), p. 084002.

[103] R. Abbott et al. "All-sky search for short gravitational-wave bursts in the third Advanced LIGO and Advanced Virgo run". In: *Phys. Rev. D* 104.12 (2021), p. 122004. DOI: 10.1103/PhysRevD.104.122004. arXiv: 2107.03701 [gr-qc].

[104] Jade Powell and Bernhard Müller. "Gravitational wave emission from 3D explosion models of core-collapse supernovae with low and normal explosion energies". In: *Monthly Notices of the Royal Astronomical Society* 487.1 (2019), pp. 1178–1190.

[105] Brynmor Haskell and Andrew Melatos. "Models of pulsar glitches". In: *International Journal of Modern Physics D* 24.03 (2015), p. 1530008.

[106] R Abbott et al. "Search for gravitational-wave transients associated with magnetar bursts in Advanced LIGO and Advanced Virgo data from the third observing run". In: *arXiv preprint arXiv:2210.10931* (2022).

[107] R Abbott et al. "Constraints on cosmic strings using data from the third Advanced LIGO–Virgo observing run". In: *Physical review letters* 126.24 (2021), p. 241102.

[108] Daichi Tsuna. *Comparing burst search sensitivities to Cosmic strings*. Tech. rep. DCC G2300822, 2023.

[109] Gianfranco Bertone and Dan Hooper. "History of dark matter". In: *Reviews of Modern Physics* 90.4 (2018), p. 045002.

[110] Gianfranco Bertone et al. "Gravitational wave probes of dark matter: challenges and opportunities". In: *SciPost Physics Core* 3.2 (2020), p. 007.

[111] Juan García-Bellido and Savvas Nesseris. "Gravitational wave energy emission and detection rates of Primordial Black Hole hyperbolic encounters". In: *Physics of the dark universe* 21 (2018), pp. 61–69.

[112] Vitor Cardoso and Andrea Maselli. "Constraints on the astrophysical environment of binaries with gravitational-wave observations". In: *Astronomy & Astrophysics* 644 (2020), A147.

[113] Sergey Klimenko et al. "A coherent method for detection of gravitational wave bursts". In: *Classical and Quantum Gravity* 25.11 (2008), p. 114029.

[114] J. Abadie et al. "All-sky search for gravitational-wave bursts in the first joint LIGO-GEO-Virgo run". In: *Phys. Rev. D* 81 (2010), p. 102001. DOI: 10.1103/PhysRevD.81.102001. arXiv: 1002.1036 [gr-qc].

[115] BP Abbott et al. "All-sky search for short gravitational-wave bursts in the second Advanced LIGO and Advanced Virgo run". In: *Physical Review D* 100.2 (2019), p. 024017.

[116] F Salemi et al. "Wider look at the gravitational-wave transients from GWTC-1 using an unmodeled reconstruction method". In: *Physical review D* 100.4 (2019), p. 042003.

[117] B. P. et all Abbott. "Observation of Gravitational Waves from a Binary Black Hole Merger". In: *Phys. Rev. Lett.* 116 (6 2016), p. 061102. DOI: 10.1103/PhysRevLett.116.061102. URL: https://link.aps.org/doi/10.1103/PhysRevLett.116.061102.

[118] Marek Szczepańczyk et al. "Observing an intermediate-mass black hole GW190521 with minimal assumptions". In: *Physical Review D* 103.8 (2021), p. 082002.

[119] Gabriele Vedovato et al. "Minimally-modeled search of higher multipole gravitational-wave radiation in compact binary coalescences". In: *Classical and Quantum Gravity* 39.4 (2022), p. 045001.

[120] AG Abac et al. "Search for Eccentric Black Hole Coalescences during the Third Observing Run of LIGO and Virgo". In: *arXiv preprint arXiv:2308.03822* (2023).

[121] MC Tringali et al. "Morphology-independent characterization method of postmerger gravitational wave emission from binary neutron star coalescences". In: *Classical and Quantum Gravity* 40.22 (2023), p. 225008.

[122] Sebastian Khan et al. "Phenomenological model for the gravitational-wave signal from precessing binary black holes with two-spin effects". In: *Physical Review D* 100.2 (2019), p. 024059.

[123] Yumeng Xu, Shubhanshu Tiwari, and Marco Drago. "PycWB: A user-friendly, Modular, and python-based framework for gravitational wave unmodelled search". In: *SoftwareX* 26 (2024), p. 101639.

[124] V Necula, S Klimenko, and G Mitselmakher. "Transient analysis with fast Wilson-Daubechies time-frequency transform". In: *Journal of Physics: Conference Series*. Vol. 363. IOP Publishing. 2012, p. 012032.

[125] Vaibhav Tiwari et al. “Regression of environmental noise in LIGO data”. In: *Classical and Quantum Gravity* 32.16 (2015), p. 165014.

[126] Eric Thrane et al. “Correlated noise in networks of gravitational-wave detectors: Subtraction and mitigation”. In: *Physical Review D* 90.2 (2014), p. 023013.

[127] Nicolas Arnaud et al. “Coincidence and coherent data analysis methods for gravitational wave bursts in a network of interferometric detectors”. In: *Physical Review D* 68.10 (2003), p. 102001.

[128] Sergei Klimenko et al. “Constraint likelihood analysis for a network of gravitational wave detectors”. In: *Physical Review D* 72.12 (2005), p. 122002.

[129] Sophie Bini et al. “An autoencoder neural network integrated into gravitational-wave burst searches to improve the rejection of noise transients”. In: *Classical and Quantum Gravity* (2023).

[130] Tianqi Chen et al. “Xgboost: extreme gradient boosting”. In: *R package version 0.4-2* 1.4 (2015), pp. 1–4.

[131] Tanmaya Mishra et al. “Optimization of model independent gravitational wave search for binary black hole mergers using machine learning”. In: *Physical Review D* 104.2 (2021), p. 023014.

[132] Tanmaya Mishra et al. “Search for binary black hole mergers in the third observing run of Advanced LIGO-Virgo using coherent WaveBurst enhanced with machine learning”. In: *Physical Review D* 105.8 (2022), p. 083018.

[133] Marek J. Szczepa ńczyk et al. “Search for gravitational-wave bursts in the third Advanced LIGO-Virgo run with coherent WaveBurst enhanced by machine learning”. In: *Phys. Rev. D* 107 (6 2023), p. 062002. DOI: 10.1103/PhysRevD.107.062002. URL: https://link.aps.org/doi/10.1103/PhysRevD.107.062002.

[134] Dixeena Lopez et al. “Utilizing Gaussian mixture models in all-sky searches for short-duration gravitational wave bursts”. In: *Physical Review D* 105.6 (2022), p. 063024.

[135] Sergey Klimenko. “Wavescan: multiresolution regression of gravitational-wave data”. In: *arXiv preprint arXiv:2201.01096* (2022).

[136] Neil J Cornish and Tyson B Littenberg. “Bayeswave: Bayesian inference for gravitational wave bursts and instrument glitches”. In: *Classical and Quantum Gravity* 32.13 (2015), p. 135012.

[137] Neil J Cornish et al. “BayesWave analysis pipeline in the era of gravitational wave observations”. In: *Physical Review D* 103.4 (2021), p. 044006.

[138] Katerina Chatziioannou et al. “Modeling compact binary signals and instrumental glitches in gravitational wave data”. In: *Physical Review D* 103.4 (2021), p. 044013.

[139] Ryan Lynch et al. “Information-theoretic approach to the gravitational-wave burst detection problem”. In: *Physical Review D* 95.10 (2017), p. 104046.

[140] Florent Robinet et al. “Omicron: a tool to characterize transient noise in gravitational-wave detectors”. In: *SoftwareX* 12 (2020), p. 100620.

[141] Patrick J Sutton et al. “X-Pipeline: an analysis package for autonomous gravitational-wave burst searches”. In: *New Journal of Physics* 12.5 (2010), p. 053034.

[142] R Abbott et al. “Search for gravitational waves associated with gamma-ray bursts detected by Fermi and Swift during the LIGO–Virgo run O3b”. In: *The Astrophysical Journal* 928.2 (2022), p. 186.

[143] R Abbott et al. "Search for Gravitational Waves Associated with Fast Radio Bursts Detected by CHIME/FRB During the LIGO–Virgo Observing Run O3a". In: *arXiv preprint arXiv:2203.12038* (2022).

[144] Vasileios Skliris, Michael RK Norman, and Patrick J Sutton. "Real-Time Detection of Unmodelled Gravitational-Wave Transients Using Convolutional Neural Networks". In: *arXiv preprint arXiv:2009.14611* (2020).

[145] S Klimenko et al. "Localization of gravitational wave sources with networks of advanced detectors". In: *Physical Review D* 83.10 (2011), p. 102001.

[146] S Klimenko et al. "Method for detection and reconstruction of gravitational wave transients with networks of advanced detectors". In: *Physical Review D* 93.4 (2016), p. 042004.

[147] Irene Di Palma and Marco Drago. "Estimation of the gravitational wave polarizations from a nontemplate search". In: *Physical Review D* 97.2 (2018), p. 023011.

[148] Yuki Hagihara et al. "Probing gravitational wave polarizations with Advanced LIGO, Advanced Virgo, and KAGRA". In: *Physical Review D* 98.6 (2018), p. 064035.

[149] Katerina Chatziioannou, Nicolas Yunes, and Neil Cornish. "Model-independent test of general relativity: An extended post-Einsteinian framework with complete polarization content". In: *arXiv preprint arXiv:1204.2585* (2012).

[150] Gareth S Davies et al. "Extending the PyCBC search for gravitational waves from compact binary mergers to a global network". In: *Physical Review D* 102.2 (2020), p. 022004.

[151] Yi Shuen C Lee, Margaret Millhouse, and Andrew Melatos. "Enhancing the gravitational-wave burst detection confidence in expanded detector networks with the BayesWave pipeline". In: *Physical Review D* 103.6 (2021), p. 062002.

[152] cWB. *Documentation*. 2024. URL: https://gwburst.gitlab.io/documentation/latest/html/faq.html#the-cwb-2g-regulators (visited on 2024).

[153] Reed Essick et al. "Localization of short duration gravitational-wave transients with the early Advanced LIGO and Virgo detectors". In: *The Astrophysical Journal* 800.2 (2015), p. 81.

[154] Michael Zevin et al. "Gravity Spy: integrating advanced LIGO detector characterization, machine learning, and citizen science". In: *Classical and quantum gravity* 34.6 (2017), p. 064003.

[155] Massimiliano Razzano et al. "GWitchHunters: Machine learning and citizen science to improve the performance of gravitational wave detector". In: *Nuclear Instruments and Methods in Physics Research Section A: Accelerators, Spectrometers, Detectors and Associated Equipment* 1048 (2023), p. 167959. ISSN: 0168-9002. DOI: https://doi.org/10.1016/j.nima.2022.167959. URL: https://www.sciencedirect.com/science/article/pii/S0168900222012517.

[156] Miriam Cabero et al. "Blip glitches in Advanced LIGO data". In: *Classical and Quantum Gravity* 36.15 (2019), p. 155010.

[157] Benjamin P Abbott et al. "Characterization of transient noise in Advanced LIGO relevant to gravitational wave signal GW150914". In: *Classical and Quantum Gravity* 33.13 (2016), p. 134001.

[158] Benjamin P Abbott et al. "Effects of data quality vetoes on a search for compact binary coalescences in Advanced LIGO's first observing run". In: *Classical and Quantum Gravity* 35.6 (2018), p. 065010.

[159] Jane Glanzer et al. "Data quality up to the third observing run of Advanced LIGO: Gravity Spy glitch classifications". In: *Classical and Quantum Gravity* (2022).

[160] Alexander H Nitz. "Distinguishing short duration noise transients in LIGO data to improve the PyCBC search for gravitational waves from high mass binary black hole mergers". In: *Classical and Quantum Gravity* 35.3 (2018), p. 035016.

[161] Rich Ormiston et al. "Noise reduction in gravitational-wave data via deep learning". In: *Physical Review Research* 2.3 (2020), p. 033066.

[162] Hongyu Shen et al. "Denoising gravitational waves with enhanced deep recurrent denoising auto-encoders". In: *ICASSP 2019-2019 IEEE International Conference on Acoustics, Speech and Signal Processing (ICASSP)*. IEEE. 2019, pp. 3237–3241.

[163] Roberto Corizzo et al. "Scalable auto-encoders for gravitational waves detection from time series data". In: *Expert Systems with Applications* 151 (2020), p. 113378.

[164] Filip Morawski et al. "Anomaly detection in gravitational waves data using convolutional autoencoders". In: *Machine Learning: Science and Technology* 2.4 (2021), p. 045014.

[165] Eric A Moreno et al. "Source-agnostic gravitational-wave detection with recurrent autoencoders". In: *Machine Learning: Science and Technology* 3.2 (2022), p. 025001.

[166] Andrew Ng et al. "Sparse autoencoder". In: *CS294A Lecture notes* 72.2011 (2011), pp. 1–19.

[167] Rasmus Bro and Age K Smilde. "Principal component analysis". In: *Analytical methods* 6.9 (2014), pp. 2812–2831.

[168] François Chollet. *Keras, version 2.11.0,* `https://github.com/fchollet/keras`. 2015.

[169] Abien Fred Agarap. "Deep learning using rectified linear units (relu)". In: *arXiv preprint arXiv:1803.08375* (2018).

[170] Sepp Hochreiter and Jürgen Schmidhuber. "Long short-term memory". In: *Neural computation* 9.8 (1997), pp. 1735–1780.

[171] Diederik P Kingma and Jimmy Ba. "Adam: A method for stochastic optimization". In: *arXiv preprint arXiv:1412.6980* (2014).

[172] Serguei Ossokine et al. "Multipolar effective-one-body waveforms for precessing binary black holes: Construction and validation". In: *Physical Review D* 102.4 (2020), p. 044055.

[173] J. Abadie et al. "All-sky search for gravitational-wave bursts in the second joint LIGO-Virgo run". In: *Phys. Rev. D* 85 (2012), p. 122007. DOI: `10.1103/PhysRevD.85.122007`. arXiv: `1202.2788 [gr-qc]`.

[174] Sophie Bini et al. "Search for hyperbolic encounters of compact objects in the third LIGO-Virgo-KAGRA observing run". In: *Physical Review D* 109.4 (2024), p. 042009.

[175] William Marshall Smart and Robin Michael Green. *Textbook on spherical astronomy*. Cambridge University Press, 1977.

[176] T. Damour and N. Deruelle. "General relativistic celestial mechanics of binary systems. I. The post-Newtonian motion." In: *Annales de L'Institut Henri Poincare Section (A) Physique Theorique* 43.1 (1985), pp. 107–132.

[177] Gihyuk Cho et al. "Gravitational waves from compact binaries in post-Newtonian accurate hyperbolic orbits". In: *Physical Review D* 98.2 (2018), p. 024039.

[178] Mohammed Khalil et al. "Energetics and scattering of gravitational two-body systems at fourth post-Minkowskian order". In: *Physical Review D* 106.2 (2022), p. 024042.

[179] Thibault Damour and Piero Rettegno. "Strong-field scattering of two black holes: Numerical relativity meets post-Minkowskian gravity". In: *Physical Review D* 107.6 (2023), p. 064051.

[180] Santiago Jaraba and Juan Garcia-Bellido. "Black hole induced spins from hyperbolic encounters in dense clusters". In: *Physics of the Dark Universe* 34 (2021), p. 100882.

[181] Patrick E Nelson et al. "Induced spins from scattering experiments of initially nonspinning black holes". In: *Physical Review D* 100.12 (2019), p. 124045.

[182] Alessandro Nagar et al. "Effective-one-body waveforms from dynamical captures in black hole binaries". In: *Physical Review D* 103.6 (2021), p. 064013.

[183] Simone Albanesi et al. "New avenue for accurate analytical waveforms and fluxes for eccentric compact binaries". In: *Physical Review D* 105.12 (2022), p. L121503.

[184] Tomas Andrade et al. "Towards numerical-relativity informed effective-one-body waveforms for dynamical capture black hole binaries". In: *arXiv preprint arXiv:2307.08697* (2023).

[185] AG Abac et al. "Search for Eccentric Black Hole Coalescences during the Third Observing Run of LIGO and Virgo". In: *arXiv preprint arXiv:2308.03822* (2023).

[186] Vaibhav Tiwari. "Estimation of the sensitive volume for gravitational-wave source populations using weighted Monte Carlo integration". In: *Classical and Quantum Gravity* 35.14 (2018), p. 145009.

[187] Patrick J Sutton. "Upper limits from counting experiments with multiple pipelines". In: *Classical and Quantum Gravity* 26.24 (2009), p. 245007.

[188] David Tsang. "Shattering flares during close encounters of neutron stars". In: *The Astrophysical Journal* 777.2 (2013), p. 103.

[189] V. Gayathri et al. "Enhancing the sensitivity of transient gravitational wave searches with Gaussian mixture models". In: *Phys. Rev. D* 102 (10 2020), p. 104023. DOI: 10.1103/PhysRevD.102.104023. URL: https://link.aps.org/doi/10.1103/PhysRevD.102.104023.

[190] Alejandro Bohé et al. "Improved effective-one-body model of spinning, nonprecessing binary black holes for the era of gravitational-wave astrophysics with advanced detectors". In: *Physical Review D* 95.4 (2017), p. 044028.

[191] Philip Relton and Vivien Raymond. "Parameter estimation bias from overlapping binary black hole events in second generation interferometers". In: *Physical Review D* 104.8 (2021), p. 084039.

List of Figures

List of Tables